



Norwegian University of
Science and Technology

Anti-Icing and De-Icing of Pipe Structures on Marine Vessels using Waste Heat Recovery

Numerical Simulations and Experimental
Testing of Ulmatec Pyro's Double-Pipe
Technology

Lene *Æ*esøy

Mechanical Engineering
Submission date: July 2017
Supervisor: Zhiliang Zhang, KT

Norwegian University of Science and Technology
Department of Structural Engineering



MASTER THESIS 2017

SUBJECT AREA: Arctic technology	DATE: 31.07.2017	NO. OF PAGES: 81 + Appendices
------------------------------------	---------------------	----------------------------------

TITLE:

Anti-Icing and De-Icing of Pipe Structures on Marine Vessels using Waste Heat Recovery

Anti-Ising og Avising av Rørkonstruksjoner på Skip
ved bruk av Vannbåren Spillvarme

BY:

Lene Æsøy



ABSTRACT:

Marine activities in Arctic waters are endangered by ice accretion. To meet the IMO Polar Code for ships operating in Arctic areas, a waterborne heating systems using waste heat through a "double-pipe system" has been developed by Ulmatec Pyro. The main objective of this thesis project has been to investigate the behaviour of anti-icing and de-icing for pipe structures on ships to provide knowledge for design and operations.

Numerical models are developed and experimental tests have been performed. A one-dimensional heat transfer simulation model was programmed in MATLAB. In addition, a three-dimensional CFD simulation model was developed to include the transient behaviour. These simulation models were based on fundamental thermo- and fluid- dynamics, combined with empirical data from previous icing research. Comparing the steady state simulation results, the CFD model and the simple 1D model show good correlations between the models and the experimental results.

The experimental setup was designed and built for validating theoretical models, and further as a design verification lab for Ulmatec Pyro. A series of experiments are conducted, providing valuable insight in the icing- and anti-icing processes for the "double-pipe system". The experiments gave a better understanding of the complex ice melting process, and provided input of further modifications of the simulation models.

The experiments also provided valuable experience and information needed to upgrade the test setup for further testing with more extreme Polar conditions.

SUPERVISOR:

Prof. Zhiliang Zhang

CARRIED OUT AT:

Department of Structural Engineering at NTNU-Trondheim and Ulmatec Pyro 6280 Søvik

Summary

Shipping, fishing and exploration activities in Arctic waters are endangered by ice accretion on critical structures causing various safety risks. Ulmatec Pyro have developed an anti-icing/de-icing system using waste heat circulation in a “double pipe system”, for hand railings, helicopter decks and stairway applications. The research objectives of this master thesis was to support Ulmatec Pyro in the design process, using theoretical models for design optimization, and to develop experimental facilities to verify their designs to meet the IMO Polar Code for ships operating in Arctic areas.

The first part of the project investigated relevant literature and research on icing mechanisms and de-icing technologies. Atmospheric icing is a known problem for mobile units such as airplanes. However, marine icing is more complex since it involves saline water. Further, the marine icing process is more unpredictable with a periodic behavior caused by the weather conditions.

Two different numerical models are developed, based on previous icing studies and combined with basic thermo- and fluid- dynamics. First, a simple 1-dimensional steady state anti-icing model was developed using finite difference method (FDM) and lumped capacitance method (LCM). This model programmed in MATLAB code, is made for a given symmetrical double pipe geometry, and shows good correlations with experimental tests. The second model is made in COMSOL Multiphysics, where 2-dimensional axisymmetric geometry is used. This model is able to handle transient as well as steady state conditions. The purpose of this model was to simulate de-icing processes. Comparing the steady state results, the CFD model and the simple 1D model shows good correlations. The transient de-icing simulations results give good results within the assumptions that the water is entrapped in the ice. However, the de-icing experiments show that this model must be modified to give more realistic ice-melting behavior. These modifications include water draining giving insulation air layers between ice and pipe surface, and further include saline ice models.

An experimental setup was designed and built for validating theoretical models, and further as a design verification lab for Ulmatec Pyro. The test lab was built inside a commercial freezing container, which turned out to have insufficient freezing capacity for the extreme Polar test conditions. Despite of these limitations, a series of experiments were conducted, providing valuable insight in the icing- and anti-icing processes. The experiments also showed that double pipes gave a more uniform surface temperature than a single pipe, and that it is favorable with a higher flow velocity in the annulus between the inner and outer pipe.

The experiments confirm that the double pipe technology is giving a more uniform surface temperature along the pipe compared to a single pipe. Hence, a more efficient use of waterborne heat. The experiments also provided good validation of the theoretical simulation models within the available test conditions. De-icing tests also showed the complexity of the ice melting process. Hence, it gave a better understanding of the de-icing process and that more complex simulation models are needed. The experiments also provided valuable experience and information needed to upgrade the test rig for further testing with more extreme Polar conditions.

Sammendrag

Skip som opererer i arktiske farvann er utsatt for ising på kritiske strukturer som forårsaker ulike sikkerhetsrisikoer. Ulmatec Pyro har utviklet et system for anti-ising og av-ising som bruker spill-varme i et ”dobbeltrørsystem”, tiltenkt rekkverk, rømningsveier og helikopterdekk. Målet med denne masteroppgaven var å støtte Ulmatec Pyro i designprosessen, ved hjelp av teoretiske modeller for designoptimalisering, og utvikling av et eksperimentelt anlegg for å teste og verifisere deres design for å møte sikkerhetskravene til IMO (Polar Code) for skip som opererer i Arktiske farvann.

Den første delen av prosjektet undersøkte relevant litteratur og forskning om isingsmekanismer og avisningsteknologier. Atmosfærisk ising er et kjent problem for mobile enheter som fly. Men marin-ising er mer kompleks fordi det innebærer saltvann. Videre er marin-ising mer uforutsigbar med en periodisk oppførsel forårsaket av værforholdene.

To forskjellige numeriske modeller er utviklet, basert på tidligere studier av ising kombinert med grunnleggende termo- og fluiddynamikk. Først ble en enkel, 1-dimensjonal, stasjonær anti-ising modell utviklet ved bruk av Finite Difference Method (FDM) og Lumped Capacitance Method (LCM). Denne modellen er programmert i MATLAB og laget for en gitt symmetrisk dobbeltrør-geometri. Modellen viser gode korrelasjoner med eksperimentelle tester. Den andre modellen er laget i COMSOL Multiphysics, hvor en 2-dimensjonal aksisymmetrisk geometri brukes. Denne modellen er i stand til å håndtere tidsavhengige og stasjonære forhold. Formålet med denne modellen var å simulere avisingsprosesser. Sammenligning av de teoretiske modellene med de stasjonære eksperimentelle resultatene viser gode korrelasjoner med både CFD-modellen og den enkle 1D-modellen. Simuleringsresultatene fra den tidsavhengige avisings-modellen gir gode resultater innenfor forutsetningene om at vannet er fanget i isen (ingen drenering). Avisningsforsøkene viser imidlertid at denne modellen må modifiseres for å gi mer realistisk oppførsel av is-smeltingen. Disse modifikasjonene inkluderer vandredrenering som gir isolerende luftlommer mellom is- og røroverflate, samt inkludering av modeller for sjøvann.

Et eksperimentelt oppsett ble designet og bygget for å verifisere de teoretiske modellene, og videre som et design verifikasjonslaboratorium for Ulmatec Pyro. Testlabben ble bygd inne i en kommersiell frysecontainer, som viste seg å ha utilstrekkelig frysekapasitet for de planlagte ekstreme (Polare) testbetingelsene. Til tross for disse begrensningene ble det gjennomført en rekke eksperimenter, noe som ga verdifull innsikt i mekanismene for ising og anti-ising. Eksperimentene viste også at dobbeltrør ga jevnere overflatetemperatur enn et enkeltør, samt at det er gunstig med høyere strømningshastighet i ytterrøret.

Forsøkene bekrefter at dobbeltrørsteknologien gir en mer jevn overflatetemperatur langs røret enn ved bruk av et singelrør. Derfor er dette en mer effektiv bruk av vannbåren varme. Forsøkene ga også god validering av de teoretiske simuleringsmodellene innenfor de tilgjengelige testbetingelsene. Avisningstester viste også kompleksiteten til issmeltingsprosessen. Disse forsøkene ga en bedre forståelse av avisingsprosessene og forbedret simuleringsmodell er nødvendig. Forsøkene ga også verdifull erfaring og informasjon som var nødvendig for å oppgradere testriggeren for videre testing med mer ekstreme (Polare) forhold.

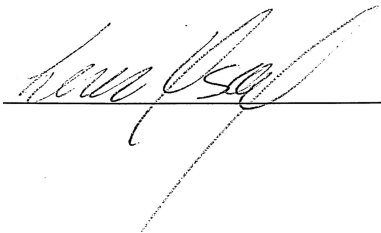
Preface

This master thesis is submitted to the Norwegian University of Science and Technology (NTNU). The master project has been performed at the Department of Structural Engineering, with Professor Zhiliang Zhang as main supervisor.

The experimental part has been performed at Ulmatec Pyro, with Jan Petter Urke, Arne Skotte and Roger Amdam as co-supervisors. Ulmatec Pyro financed the experimental parts of this project, as part of their product development program.

Ytre Hoem, 27. July 2017

Lene Æsøy

A handwritten signature in black ink, appearing to read 'Lene Æsøy', is written over a horizontal line. The signature is fluid and cursive, with a long, sweeping tail that extends downwards and to the right.

Acknowledgements

First I will thank my supervisor Prof. Zhiliang Zhang (NTNU), who encouraged me through the project and guided me through the development of the numerical simulation models.

I will also thank Ulmatec Pyro for the opportunity to work on this master thesis topic on the development of their new patented de-icing technology. I will specially thank Managing Director Jan Petter Urke, former Technical Manager Arne Skotte and the new Technical Manager Roger Amdam for the opportunity and liberty they gave me, allowing me to define the master thesis objectives and to take part in the design of the De-Icing Simulation Laboratory. Also many thanks to the great and positive people involved in the project at Ulmatec Pyro; Maria Dolores for detail design and follow-up on the construction of the laboratory, Palmar for urgently ordering parts when needed, Jan Arild for his patience with this "odd" project, Terje and Torgeir for always solving the automation problems and Edvard for finalizing the test rig and technical assisting during experiments. I have learned a lot from this practical experience, and I hope that they have benefited from my contributions in this project.

I will also thank NTNU Ålesund for letting me borrow technical measuring equipment for the experiments (IR-camera).

Finally, I want to express my gratitude to my parents for providing me with support and encouragement throughout my study at NTNU. I would especially thank my dad, Vilmar for helping me with guidance related to the experiments. Also, I want to thank my mom, Wenche for clean clothes and making dinner in the hectically submission period. This accomplishment would not have been possible without their help.

Thank you all!

Table of Contents

Summary	i
Sammendrag	ii
Preface	iii
Acknowledgements	iv
Table of Contents	v
List of Tables	vii
List of Figures	ix
Nomenclature	xiii
1 Introduction	1
2 Theory	7
2.1 Icing as a phenomenon	8
2.1.1 Marine icing models	8
2.1.2 Saline water icing	10
2.1.3 Periodic icing processes	10
2.2 Heating requirements for icing prevention	11
2.2.1 Anti-icing requirements	13
2.2.2 De-icing requirements	13
2.3 Heat transfer	14
2.3.1 Heat transfer mechanisms	15
2.3.2 Modelling approaches	22

3	Numerical simulation models	23
3.1	Umatec Pyro's double pipe design	23
3.2	1D Axisymmetric heat transfer model	25
3.3	2D Axisymmetric heat transfer model (CFD)	29
	3.3.1 Steady state model (Anti-icing)	29
	3.3.2 Transient model (De-icing)	31
3.4	Simulation results	32
	3.4.1 Anti-icing simulations	32
	3.4.2 De-icing simulations	37
4	Experiments	41
4.1	Laboratory design and experimental setup	41
	4.1.1 Icing simulation chamber	42
	4.1.2 Test section (pipe design)	43
	4.1.3 Instrumentation and data logging	46
	4.1.4 Flow sensor calibration	48
	4.1.5 Air flow measurements	48
	4.1.6 Infrared camera for pipe surface temperature measurements	50
	4.1.7 Test procedure/plan	51
4.2	Experimental results	54
	4.2.1 Case 1; Anti-icing	54
	4.2.2 Case 2; Icing	57
	4.2.3 Case 3; De-icing	58
5	Results and discussion	59
5.1	Anti-icing experiments vs. 1D simulations	59
	5.1.1 Experimental heat transfer coefficients	68
	5.1.2 Design simulations for Polar Code Conditions	70
5.2	Icing experiment	72
5.3	De-icing simulations vs. experiments	73
5.4	Experimental uncertainty and test rig modification	75
5.5	Suggestions for further work	76
	5.5.1 Theoretical model modifications	76
	5.5.2 Experiments	76
6	Conclusions	77
	References	79
	APPENDICES	82
A	Material Properties	83
	A.1 Saline Ice and Water	83
	A.2 Glycol-Water mixture	84
	A.3 Air	86
B	MATLAB Codes	87

List of Tables

2.1	DNV GL's document Rules of classifications on ships; <i>Class notation Winterized (Table A1)</i> [6]	12
2.2	DNV GL's document rules of classifications on ships; <i>Typical design environmental conditions (Table A2)</i> . [6]	12
2.3	Definitions and equations of dimensionless parameters used in heat transfer calculations.	18
2.4	Nusselt numbers for various geometries relevant for this thesis (ref. [29]).	19
4.1	Pipe dimensions for the laboratory experiments.	44
4.2	Overview of sensors and control valves.	46
4.3	Wind velocity calibration measurements.	49
4.4	Overview of the planned test for Case 1; Anti-icing.	52
4.5	Test result from the PLC. Case1; test 1-12. $\Delta T_L = T_{in} - T_{out}$ for the single pipe and $\Delta T_L = T_{turn} - T_{out}$ for the double pipes.	56
5.1	Results from the PLC and numerical simulations for the tests with wind velocity 0m/s	62
5.2	Results from the PLC and numerical simulations for the tests with wind velocity 2.6m/s	63
5.3	Heat transfer coefficient h_{air} calculation table.	69
A.1	Thermal Properties of Sea Ice $0^\circ C - 8^\circ C$ [26]	83
A.2	The thermal properties conductivity, density and dynamic viscosity are taken from[4], while the specific heat capacity are taken form [10].	85

List of Figures

1.1	<i>Icing on KV Nordkapp on the 27th of February 1987, Barents Sea. Left picture show the fore-ship and the wheel house, right picture show the starboard walkway and railings [24].</i>	1
1.2	Example picture to show that rough waves can make the sea splash all over the ship [2].	2
1.3	Principle picture to show which ising types are most current for ships. . .	3
1.4	Principle drawing of the de-icing technology design by Ulbatec Pyro . . .	5
2.1	Ice accretion on railings.	7
2.2	Marine icing due to sea spray (ref. Dehghani-sanij et.al) [5].	8
2.3	Principle drawing of the thermodynamic processes of icing, [18] [5]. . . .	9
2.4	<i>”Scheme of the ice growth caused by periodic sea spray. The black arrows represent the directions of the heat fluxes. The solid red line represents the temperature profile in the water and ice accretion. The dashed red line represents the temperature profile in the previous step.” [18]</i>	11
2.5	Principle of de-icing process of a horizontal cylinder using waterborne heat through a double pipe.	14
2.6	Principle Drawing of the de-icing process for a horizontal cylinder, here represented in 2D and 1D. $T(r)$ represent the temperature distribution throughout the cylinder as a function of the radius.	14
2.7	Schematic drawing of the thermal boundary layer.	16
2.8	Phase transition of melting ice.	20
2.9	Thermal resistant network through the body. The reference area A_{ref} is marked at the ininside of the pipe wall.	21
3.1	The principle of the Ulmatec Pyro double pipe technology. Temperature graph shows expected surface temperature for a double pipe compared to a single pipe.	24
3.2	Principle drawing of the double pipe with and without thickness of the pipe wall, where A refer to the cross section area.	24

3.3	Plot of the velocity factor of various relative areas.	25
3.4	Principle drawing of the 1D axisymmetric heat transfer model.	26
3.5	Principle drawing and equations for the first inner element of the 1D model, $j=1$	26
3.6	Principle drawing and equations for the first outer element of the 1D model, $j=1$	27
3.7	System equations for the lowest number of model elements ($m=3$).	27
3.8	Simulated temperature distribution of the double-pipe ($\text{Ø}50\text{-}\text{Ø}38$), ($L = 10\text{m}$, $U = 0\text{m/s}$, $T_{in} = 80^\circ\text{C}$, $T_\infty = -10^\circ\text{C}$ and $V_{flow} = 0.025\text{m}^3/\text{h}$).	28
3.9	Simulated temperature distribution for various number of elements m	28
3.10	Converging plot showing that $m=400$ is a sufficient number of elements. ΔT_{end} is converging towards 0 when $m=400$	29
3.11	Schematic overview of the boundary conditions and the mesh (pipe-turn) for the anti-icing.	30
3.12	Schematic overview of the boundary conditions and the mesh (pipe-turn) for the de-icing model.	32
3.13	Theoretical result comparing 1D and 2D steady state models for the $\text{Ø}50\text{-}\text{Ø}32$ double pipe used in the experiments in chapter 4.	33
3.14	Theoretical result comparing 1D and 2D steady state models for the $\text{Ø}50\text{-}\text{Ø}38$ double pipe used in the experiments in chapter 4.	34
3.15	Simulation result for the $\text{Ø}50$ single pipe (test 1 ref. table 4.4).	35
3.16	Parameter study comparing geometry and flow rates for double pipes with an outer pipe diameter $D = 50\text{mm}$	35
3.17	Parameter study comparing pipe length L and flow rates for double pipes with an outer pipe diameter $D = 50\text{mm}$	36
3.18	Temperature distribution of the de-icing simulation at time 3600s.	37
3.19	Temperature profiles for the ice layer model, fresh water ice with initial thickness 10mm. Temperatures higher than 0°C is equal to melted ice (water).	38
3.20	2D temperature plot at pipe length $L = 2.5\text{m}$	40
3.21	2D temperature plot at pipe length $L = 0.8\text{m}$	40
3.22	2D temperature plot at pipe length $L = 0\text{m}$	40
4.1	The freezer container general arrangement drawing with the essential equipment, pipes and connections between the units are not included in this drawing.	42
4.2	Principle drawing showing how the airflow is circulating in the test room.	43
4.3	Principle drawing of the pipe dimensions used in the experiments (ref. also table 4.1).	44
4.4	Principle drawing of the double pipe arrangement in the test section.	45
4.5	Test section consisting of three test pipes (1-3), temperature- (T) and flow sensors (F).	45
4.6	Schematic drawing of the de-icing test system.	46
4.7	Control system(PLC).	47
4.8	Temperature measurements for experimental and numerical comparison.	47
4.9	Flow sensor calibration. The calculated calibration factor is 0.0245.	48

4.10	Surface emissivity test for IR-camera. The object to the left is sprayed with matte black lacquer, and the one to the right has a shiny metal surface.	50
4.11	Icing - Manually application of the water spray.	53
4.12	Starting de-icing process.	53
4.13	Surface temperature measured with the IR-camera (inlet temperature $T_{in} \approx 35^{\circ}C$).	54
4.14	Time dependent temperature plot for the double-pipe $\text{Ø}50\text{-}\text{Ø}38$	55
4.15	Icing experiment from start to end. Total icing time is approx. 1 hour. . .	57
4.16	Time dependent temperature plot of the De-Icing Experiment.	58
4.17	Photographs of different parts of the pipes at different times during the De-Icing experiment.	58
5.1	Test 4: $V_{flow} \approx 0.01[m^3/h]$, $T_{in} \approx 40[^{\circ}C]$, $T_{\infty} \approx -10[^{\circ}C]$ and $U_{wind} = 0[m/s]$	60
5.2	Test 7: $V_{flow} \approx 0.02[m^3/h]$, $T_{in} \approx 20[^{\circ}C]$, $T_{\infty} \approx -10[^{\circ}C]$ and $U_{wind} = 0[m/s]$	60
5.3	Test 10: $V_{flow} \approx 0.02[m^3/h]$, $T_{in} \approx 40[^{\circ}C]$, $T_{\infty} \approx -10[^{\circ}C]$ and $U_{wind} = 0[m/s]$	60
5.4	Test 2: $V_{flow} \approx 0.01[m^3/h]$, $T_{in} \approx 20[^{\circ}C]$, $T_{\infty} \approx -10[^{\circ}C]$ and $U_{wind} = 2.6[m/s]$	61
5.5	Test 5: $V_{flow} \approx 0.01[m^3/h]$, $T_{in} \approx 40[^{\circ}C]$, $T_{\infty} \approx -10[^{\circ}C]$ and $U_{wind} = 2.6[m/s]$	61
5.6	Test 11: $V_{flow} \approx 0.02[m^3/h]$, $T_{in} \approx 40[^{\circ}C]$, $T_{\infty} \approx -10[^{\circ}C]$ and $U_{wind} = 2.6[m/s]$	61
5.7	Test 10: $T_{in} = 36.0^{\circ}C$, $V_{flow} = 0.016m^3/h$ and $U_{wind} = 0m/s$	63
5.8	Test 11: $T_{in} = 36.8^{\circ}C$, $V_{flow} = 0.016m^3/h$ and $U_{wind} = 2.6m/s$	64
5.9	Surface temperatures for wind velocity of 0 $[m/s]$, test number 1, 4, 7 and 10. C1 refers to the double pipe 50x32, and C2 refers to 50x38. The plot combines the experimental result (IR-camera) and numerical results from the 1D axisymmetrical model with the same conditions as the experimental data (ref. table 5.1).	65
5.10	Surface temperatures for wind velocity of 2.6 $[m/s]$, test number 2, 5, 8 and 11. C1 refers to the double pipe 50x32, and C2 refers to 50x38. The plot combines the experimental result (IR-camera) and numerical results from the 1D axisymmetrical model with the same conditions as the experimental data (ref. table 5.2).	66
5.11	Surface temperatures for wind velocity of 5.8 $[m/s]$, test number 3, 6, 9 and 12. C1 refers to the double pipe 50x32, and C2 refers to 50x38. The plot combines the experimental result (IR-camera) and numerical results from the 1D axisymmetrical model with the same conditions as the experimental data (ref. table 4.5).	67
5.12	Heat transfer coefficient h_{air} for theoretical simulations and experimental results.	68
5.13	Double pipe simulations for "Basic" condition; $T_{\infty} = -10^{\circ}C$, $U = 20m/s$ and $V_{flow} = 0.15m^3/h$	70

5.14	Double pipe simulations for "Cold" condition; $T_\infty = -30^\circ C$, $U = 20m/s$ and $V_{flow} = 0.4m^3/h$	71
5.15	Double pipe simulations for "Polar" condition; $T_\infty = -45^\circ C$, $U = 20m/s$ and $V_{flow} = 0.6m^3/h$	71
5.16	Icing process; The pictures taken with a GoPro camera in between every water spray.	72
5.17	Ice dimensions after the icing experiment. The ice thickness is approximately 10mm at the top, 7mm on the sides and 4mm at the bottom.	72
5.18	Schematic drawing of the de-icing process.	73
5.19	Infrared picture taken at the end of the De-Icing experiment.	74
5.20	Picture showing the insulating layer of air between the pipe surface and the ice.	74
A.1	Thermal Conductivity (k) of saline water and ice. The lines show functions of temperature from regression, while the dots represents measured values.	84

Nomenclature

Abbreviations	Definition
BC	Boundary condition
CFD	Computational Fluid Dynamics
COMSOL	COMputer SOLution
DNV GL	Det Norske Veritas (Norway) and Germanischer Lloyd (Germany)
FDM	Finite Difference Method
FEM	Finite Element Method
ICEMOD	Ising model by Ivar Horjen
IMO	International Maritime Organization (UN)
IR	Infrared
LCM	Lumped Capacitance Method
MATLAB	MATrix LABoratory
NTH	Norwegian Institute of Technology
NTNU	Norges Teknisk-Naturvitenskapelige Universitet
PC	Polar Class
PLC	Programmable Logic Controller
RIGICE04	Steady state Canadian icing model

Symbol	Definition	Unit
A_1	Cross section area inner pipe	$[m^2]$
A_2	Cross section area annulus	$[m^2]$
A_{ref}	Reference surface area	$[m^2]$
A_s	Surface area	$[m^2]$
b	Ice thickness	$[m]$
B_i	Biot number	$[-]$
C_L	Thermal capacitance	$[W/K]$
c_p	specific heat capacity	$[J/kgK]$
D	Diameter	$[m]$
d_1	Inner diameter annulus	$[m]$
d_2	Outer diameter annulus	$[m]$
D_h	Hydraulic diameter	$[m]$
e	saturated water pressure function of temperature	$[Pa]$
E	Evaporation coefficient	$[K/Pa]$
E_m	The energy of de-icing per unit area	$[J/m^2]$
f	Darcys friction factor	$[-]$

Symbol	Definition	Unit
F_d	Spray flux	$[m^2/s]$
g	Gravitational acceleration	$[-]$
Gr	Grashof number	$[-]$
h	Heat transfer coefficient	$[W/m^2K]$
h_{tot}	Total heat transfer coefficient	$[W/m^2K]$
h_{w1}	Convective heat transfer coefficient inner pipe flow	$[W/m^2K]$
h_{w2}	Convective heat transfer coefficient outer pipe flow	$[W/m^2K]$
h_{air}	Convective heat transfer coefficient air flow	$[W/m^2K]$
h_{mi}	Heat transfer coefficient of the melted ice	$[W/m^2K]$
H_f	Specific heat of fusion	$[J/kg]$
k	Conduction	$[W/mK]$
k_w	Thermal conductivity water	$[W/mK]$
k_{al}	Thermal conductivity aluminum	$[W/mK]$
k_{ice}	Thermal conductivity ice	$[W/mK]$
L_c	Characteristic length	$[m]$
L_f	Latent heat of fusion	$[J/kg]$
m	Radial integer	$[-]$
n	Longitudinal integer in FDM	$[-]$
n	Exponent related to combined convection	$[-]$
Nu	Nusslets number	$[-]$
Nu_N	Nusslets number for natural convection	$[-]$
Nu_F	Nusslets number for forced convection	$[-]$
$Nu_{combined}$	Nusslet number for combined convection	$[-]$
p	Time integer	$[-]$
Pr	Prandtl number	$[-]$
\dot{q}	Heat flux	$[W/m^2]$
\dot{q}_s	Surface heat flux	$[W/m^2]$
Q	Heat transfer	$[J]$
\dot{Q}	Heat transfer rate	$[W]$
\dot{Q}_a	Conductive heat transfer rate	$[W]$
\dot{Q}_c	Convective heat transfer rate	$[W]$
\dot{Q}_e	Heat transfer rate due to evaporation	$[W]$
\dot{Q}_w	Heat transfer rate due to impingement	$[W]$
\dot{Q}_r	Heat transfer rate due to radiation	$[W]$
\dot{Q}_v	Aerodynamic heat transfer rate	$[W]$
\dot{Q}_v	Heat transfer rate due to kinetic energy	$[W]$
\dot{Q}_f	Latent heat transfer rate due to freezing	$[W]$
Q_{tot}	Constant power of heat supplied	$[W]$
\dot{Q}_{cd}	Heat transfer rate due to conduction	$[W]$
\dot{Q}_{cv}	Heat transfer rate due to convection	$[W]$
r	Radius	$[m]$
R	Thermal resistance	$[K/W]$

Symbol	Definition	Unit
r_{ref}	Reference radius	[m]
r_H	Relative humidity	[-]
Ra_L	Rayleigh number	[-]
Ra_D	Rayleigh number for where $L_c = D$	[-]
Re	Reynolds number	[-]
S_w	Salinity of water	[%]
t	Time	[s]
t_m	Necessary de-icing time	[s]
t_d	Design temperature correlated to DNG GL standards	[K]
T_{avg}	Average bult temperature of the boundary layer	[K]
T_{bl}	Temperature of the boundary layer	[K]
T_d	Spray temperature	[K]
T_f	Freezing temperature	[K]
T_{in}	Inlet temperature	[K]
T_l	Liquid temperature	[K]
T_{out}	Outlet temperature	[K]
T_s	Surface temperature	[K]
$T_{s_{avg}}$	Average surface temperature	[K]
T_{sol}	Solid temperature	[K]
T_w	Water film temperature	[K]
$T_{w_{in}}$	Water flow inlet temperature	[K]
$T_{w_{out}}$	Water flow outlet temperature	[K]
T_∞	Temperature outside the boundary layer	[K]
U_{air}	Wind (air) velocity	[m/s]
U_{in}	Inlet velocity	[m/s]
U_{out}	Outlet velocity	[m/s]
V_{flow}	Water flow rate	[m ³ /h]
β	Coefficient for volume expansion	[1/K]
δ_t	Thermal boundary layer thickness	[m]
Δr	Radial step	[m]
Δt	Time step	[s]
ΔT	Temperature difference	[K]
Δz	Length step	[m]
η	Water film thickness	[m]
μ	Dynamic viscosity	[kg/ms]
ν	Kinematic viscosity	[m ² /s]
ρ	Density	[kg/m ³]
ρ_i	Ice dencity	[kg/m ³]
ρ_w	Water dencity	[kg/m ³]
σ_M	Entraped liquid ratio	[-]

Introduction



Figure 1.1: *Icing on KV Nordkapp on the 27th of February 1987, Barents Sea. Left picture show the fore-ship and the wheel house, right picture show the starboard walkway and railings [24].*

Icing is a natural mechanism where water droplets freeze on cold surfaces. For mobile units such as airplanes and ships this can cause severe safety issues. Icing can be divided into atmospheric icing, which is the most critical for airplanes, while marine icing is caused mainly by sea-spray and assumed to be the most serious for ships. Several methods are known to prevent icing problems such as surface heating, surface materials, and different methods for mechanical removal of ice. For marine vessels operating in Arctic waters, icing is a major safety concern. The weight of the ice can compromise the manoeuvrability and the stability of the ship, which have led to a numerous accidents and shipwrecks. It

is also very important for the safety on board a ship that escape routes, railings and life saving equipment are free of ice. The rapid ice growth due to polar lows and sea spray is a combination which can lead to a vessel covered with thick ice in just a few hours. An example is the marine icing observed on KV Nordkapp, where 110 tons of ice accumulated in 17 hours [24]. The ship was covered in ice from the deck railing to the top of the wheel house shown in Figure 1.1.

Polar lows are special weather conditions, which occurs due to cold-airflow over relatively warm seawater, accompanying strong winds (15-30m/s), high wave heights and cloudy snowy weather. A study of icing on ships in northern seas of Japan showed that ice accretion occurred in the region of the southwest quadrant of the cyclone, where the cold air was below -18°C . The sea temperature was $0-2^{\circ}\text{C}$, winds between 20-30m/s (40-60kts), wave heights 3-7m and cloudy weather with heavy snow-showers [25].



Figure 1.2: Example picture to show that rough waves can make the sea splash all over the ship [2].

Icing can cause numerous of problems on a vessel. For example, stability issues as the ice grow on top of the ship causing the centre of gravity to change which can lead to capsizing. On larger ships with helicopter deck, icing can create landing problems preventing rapid evacuation in case of emergencies. Vital machines covered with ice will be difficult or even impossible to operate. Windows covered with ice leads to loss of visibility. Outdoor stairs and decks may be slippery and dangerous for the crew to use, especially in heavy sea motions (ref. figure 1.2). Railings may be irregular in shape and hard to grasp in case of slippery deck. Icing have been an issue as long as marine vessels has been operating in Arctic climates. A wide variety of technologies exists for de-icing, anti-icing and detecting ice. Most of these technologies are designed and currently used for other purposes, for example in aviation. As a consequence, not all technologies are applicable for offshore vessels, but some are more adoptable than others. The most commonly used technologies

for ships are structural design, electrical heating, high-velocity fluids and manual de-icing [23]. Structural design mitigating exposed surfaces for icing, is the most efficient method to reduce the hazard of icing. This method includes geometrical design in general, and covers to protect vital machines such as lifesaving equipment and other safety functions. The main purpose is to protect and reduce the area where the ice can accumulate. However, design for ice prevention may also hinder vital functions of the ship, such as the helicopter landing platform, which has to be placed where it is easy for the helicopter to land, normally at a top location on the ship. Icing in this high location on a ship is very critical for the stability, since the landing platform has a large surface for the ice to accumulate (ref. figure 1.3).



(a) Foto: Harald M. Valderhaug; Helideck placed at a top location of the ship [28].



(b) Potential ice accretion areas, by ice type, on the Ocean Rig semisubmersible Erik Raude ([21]), [23]

Figure 1.3: Principle picture to show which icing types are most current for ships.

Electrical heating, often used in form of heating elements inside the surfaces to prevent icing to occur or to melt already accumulated ice. This method works to remove the ice, but is not particularly energy efficient, since electrical power is generated by diesel generators at around 45% efficiency. Another factor may be that the ship does not have sufficient electrical power to use on heating, when power is needed for propulsion. High-velocity fluids like steam lances have been used to remove ice on ships. Hot water and steam jets can cut up to 1m thick ice. However, it can also damage the structure under the ice and also leave trace of water which can freeze and create a thin layer of new ice after removing the thick sea ice. Manual de-icing has been used from the beginning of ice removal on marine vessels. Wooden mallets and shovels are example of equipment that were used and still are used remove ice on ships. This is very hard, inefficient and dangerous method of removing the ice. Manual de-icing can be used in combination with heating when it is safe for the crew to operate on deck [23].

Most research studies of icing are made by researchers in countries that have a coastline towards to the Arctic areas. The main studies in this field are conducted by universities in Norway, Russia, Canada and Japan. Models for icing, anti-icing and de-icing found in earlier studies are mainly empirical, based on experiments and numerical simulations, field and laboratory studies. Horjen presented in his PhD Thesis (1990) several numerical models for calculating the ice accretion and heat energy consumption; Ice accretion

from sea spray, necessary heat power to prevent icing from sea spray (Anti-Icing) and necessary heat to remove an ice layer formed by sea spray (De-Icing). The new icing model ICEMOD, originally called ICING consisting of a package of several sub-models to be used for time-analysis of various aspects of ice accretion and icing prevention. Horjen's research is a part of a joint Canadian/Norwegian icing projects for evaluating the two icing models ICEMOD and RIGICE, which is a steady state Canadian model (Roebber and Mitten, 1987). This project was performed by NTH and the Canadian Atmospheric Environment Service (AS) and is reported in detail by Brown and Horjen (1989) [13] [22]. Kulyakhtin presented in his PhD Thesis (2014) a new icing model which includes heat flux into the accreted ice based on CFD analysis. The new model by Kulyakhtin was compared to existing models of icing (ICEMOD and RIGICE04), which both have neglected the heat flux into the accreted ice. This study proves numerically and experimentally that the heat flux into the accreted ice generated by freezing should not be neglected. During this study, experiments of sea spray icing were conducted and compared with numerical modelling. The PhD Thesis explains how the ice growth occurs in detail and how the salinity change as the saline water freeze to ice [18]. Samuelsen, Løseth and Edvardsen (2015) presented a comparison of the icing event that occurred on the Norwegian Coast Guard vessel KV Nordkapp in 1978 with a sea spray model [24].

Charles C. Ryerson (2010) made a study of various types of icing and de-icing methods on offshore structures. It focuses on safety of offshore oil-platforms and rank various hazards along with the probability of the different types of icing. This research is relevant, since oil and gas exploration activities are moving into Arctic offshore areas [23].

The international maritime organization (IMO) issued the "Polar Code" [15] into force from 1. January 2017, which regulate safety of ships operation in Arctic areas (North and south of 60° latitude). DNV GL rules for classification (2017) [6] contain procedural and technical requirements related to class certificates. The rules represents all requirements adopted by the society as basis for classification. This document contains the classifications for ships operating in cold climate, and are used as a base for the modelling conditions in this study .

Problem formulation

Ulmatec Pyro is a company that specialises on heating systems for ships based on waterborne heat. The company designs system for ships and marine vessels to utilize waste heat for heating the water on board for showers, heating indoor etc. Heat-exchangers uses engine cooling water and exhaust gases to heat the water up to 90°C. This water can also be used for de-icing as a central heating system in for example railings, escape routes, helidecks etc. The heating technology is similar to electrical heating, except that waterborne waste heat is used instead of electricity. Using waste heat is more energy efficient and environmentally friendly than electrical heating. If de-icing requires more energy than is produced by waste energy, it is also possible to produce hot water from the engine or heaters [27]. Ulmatec Pyro has patented a design technology based on a double pipe principle. The main idea behind the technology is to achieve a more even surface temperature along the length of the pipe, compared to a single pipe. The principle is to send a warm water flow through the innermost pipe, then turn the flow into the outer pipe. The returning

”cold” water that goes back into the outer pipe will be heated by the ”warm” water in the inner pipe on its way back to the outlet resulting with an even temperature on the de-icing surface. Figure 1.4 show the principle of the de-icing technology by Ulmatec Pyro. The patent description and more detailed information can be found in [1].

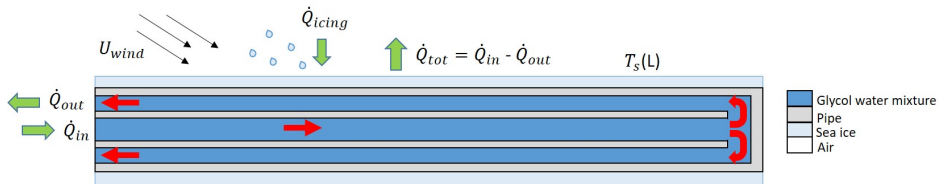


Figure 1.4: Principle drawing of the de-icing technology design by Ulmatec Pyro

De-icing using waste heat is a new technology for Ulmatec Pyro, and they have asked NTNU for assistance to establish knowledge related to icing, and de-icing methods. This is the background for this Master Thesis. Theoretical background studies on mechanism of icing and thermodynamics/heat transfer processes related to de-icing were conducted through a pre-project.

Objectives

The main objective of this master thesis project is to build knowledge for design and operation of waterborne heating systems for anti-icing and de-icing, through a combined numerical and experimental approach. The goal is to be able to calculate the heat required to keep critical surfaces free of ice under icing conditions (ref. figure 1.1), the heat required to remove ice after a severe icing incident, and further optimize the design parameters of the Ulmatec Pyro double-pipe system (ref. figure 1.4).

Scope of work

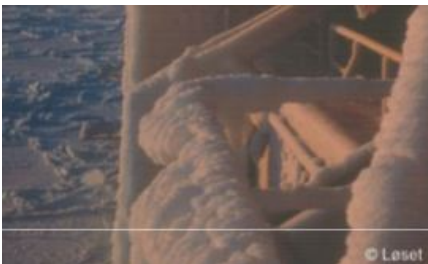
The total project (pre-project and master thesis) is planned to cover:

- Theoretical background studies on mechanism of icing and thermodynamics/heat transfer processes related to anti-icing and de-icing.
- Establish heat transfer models for typical anti-icing and de-icing cases.
- Develop numerical simulation models for anti-icing and de-icing.
- Perform simulations to establish boundary conditions and main design parameters.
- Plan and prepare experimental studies to verify and calibrate the theoretical models.
- Perform experiments and compare the results with the numerical simulation models.

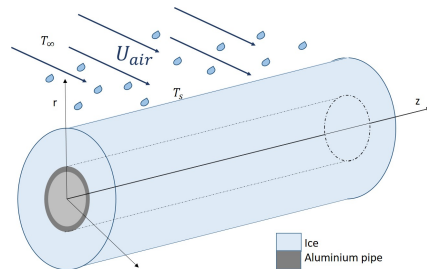
Theory

Anti-icing and de-icing are problems mainly covered by heat transfer theory, by Cengel and Ghajar (2015) [29]. Anti-icing is mainly a problem of providing a sufficient heat flux to keep surface temperatures above the freezing conditions of the water droplets. This is relatively simple theory, except for the convection conditions in the boundary layer of the surface involving both liquid droplets and air flow. And further the heat transfer through a phase changing material such as ice during de-icing is a very complex problem. Hence, analytically solutions are only possible if many assumptions and simplifications are implemented. The models for icing, anti-icing and de-icing found in previous studies are empirical and numerical models ref. [13], [18] and [22].

Ulmatec Pyro intends to use their anti-icing technology on railings, escape routes and helicopter platforms. Of these mentioned, railings have the simplest geometry to calculate and simulate the de-icing process. Hence, this study focuses on icing on horizontal cylinder geometry. Figure 2.1a shows railings that have been exposed to severe icing on-board KV Nordkapp 1987, [18].



(a) Ice accretion on the railings on KV Nordkapp. Photo by Prof. Sveinung Løset, [18].



(b) Principle drawing of icing on railings.

Figure 2.1: Ice accretion on railings.

This chapter presents theoretical background for icing, anti- and de-icing models, and heat transfer methods. The first part cover icing processes, second part covers anti-icing methods, and the third part covers heat transfer models for pipes designed by Ulmatec Pyro. Part of the theoretical background in this chapter is also covered by the pre-project report.

2.1 Icing as a phenomenon

As mentioned in the introduction, icing can be divided into atmospheric- and marine-icing. The latter is assumed to be the most serious for ships operating in Arctic environment. Hence, the theoretical background will focus on marine icing, which is a complex process involving cold air flow with sea water droplets, water salinity, air and surface temperatures as the main driving forces. The combination of sea-spray, snow and cold air flow with relatively high velocities creates an environment for rapid ice growth.

Sea ice is more complex than fresh water due to variable salinity through the ice layers. Schwerdtfeger (1969) present thermal properties of sea ice [26]. It contains mathematical modelling of the thermal properties of sea ice, which are compared with pure ice and experimental values. Hajo (1992) present a salinity model of sea ice. Field data have been compared with "ideal" salinity profiles generated by a simulation scheme based on thermodynamic growth under climatological conditions representative of the Weddell Sea. The composite salinity profiles agree well with simulations [7]. The physical properties of sea ice are strongly dependent on salinity, temperature and time. This article was very useful to understand the thermal properties of sea ice. Results from this article were used in the project thesis.

2.1.1 Marine icing models

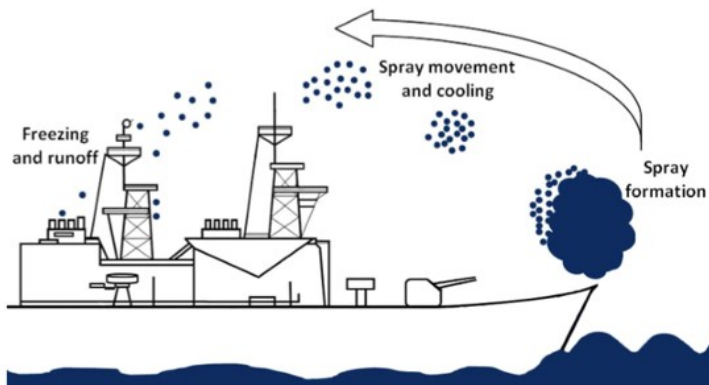


Figure 2.2: Marine icing due to sea spray (ref. Dehghani-sanij et.al) [5].

Marine icing is icing due to sea spray freezing onto the surface. Sea spray occurs due to wave collisions with the vessel (impact-generated) and wind-generated spray from the sea. At high wind velocities wind-generated spray will dominate [13], [12]. Figure 2.2 is a principle drawing showing how the sea spray is generated and how it spreads onto the vessel.

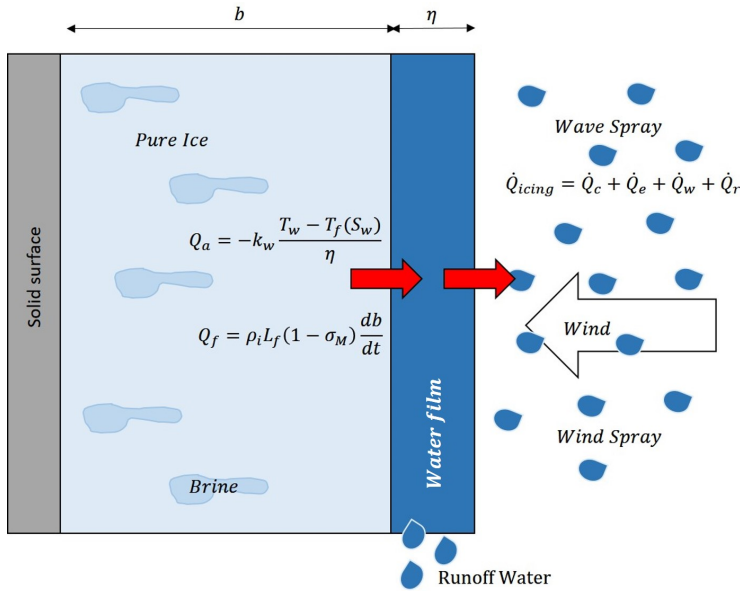


Figure 2.3: Principle drawing of the thermodynamic processes of icing, [18] [5].

When sea water cools down to its freezing point, crystallization of pure ice starts. The salt concentration of the water film (brine) increase due to pure ice growth. The brine will remain in contact with the sea spray while the icing take place. While the freezing process continues, some pockets of brine are cut off from the water-film, and as a result the accumulated ice contains of pure ice, brine, solid salt and air bubbles. As a result due to the reduction of salt concentration in the icing process, the salinity of the accumulated ice is lower than the salinity of sea water. From previous research it is found that for temperatures between $-8.2\text{ }^{\circ}\text{C}$ and $0\text{ }^{\circ}\text{C}$, essentially all salts trapped within the sea ice are in a water solution. Hence, the thermal properties of sea ice are affected by the salinity [26]. As stated in the pre-project, saline water can be modeled as pure water as an assumption for simplified calculations. In addition, ice with a lower temperature than $-8\text{ }^{\circ}\text{C}$ can also be modeled as pure ice. Figure 2.3 show an overview of the thermodynamic processes and heat transfers during the icing process, which can determine the icing rate. The super-cooled water droplets freeze due to several heat transfer rates at the interface between the air and water. Heat transfer rates which are involved in the process; heat capacity of impinging \dot{Q}_w , Radiation \dot{Q}_r , Convection \dot{Q}_c , Evaporation \dot{Q}_e , conductive heat flux \dot{Q}_a , latent heat flux \dot{Q}_f due to freezing, kinetic energy of incoming droplets \dot{Q}_k and aerodynamic heating \dot{Q}_v . \dot{Q}_k and \dot{Q}_v are generally very small and therefore they are ne-

glected. The heat balance at the *air - water film interface* gives the following equation: [5]

$$\dot{Q}_a = \dot{Q}_c + \dot{Q}_e + \dot{Q}_w + \dot{Q}_r \quad (2.1)$$

Which also can be written as;

$$-k_w A_s \frac{T_w - T_f}{\eta} = \dot{Q}_c + \dot{Q}_e + \dot{Q}_w + \dot{Q}_r \quad (2.2)$$

Where T_w is the water film temperature, T_f is the freezing temperature, A_s is the heat transfer surface area, k_w is the thermal conductivity of the water film and η is the water film thickness. The heat generated at the *ice - water interface* is conducted through the water film through the *water film - air interface* which is equal to the heat transfer rate to the air ($\dot{Q}_a = \dot{Q}_f$) [5], [18]. Hence, the equation can be written;

$$\rho_i L_f A_s (1 - \sigma_M) \frac{db}{dt} = -k_w A_s \frac{T_w - T_f}{\eta} = \dot{Q}_c + \dot{Q}_e + \dot{Q}_w + \dot{Q}_r \quad (2.3)$$

Where $L_f(1 - \sigma_M)$ is the latent heat of fusion of saline water ($\sigma_M = 0$ for pure water), ρ_i is the density of the accumulated ice, b is the ice thickness and t is the time. For more detailed derivation of these formulas see (Kulyakhtin, Anton 2014 [18]) and (Dehghani, Alireza and Muzychka, Yuri and Naterer, Greg 2015 [5]).

2.1.2 Saline water icing

For temperatures below $-8.2^\circ C$ saline ice and pure ice have similar thermal properties. Hence, saline ice can be assumed having the same thermal properties as pure ice [26]. The same applies to saline water and pure water, the salinity has a minor effect on the thermal properties in the temperature range $0^\circ C - 80^\circ C$ which also can be assumed as pure water for modelling and calculation purposes. For experimental purposes it is desirable to test with fresh water icing inside the lab due to corrosion and other maintenance arguments. The main difference of icing with pure water compared to saline water is the freezing temperature which is dependent on salinity of the ice. The freezing temperature decreases as the salinity increases. By assuming thermal properties of fresh water for modelling purposes of the de-icing process gives conservative results.

2.1.3 Periodic icing processes

Icing on marine vessels will appear as periodic icing due to wave generated spray. Hence, modelling of marine icing should therefore be periodic. The spray period and duration is varying due to the weather conditions and the wave parameters. Figure 2.4 show the ice growth caused by periodic icing: (1) As a "new" spray hits the structure, the water cools down to its freezing point and the freezing starts. (2) As the freezing continues the salinity of the water film increases, as a result the freezing point temperature decreases creating a temperature gradient in the formed ice. This continues until the salinity of the water film

reaches its maximum where the freezing temperature is the same as the air temperature. (3) The ice growth stops since the water film cannot become cooler than the air temperature, only freezing of entrapped water (brine pockets) happens at this step. The system stays in its thermal balance until the next spray event happens (4). The ice thickness is thicker since the previous spray event. Hence, the initial conditions are different from the previous spray. For temperatures below -23°C the water freezes with all the salt contained in the ice. Hence, this periodic freezing model is only valid for temperatures between 0°C and -23°C [18].

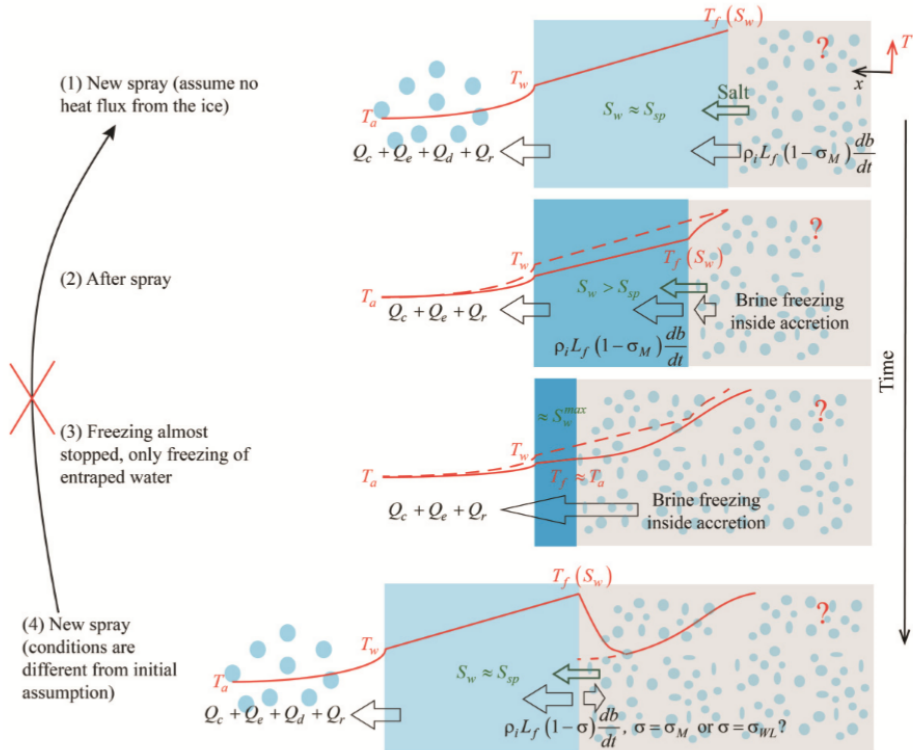


Figure 2.4: "Scheme of the ice growth caused by periodic sea spray. The black arrows represent the directions of the heat fluxes. The solid red line represents the temperature profile in the water and ice accretion. The dashed red line represents the temperature profile in the previous step." [18]

2.2 Heating requirements for icing prevention

Marine vessels which are made for Arctic environments need to be classified for operating in Arctic conditions. DNV GL is an international classification society which can issue certifications confirming that IMO regulations are met [15], ref table 2.1 and table 2.2 [6]. Depending of the classification of each vessel, different heating may be required for anti-icing and de-icing. For safety regulations regarding maximum surface temperature on

railings and escape routes, no upper limit is required from the class notation for anti-icing and de-icing. This is due to energy saving reasons because anti- and de-icing are very energy demanding processes. Hence, it is advisable to set the surface temperature just above the minimum temperature limit.

Table 2.1: DNV GL’s document Rules of classifications on ships; *Class notation Winterized (Table A1)* [6]

Table A1 Class notation Winterized				
<i>Class notation</i>		<i>Qualifier</i>		
<i>Name</i>	<i>Description</i>	<i>Name</i>	<i>Description</i>	<i>Requirements</i>
Winterized	Operation in cold climate	Basic	Operation occasionally in cold climate for short periods.	A110, B and C
		Cold	Operation in cold climate regularly or for an extended period of time, though not necessarily in ice-infested waters.	A110, B and C
		Polar	Operation in extreme cold climate of the polar regions year-round, in ice infested waters.	A110, B and C
		t_d	Design Temperature.	A108
		Enchanted	Additional requirements of a higher level of winterization.	A106

Table 2.2: DNV GL’s document rules of classifications on ships; *Typical design environmental conditions (Table A2)*. [6]

Table A2 Typical design environmental conditions			
<i>Qualifier</i>	<i>Air temp [t_d]</i>	<i>Sea water temp</i>	<i>Wind speed</i>
Basic	$\leq -10^\circ C$ ($-10^\circ C$ is default)	$+4^\circ C$ without ice class $-2^\circ C$ with ice class	20 [m/s]
Cold	$-15^\circ C$ to $-30^\circ C$	$+2^\circ C$ without ice class $-2^\circ C$ with ice class	20 [m/s]
Polar	$< -25^\circ C$	$-2^\circ C$	20 [m/s]

To decide for which conditions to simulate the de-icing process, DNV GL's rules for classification of ships have been considered. Table 2.1 show the class notation Winterized and with relevant qualifiers, Basic, Cold and Polar. Table 2.2 represent the typical design environmental conditions for these qualifiers. The design temperature t_d is the mean daily average air temperature in the intended area of operation.

For the qualifier Polar, the design temperature is not specified further than lower than -25°C . For calculations where the most extreme temperature over the day is relevant, the air temperature can be set 20°C lower than the design temperature in the notation. If no specification of the design temperature has been given, the values -35°C for notations PC(1) to PC(5) and -25°C for notations PC(6) and PC(7) will be considered.[6] Hence, required design condition for testing and calculations is thereby; Basic -10°C , Cold -30°C and Polar -45°C . These conditions will be taken into consideration in further calculations and numerical simulations.

2.2.1 Anti-icing requirements

Anti icing is basically avoiding ice to form on a surface by applying high temperature to the surface, using a heat source inside the surface. If no icing is allowed at all, the DNV GL's rules of classifications require a minimum surface temperature of $+3^\circ\text{C}$;

103. *The heating capacity for anti-icing and anti-freezing arrangements shall be sufficient to prevent icing or freezing under the design environmental conditions. Anti-icing and anti-freezing arrangements must be able to maintain a surface temperature of at least $+3^\circ\text{C}$ under the design environmental conditions.* [6]

Due to extreme weather conditions, avoiding ice to grow is very energy demanding. Instead, icing is allowed in extreme conditions and then heat is applied to remove the ice when the conditions are back to "normal". This way energy consumption can be reduced [13].

2.2.2 De-icing requirements

De-icing is removing ice which has accumulated on a surface. Due to the insulation effect of the ice, the de-icing process require a lower effect than by anti-icing heating method. The energy of de-icing per unit area is defined by;

$$E_m = \dot{Q}_{tot} t_m \quad (2.4)$$

Where \dot{Q}_{tot} is constant power of heat supplied by the heat source, and t_m is the necessary de-icing time [13]. The heat source shown in figures 2.5 and 2.6 is glycol water mixture circulation from a waste heat recovery system. The waterborne heat running through the inner pipe with a inlet velocity U_{in} and temperature T_{in} is heating the outer pipe flow from the inside. This fluid flow leaves the system with a lower temperature T_{out} and a outlet velocity U_{out} . Here, \dot{Q}_{tot} is the heat supply melting the sea-ice, while the cold air is removing heat by forced convection due to the air velocity U_{air} . The loss due to forced convection is negligible while the ice is thick, the ice works as an insulating layer. Hence,

the total energy supplied to the system is used for melting the ice and heating the entrapped melted water can be assumed.

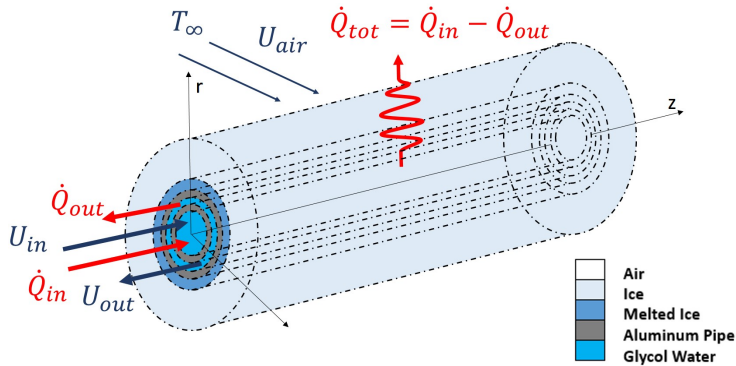


Figure 2.5: Principle of de-icing process of a horizontal cylinder using waterborne heat through a double pipe.

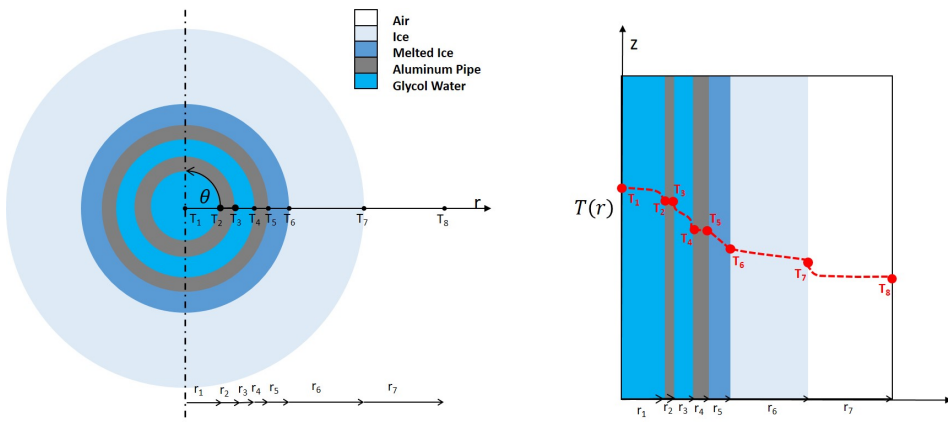


Figure 2.6: Principle Drawing of the de-icing process for a horizontal cylinder, here represented in 2D and 1D. $T(r)$ represent the temperature distribution throughout the cylinder as a function of the radius.

2.3 Heat transfer

Heat transfer is the exchange/transfer of thermal energy and heat due to temperature differences. This process can be divided into various mechanisms such as, thermal convection, thermal conduction, thermal radiation and energy by phase change. Heat transfer through a system is usually a combination of these mechanisms which gives complex systems that needs to be calculated or modelled. There are several modelling approaches which can

be used to calculate heat transfer of different systems such as; solving the heat equation, lumped capacitance method and finite difference method. In some cases these methods can be combined to simplify and calculate a complex system [3].

2.3.1 Heat transfer mechanisms

The amount of heat transferred throughout a process is denoted Q , and the amount of heat transfer per unit time, also called heat transfer rate is denoted \dot{Q} [29]. The heat transfers over the time period Δt is given by (2.5);

$$Q = \int_0^t \dot{Q} dt \quad (2.5)$$

The rate of heat transfers per unit area normal to the heat transfer direction is called heat flux, ref. equation 2.6. In solids, heat flux is always by conduction since the molecules in a solid is relatively fixed in the structure. In gases or liquids, the molecules are not fixed in the structure and the heat transfer can be by conduction or convection depending on the motion of the fluid. The rate of heat transfer through a fluid in motion (for example fluid running through a pipe or wind in the air.) is much higher by convection than conduction. Increasing velocities causes increased rate of heat transfer [29].

$$\dot{q} = \frac{\dot{Q}}{A_s} \quad (2.6)$$

Thermal conduction

The transfer of heat from more energetic particle to less energetic ones, expressed by Fourier's Law [29]:

$$\dot{Q}_{cd} = -kA_s \frac{dT}{dx} \quad (2.7)$$

Where k is the conductivity of the material, which can be a constant or a function of temperature $k(T)$. Especially for fluids the thermal conductivity varies with temperature.

Convective heat transfer

The transfer of heat in fluids, which can be divided into natural- and forced- convection. Natural convection occurs due to difference in temperature which affect the material properties of the fluid, such as density. The heavier fluid will fall and the lighter will rise, the motion of fluid is due to the temperature difference. Forced convection is caused by movement in the fluid due to external forces, for example wind velocity and fluid flow through a pipe. Hence, natural convection is driven by the temperature differences and density gradients, while forced convection is driven by the fluid flow. Convection is taking place through the boundary layer of the fluid at the surface of the solid object. The average temperature (T_{avg}) in the thermal boundary layer is used to simplify and bring the effect of the boundary layer into the calculations. Hence, average bulk temperature for the thermal boundary layer is assumed (ref. figure 2.7 and equation 2.8).

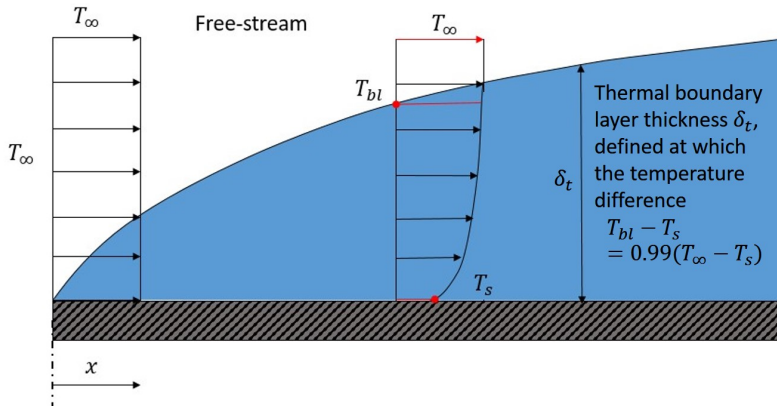


Figure 2.7: Schematic drawing of the thermal boundary layer.

$$T_{avg} = \frac{T_s + T_\infty}{2} \quad (2.8)$$

The transfer of heat occurring because of fluid motion (convection) is given by the heat transfer coefficient h , surface area A_s and temperature difference through the boundary layer, ref. equation 2.9. The heat transfer coefficient is dependent on the conductivity of the fluid k , the characteristic length L_c (for pipes $L_c = D$) and Nusselts number Nu , ref. equation 2.10.

$$\dot{Q}_{cv} = h(T_{avg})A_s(T_s - T_\infty) \quad (2.9)$$

$$h(T_{avg}) = \frac{k(T_{avg})}{D} Nu(T_{avg}) \quad (2.10)$$

Nusselts number is the ratio of convective to conductive heat transfer normal to the boundary. This number depends on the geometry of the structure and the temperature in the fluid. An overview of the relevant Nusselt number for this master thesis is listed in table 2.4. For the double pipe design the internal flow in the outer pipe is flowing through an annulus. The Nusselts number for internal forced convection of an annulus is the same expression as for a pipe where the hydraulic diameter D_h represents the annulus (ref equation 2.11), where d_2 is the outer diameter of the annulus and d_1 is the inner diameter of the annulus [29].

$$D_h = (d_2 - d_1) \quad (2.11)$$

Combined convection is the correlation between natural and forced convection, ref. equation 2.12. The plus sign is for transverse- and assisting- flows, and the minus sign correlates to opposing flows. The exponent n varies between 3 and 4 depending on the geometry involved. It is observed that $n = 3$ correlates experimental data for vertical surfaces well.

For horizontal surfaces a large value of n is suitable [29]. For horizontal transverse flows a value of $n = 4$ is used.

$$Nu_{combined} = (Nu_F^n \pm Nu_N^n)^{\frac{1}{n}} \quad (2.12)$$

Table 2.3 contains an overview of the dimensionless parameters used for calculating and evaluating validity of Nusslets numbers (ref. table 2.4), considerations whether the flow is laminar or turbulent, and for other heat transfer evaluations. The thermal expansion coefficient (β) used in equation 2.19 and equation 2.21 (ref. table 2.3), is given by equation 2.13.

$$\beta(T_{avg}) = \frac{2}{T_s + T_\infty} = \frac{1}{T_{avg}} \quad (2.13)$$

Radiation

At atmospheric temperatures the radiation effect is very small compared to conduction and convection. Hence, radiation is neglected in this study.

Impinging water droplets

Ice accretion rate depends on the amount of water impinging on the surfaces, which is determined by the air flow around the surfaces of interest. The heat flux due to impinging depends on the specific heat capacity of the water c_p , the spray flux F_d and the spray T_d and film temperature T_f . [18]

$$\dot{Q}_d = A_s c_p F_d (T_d - T_f) \quad (2.14)$$

Evaporation of water

The heat flux due to evaporation is substantial. It is comparable to heat flux due to convection. For wind generated spray (small droplets), evaporation leads to an increase of the salinity in the droplets, which can be as much as 8 times the salinity of the sea water at 80% air humidity. For denser spray (big droplets), the the rate of heat transfer will decrease due to temperature change in the droplet temperature. Hence, heat flux due to evaporation is dependent of air humidity, droplet size and water vapour. [18]

$$\dot{Q}_e = hEA_s(r_H e(T_a) - e(T_w)) \quad (2.15)$$

Where E is a coefficient, for details see Lozowski [19], r_H is the relative humidity of air and $e(T)$ is a saturated water pressure function of temperature.

Table 2.3: Definitions and equations of dimensionless parameters used in heat transfer calculations.

Number	Equation	Significance	Reference
Biot	$B_i = \frac{hL_c}{k}$ (2.16)	Thermal resistance ratio.	[3]
Nusselt	$Nu = \frac{hL_c}{k}$ (2.17)	Ratio of convective to conductive heat transfer normal to the boundary layer, geometry and temperature dependent.	[29]
Reynolds	$Re = \frac{\rho u L_c}{\mu}$ (2.18)	Ratio of internal forces to viscous forces within a fluid.	[29]
Grashof	$Gr = \frac{g\beta\Delta T L_c^3}{\nu^2}$ (2.19)	Ratio between buoyancy force and the viscous force	[29]
Prandtl	$Pr = \frac{c_p\mu}{k}$ (2.20)	Ratio of viscous diffusion rate to thermal diffusion rate.	[29]
Rayleigh	$Ra = \frac{g\beta\Delta T L_c^3 Pr}{\nu^2}$ (2.21)	Product of Prandtl and Grashofs number. Value define if the flow is natural convection driven or forced convection driven.	[29]

Table 2.4: Nusselt numbers for various geometries relevant for this thesis (ref. [29]).

Significance	Equation (number)
Natural convection of a horizontal cylinder:	$Nu_N = \left[0.6 + \frac{0.387 * (Ra_D)^{\frac{1}{6}}}{\left[1 + \left(\frac{0.599}{Pr} \right)^{\frac{9}{16}} \right]^{\frac{8}{27}}} \right]^2 \quad (2.22)$ <p style="text-align: center;">Valid for $Ra_D \leq 10^{12}$</p>
External forced convection of a cylinder with cross-flow:	$Nu_F = 0.3 + \left[\left(\frac{0.62(Re)^{\frac{1}{2}} Pr^{\frac{1}{3}}}{\left[1 + \frac{0.4}{Pr} \right]^{\frac{1}{4}}} \right) \left(1 + \left(\frac{Re}{282000} \right)^{\frac{5}{8}} \right)^{\frac{4}{5}} \right] \quad (2.23)$ <p style="text-align: center;">Valid for $RePr \geq 0.2$</p>
External forced convection of a plate with parallel to the surface:	$Nu_F = 0.664 Re_L^{\frac{1}{2}} Pr^{\frac{1}{3}} \quad (2.24)$ <p style="text-align: center;">Valid for $Re_L < 5 * 10^5, Pr > 0.6$</p>
Internal forced convection of a pipe:	$Nu_F = \frac{\frac{f}{8} * (Re_D - 1000) * Pr}{1 + \left[12.7 * \left(\frac{f}{8} \right)^{0.5} * \left(Pr^{\frac{2}{3}} - 1 \right) \right]} \quad (2.25)$
Where;	$f = (0.790 \ln(Re) - 1.64)^{-2} \quad (2.26)$ <p style="text-align: center;">Valid for $3 * 10^3 < Re_L < 5 * 10^6, 0.5 \leq Pr \leq 2000$</p>
	$f = 3.03 * 10^{-12} Re^3 - 3.67 * 10^{-8} Re^2 + 1.46 * 10^{-4} Re - 0.151 \quad (2.27)$ <p style="text-align: center;">Valid for $2300 < Re_L < 45000$</p>
	$Nu_F = 4.36 \quad (2.28)$ <p style="text-align: center;">Valid for $2300 < Re, \dot{q}_s = constant$</p>

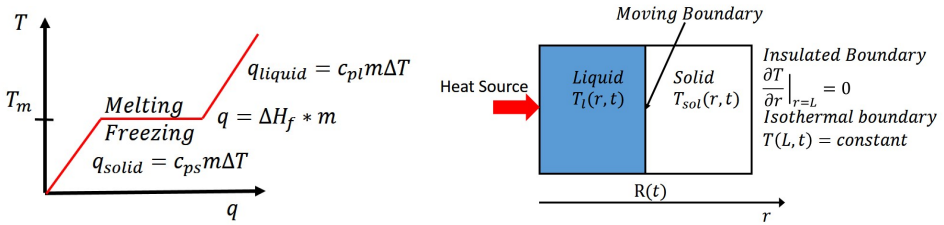
Phase change from solid to liquid

Melting and freezing is the transition of solid to liquid phase and liquid to solid phase. The thermodynamic process of a phase change transition can be explained using the heat equation (ref. equation 2.29), which is a partial differential equation (PDE) describing the heat distribution over a period of time. Heat equation in polar coordinates (r, θ, z) : [3]

$$\frac{1}{r} \frac{\partial}{\partial r} (kr \frac{\partial T}{\partial r}) + \frac{1}{r^2} \frac{\partial}{\partial \theta} (k \frac{\partial T}{\partial \theta}) + \frac{\partial}{\partial z} (k \frac{\partial T}{\partial z}) + \dot{q} = \rho c_p \frac{\partial T}{\partial t} \quad (2.29)$$

The freezing process were explained in section 2.1.1. Hence, an example of the melting process will be done here. For a 1D problem in radial direction ($\frac{\partial}{\partial \theta} = 0$ and $\frac{\partial}{\partial z} = 0$) with a constant heat source ($\dot{q} = 0$) the heat equation is given as:

$$\frac{1}{r} \frac{\partial}{\partial r} (kr \frac{\partial T}{\partial r}) = \rho c_p \frac{\partial T}{\partial t} \quad (2.30)$$



(a) Temperature plot of the moving boundary interface (ref figure 2.8b) of supplied energy due to phase change.

(b) Schematic drawing of melting showing the boundary conditions. [14]

Figure 2.8: Phase transition of melting ice.

For the phase change interface the the temperature will be constant and equal to the melting temperature during the phase change process, and all the heat supplied to the system is absorbed in the phase transition (ref. figure 2.8). Hence, insulated boundary and isothermal boundary conditions. Figure 2.8b is a schematic drawing of the melting process, which show the two phases (liquid and solid) with boundaries. The heat transfer in the liquid region is given by;

$$\frac{1}{r} \frac{\partial}{\partial r} (kr \frac{\partial T_l}{\partial r}) = \rho c_p \frac{\partial T_l}{\partial t} \quad (2.31)$$

The heat transfer in the solid region is given by;

$$\frac{1}{r} \frac{\partial}{\partial r} (kr \frac{\partial T_{sol}}{\partial r}) = \rho c_p \frac{\partial T_{sol}}{\partial t} \quad (2.32)$$

The heat transfer equilibrium at the interface give the following equation;

$$\rho c_p \frac{\partial T_{sol}}{\partial t} - \rho c_p \frac{\partial T_l}{\partial t} = H_f \rho \frac{dr}{dt} \quad (2.33)$$

Where H_f is the specific heat of fusion and $\rho \frac{dr}{dt}$ is the mass per unit area. The heat required to melt the water is given by the specific heat of fusion (ref. equation 2.33). Due to the insulated boundary (ref figure 2.8b), the effect of the heat source determines the melting time [14].

Overall heat transfer coefficient

$$\dot{Q}_{tot} = h_{tot} A_{ref} (T_{in} - T_{\infty}) \quad (2.34)$$

The overall total heat transfer is given by equation 2.34, where h_{tot} is the overall heat transfer coefficient and A_{ref} is the reference area, here the outside of the outer pipe wall. This coefficient is calculated from the total resistance through the body.

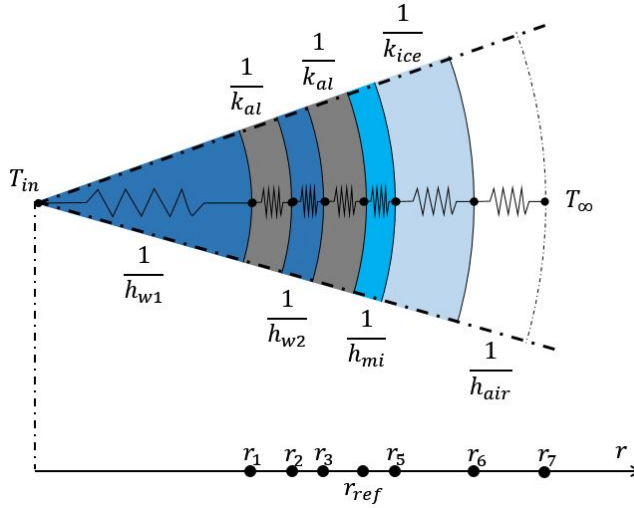


Figure 2.9: Thermal resistant network through the body. The reference area A_{ref} is marked at the inside of the pipe wall.

The outer radius of the outer pipe is chosen as the reference radius due to easy access to measure (ref. figure 2.9). The overall total heat transfer coefficient per unit length with respect to the reference area is given by [29];

$$h_{tot} = \frac{1}{\frac{r_{ref}}{h_w1 r_1} + \frac{r_{ref}(r_2 - r_1)}{k_{al} r_2} + \frac{r_{ref}}{h_w2 r_3} + \frac{r_{ref}(r_{ref} - r_3)}{k_{al} r_{ref}} + \frac{r_{ref}}{h_{mi} r_5} + \frac{r_{ref}(r_6 - r_5)}{k_{ice} r_6} + \frac{r_{ref}}{h_{air} r_7}} \quad (2.35)$$

2.3.2 Modelling approaches

Finite difference method

In some simple cases the solution to the heat equation (ref. equation 2.29) is exact due to analytical calculations, in other more complex systems the heat equation has to be calculated numerically. Finite-difference methods are numerical methods by approximating the differential equations with difference equations where the derivatives are represented by finite difference approximation. By assuming 2D axisymmetrical geometry ($\frac{\partial}{\partial \theta} = 0$) and introducing the integers p - time-step, m - radial-direction and n - longitudinal-direction, the time derivative can be approximated using the backwards difference approximation [3];

$$\frac{\partial T}{\partial t} \Big|_{m,n} \approx \frac{T_{m,n}^p - T_{m,n}^{p-1}}{\Delta t} \quad (2.36)$$

On the first-order derivative the backward difference approximation is used, and for the second-order term the central difference approximation on the radial derivatives giving;

$$\frac{\partial T}{\partial r} \Big|_{m,n} \approx \frac{T_{m,n}^p - T_{m-1,n}^p}{\Delta r} \quad (2.37)$$

$$\frac{\partial^2 T}{\partial r^2} \Big|_{m,n} \approx \frac{T_{m+1,n}^p - 2T_{m,n}^p + T_{m-1,n}^p}{\Delta r^2} \quad (2.38)$$

The central difference approximation is used on the second-order longitudinal term:

$$\frac{\partial^2 T}{\partial z^2} \Big|_{m,n} \approx \frac{T_{m,n+1}^p - 2T_{m,n}^p + T_{m,n-1}^p}{\Delta z^2} \quad (2.39)$$

By using FDM on a complex problem where an analytical solution does not exist makes it possible to find an approximate solution to the problem.

Lumped capacitance method

The essence of the lumped capacity method is to assume that the temperature of a solid is spatially uniform at any instant during the transient process, which implies that the temperature gradients within the solid are negligible. The validity of the Lumped Capacitance Method is evaluated from the Biot number (ref. equation 2.16, table 2.3), which may be interpreted as a thermal resistance ratio. *In particular, if $B_i \ll 1$, the resistance to conduction within the solid is much less than the resistance to convection across the fluid boundary layer. Hence, the assumption of a uniform temperature distribution within the solid is reasonable if the Biot number is small, [3].* If $B_i < 0.1$, the error using lumped capacitance method is small.

Numerical simulation models

De-icing of the double pipe is a complex problem. Melting of ice is a two-phase problem and the materials included in the process have temperature dependent properties. The double pipe contain a counter flow where heat is exchanged between the inner and outer flow, and the heat transfer depend on the flow velocity applied to the system laminar or turbulent. Hence, a simplified 1D model without ice is used to simulate the heat transfer to get an initial understanding of the double-pipe system. These calculations will be used to study the parameters involved and further used to compare with experimental results. The system is also modelled in a CFD simulation environment (COMSOL Multiphysics), where a 2D axisymmetric geometry is used, and a phase change model ice/water is implemented. The experiments will be carried out with fresh water due to maintenance of the lab. Hence, fresh water is used for numerical simulation models to compare with laboratory experiments.

3.1 Ulmatec Pyro's double pipe design

As mentioned in the introduction, the main idea behind the Ulmatec Pyro double-pipe technology is to achieve a more uniform surface temperature along the pipe length compared to a single pipe. The principle is to send a warm water flow through the inner pipe, then return the flow through the annulus, ref. figure 3.1. The "cold" returning water in the annulus will be heated by the "warm" inner pipe, resulting in an even temperature on the pipe surface.

A theoretical hypothesis based on heat transfer theory is compiled as: *"In order to achieve a uniform surface temperature along the length of the pipe, most of the heat loss should occur from the inner pipe flow. In order to achieve this, the fluid velocity in the inner pipe should be slower than the velocity in the return annulus"*. Figure 3.1 show the expected surface temperature distribution of the double-pipe compared to a single pipe. The advantage of the double pipe design is the ability to transport heat in a longer pipe compared

to a single pipe. Hence, a double pipe is preferable to maintain an even and low surface temperature along the pipe length.

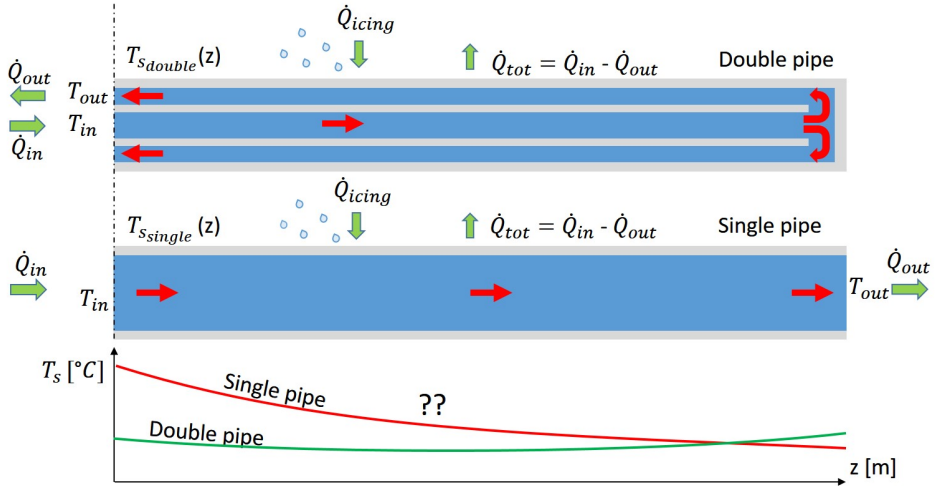


Figure 3.1: The principle of the Ulmatec Pyro double pipe technology. Temperature graph shows expected surface temperature for a double pipe compared to a single pipe.

The inner and outer pipe dimensions needs to be considered for heat transfer and flow calculations. To achieve a higher velocity in the return flow, the cross section area for the annulus needs to be less than the inner pipe (ref. figure 3.2). Introducing the velocity factor ($\frac{u_1}{u_2}$), where u_1 is the velocity in the inner pipe and u_2 is the velocity in the outer pipe. The hypothesis implies that a velocity factor lower than 1 is preferable. Railings are usually designed with an outer diameter of 50mm. Achieving a velocity factor below 1 can be challenging due to narrow annulus geometries. Figure 3.3 is a plot of the velocity factor due to the relative area ($\frac{A_1}{A_2}$), where A_1 is the cross section area of the inner pipe and A_2 is the cross section area of the annulus (ref. figure 3.2). Due to practical design limitations, area ratio higher than approximately 2.5 is not possible for these dimensions.

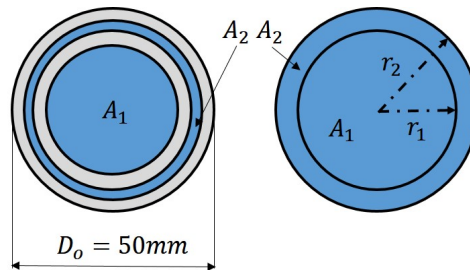


Figure 3.2: Principle drawing of the double pipe with and without thickness of the pipe wall, where A refer to the cross section area.

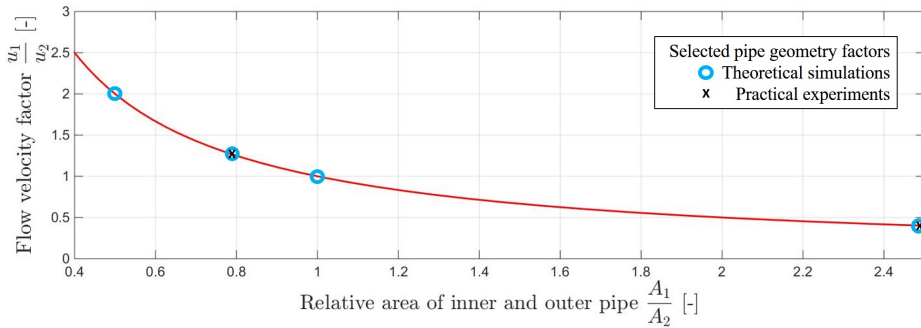


Figure 3.3: Plot of the velocity factor of various relative areas.

In the theoretical simulations in sections 3.2 and 3.3 four different velocity factors are selected ($\frac{u_1}{u_2} = [0.4, 1.0, 1.3, 2.0]$). For the practical experiments in chapter 4, two different factors are used ($\frac{u_1}{u_2} = [0.4, 1.3]$). Ref. to figure 3.3.

3.2 1D Axisymmetric heat transfer model

Finite difference method is used to model the steady state heat equation (ref. equation 2.29 where $\frac{\partial}{\partial t} = 0$). It is a non-linear problem due to temperature dependent material properties. Hence, iteration with a "starting" temperature vector $T^* = T_{in}$ is used to solve the boundary value problem. For each iteration the temperature vector T is calculated and compared with the temperature vector T^* , until convergence ($|T - T^*| < 10^{-3}$). Between each iteration step, the new temperature is set to $T^* = T$. Assumptions have been made to simplify the complex problem:

- Steady state ($\frac{\partial}{\partial t} = 0$).
- Average velocities are used, assuming fully developed flow ($\frac{D}{L_t} \ll 0.1$), [29].
- The bulk temperature of the fluid flow is used.
- Heat transfer models include the internal liquid flow and external air flow as free- and forced convection as a function of air velocity (ref. equations in table 2.4).
- With low thermal resistance ratio for the pipe walls ($B_i < 0.1$), lumped capacitance method is used (ref. section 2.3.2). This means that the pipe wall thickness is neglected (ref figure 3.2).
- Heat transfer caused by impinging water droplets and evaporation are not included.
- No heat loss at pipe end where the fluid flow turns.
- Constant surface heat flux for each element ($dL \ll L$ for sufficient number of elements m , ref. figure 3.4)
- Material properties for 50% glycol water mixture are used (ref. equations in Appendix section A.2).

Figure 3.4 show the principle drawing of the 1D axisymmetric model. The figure is drawn in 2D to show which elements and nodes that are connected. The light blue represent the inner flow, and the dark blue represent the outer pipe flow.

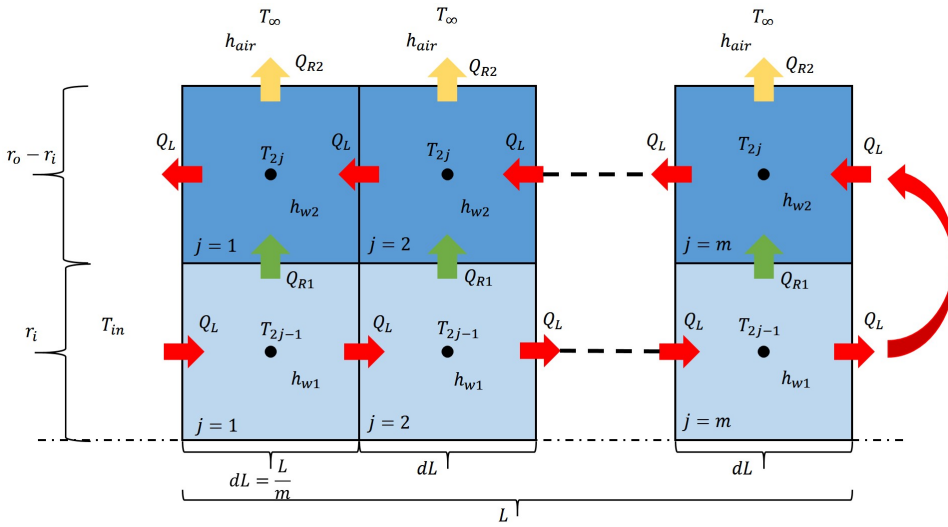


Figure 3.4: Principle drawing of the 1D axisymmetric heat transfer model.

Figure 3.5 show the first ($j=1$) element of the inner flow with connecting nodes. As seen in the figure, each element is assumed uniform bulk temperature. There is no heat transfer in the lower boundary due to symmetry. Q_L is the heat transport in the flow between the elements, where (\dot{m}) is the mass flow combined with the temperature dependent heat capacity ($c_p(T)$) combined into the thermal capacitance (C_L). Q_{R1} is the heat transfer through the inner pipe wall, which depends on the heat transfer coefficient of both water-flows ($h_{w1}(T)$ and $h_{w2}(T)$), and surface area of the inner pipe wall element ($A = 2\pi r_i dL$) combined into thermal resistance R .

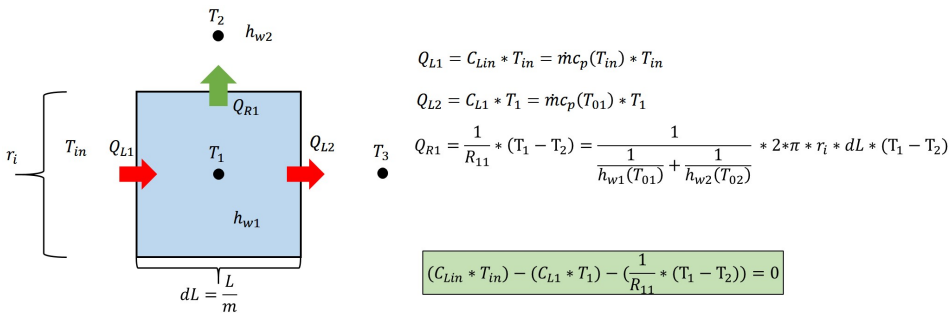


Figure 3.5: Principle drawing and equations for the first inner element of the 1D model, $j=1$.

The elements for the outer flow is shown in figure 3.6. Heat of the fluid flow is given as Q_{L1} and Q_{L2} , and the heat transfer through the inner wall is given as Q_{R1} which is the same as for the inner element. The main difference of these two elements (inner and outer flow) are the additional heat transfer through the outer wall Q_{R2} and the fluid flow in the

outer pipe is through an annulus. For the flow through the annulus the hydraulic diameter ($D_h = 2(r_o - r_i)$) is used for the calculations. The equations for heat transfer coefficient due to convection is found under Theory in chapter 2, table 2.4.

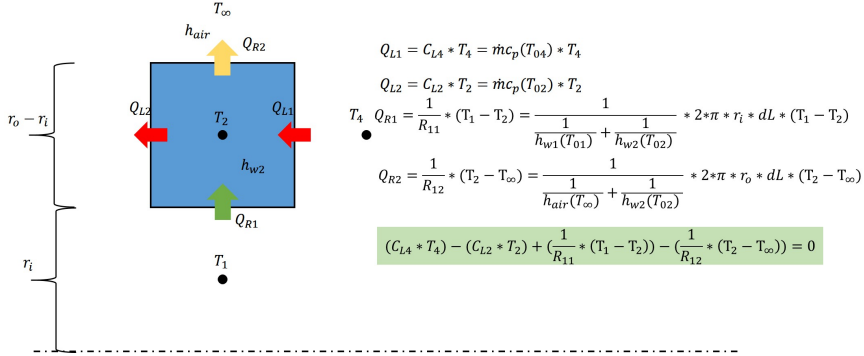


Figure 3.6: Principle drawing and equations for the first outer element of the 1D model, $j=1$.

The equations shown in figure 3.5 and figure 3.6 are combined for energy conservation of the system, giving as a set of equations written in a matrix form $A(T^*) \cdot T = B(T^*)$, where $A(T^*)$ is the heat coefficient matrix for the temperature vector (T^*) from the previous iteration (ref. figure 3.7). T is the temperature vector, and $B(T^*)$ is the heat transfer boundary vector, which is depending on the inlet liquid flow, the air temperature T_∞ and wind velocity set as boundary conditions.

$$\begin{array}{c}
 \mathbf{A}(T^*) \\
 \left[\begin{array}{cccccc}
 -C_{L1} - \frac{1}{R_{11}} & \frac{1}{R_{11}} & 0 & 0 & 0 & 0 \\
 \frac{1}{R_{11}} & -C_{L2} - \frac{1}{R_{11}} - \frac{1}{R_{12}} & 0 & C_{L4} & 0 & 0 \\
 C_{L1} & 0 & -C_{L3} - \frac{1}{R_{21}} & \frac{1}{R_{21}} & 0 & 0 \\
 0 & 0 & \frac{1}{R_{21}} & -C_{L4} - \frac{1}{R_{21}} - \frac{1}{R_{22}} & 0 & C_{L6} \\
 0 & 0 & C_{L3} & 0 & -C_{L5} - \frac{1}{R_{31}} & \frac{1}{R_{31}} \\
 0 & 0 & 0 & 0 & C_{L5} + \frac{1}{R_{31}} & -C_{L6} - \frac{1}{R_{31}} - \frac{1}{R_{32}}
 \end{array} \right]
 \end{array}
 \begin{array}{c}
 \mathbf{T} \\
 \left[\begin{array}{c}
 T_1 \\
 T_2 \\
 T_3 \\
 T_4 \\
 T_5 \\
 T_6
 \end{array} \right]
 \end{array}
 =
 \begin{array}{c}
 \mathbf{B}(T^*) \\
 \left[\begin{array}{c}
 -C_{Lin} * T_{in} \\
 -\frac{1}{R_{12}} * T_\infty \\
 0 \\
 -\frac{1}{R_{22}} * T_\infty \\
 0 \\
 -\frac{1}{R_{32}} * T_\infty
 \end{array} \right]
 \end{array}$$

Figure 3.7: System equations for the lowest number of model elements ($m=3$).

The surface temperature T_s is calculated from the temperature in the outer pipe (ref equation 3.1). The non-linear set of equation is solved by finite difference method with iteration, MATLAB was used to program the equations and solve the problems. The program was made to plot the temperature distribution along the pipe-length L for a given inlet

temperature T_{in} , volume flow V_{flow} and geometry (relative area $\frac{A_1}{A_2}$). An example of a temperature distribution is shown in figure 3.8.

$$T_s = \frac{(h_{w2} \cdot T_o) + (h_{air} \cdot T_\infty)}{h_{air} + h_{w2}} \quad (3.1)$$

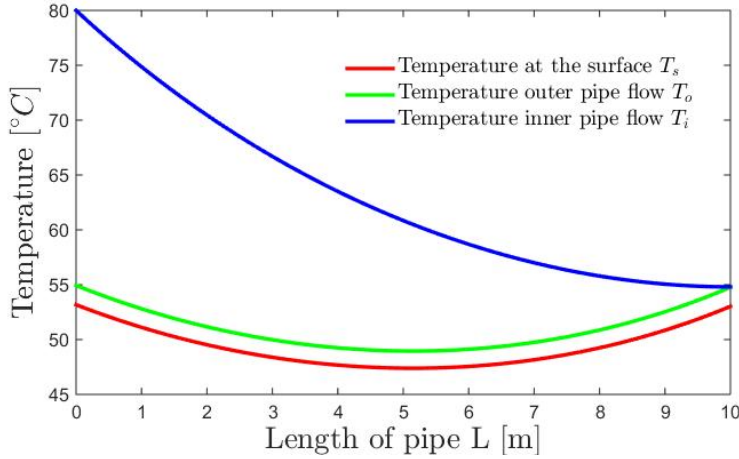


Figure 3.8: Simulated temperature distribution of the double-pipe (Ø50-Ø38), ($L = 10m$, $U = 0m/s$, $T_{in} = 80^\circ C$, $T_\infty = -10^\circ C$ and $V_{flow} = 0.025m^3/h$).

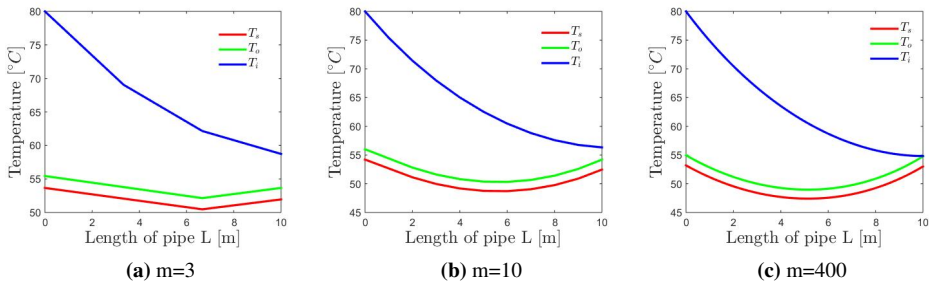


Figure 3.9: Simulated temperature distribution for various number of elements m .

The number of elements on the inner flow is denoted m set in the MATLAB program, which implies that the total number of elements $N = 2m$, this due to the double flow. The inner and outer flow temperature for the pipe turn (where the green and the blue graph are connecting) ΔT_{end} should converge towards zero with sufficient number of elements. The effect of element numbers is shown in figure 3.9 and 3.10. ΔT_s is the maximum temperature difference of the pipe surface. As seen in figure 3.10, sufficient number of elements for convergence is chosen to be $m = 400$, giving $\Delta T_{end} < 0.1^\circ C$.

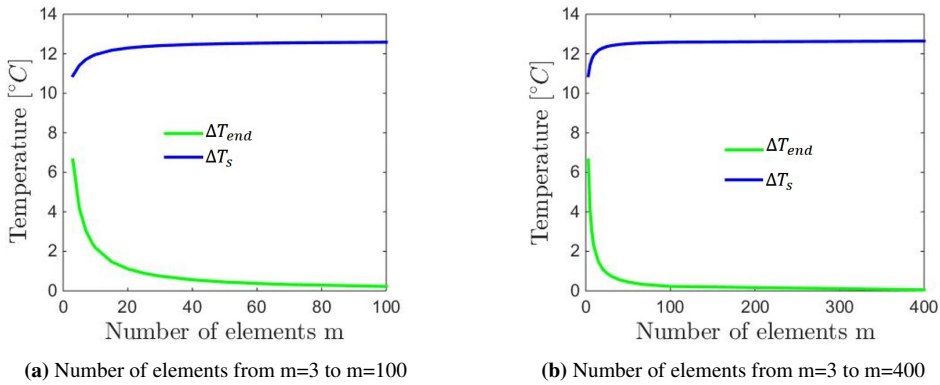


Figure 3.10: Converging plot showing that $m=400$ is a sufficient number of elements. ΔT_{end} is converging towards 0 when $m=400$.

3.3 2D Axisymmetric heat transfer model (CFD)

The 1D axisymmetrical model use the bulk temperature of the water in the calculations, and lumped capacitance method neglecting the pipe wall thickness. The intention is to advance the 1D axisymmetrical model to an 2D axisymmetric CFD model. The factors to be included are; radial temperature distribution, non uniform flow inside the pipes, pipe wall, and a layers of ice. The ice model includes phase change properties. The simulation program COMSOL Multiphysics is used to simulate these more complex CFD models.

3.3.1 Steady state model (Anti-icing)

For typical anti-icing cases, steady state conditions are assumed keeping the outer surface above required temperatures $+3^{\circ}C$. Hence, a steady state simulations are chosen for the anti-icing cases. These simulations will later be compared with the 1D axisymmetrical model. This is to verify the significance of the simplifications and assumptions made for the 1D model. The COMSOL "built-in" material properties for water and aluminum are used, where as glycol water mixture is included in the MATLAB model. For steady state simulation, no significant differences are seen in the simulations between the two models. Hence, pure water properties are used in CFD simulations. The modelling procedure in COMSOL Multyphysics is listed below:

1. Choose 2D axisymmetric model.
2. Choose Non-Isothermal Flow.
3. Creat a component:
 - (a) Definitions; choose explicit selections to group and name the boundaries and parts for easier modeling.

- (b) Geometry; draw the geometry, inner pipe flow, inner pipe, outer pipe flow outer pipe and water turn for the given geometries.
 - (c) Materials; connect the built in material aluminum to the pipe walls and the heat transfer boundaries, also connect the built in material water to the water flow and the water boundaries.
 - (d) Set flow laminar or turbulent based on the Reynolds number; implement and set the boundary conditions for the model. Set the volume flow rate for the inlet, set the pressure conditions to 0Pa at the outlet and choose No slip conditions for the walls.
 - (e) Heat transfer in fluids; set the inlet temperature, choose the outflow boundary, set the heat flux for the outer pipe to air boundary and choose thin layer for the heat transfer between the water flow and the pipe walls. Here, use thermally thin approximation and set the layer thickness (3.5mm is used for these simulations).
 - (f) Mesh the model; physics-controlled mesh; *Normal* mesh give sufficient result for this geometry.
4. Study; steady state.
 5. Compute the results
 6. Results; line graphs are used to plot the temperature distribution along the length and through the layers. Numerous 2D Surface plots are made to visualize the temperature distribution, and velocity profiles.
 7. Export data is used to export data points and later plotted in Excel and MATLAB. The exported data points were plotted together with the analytically results to compare the calculations.

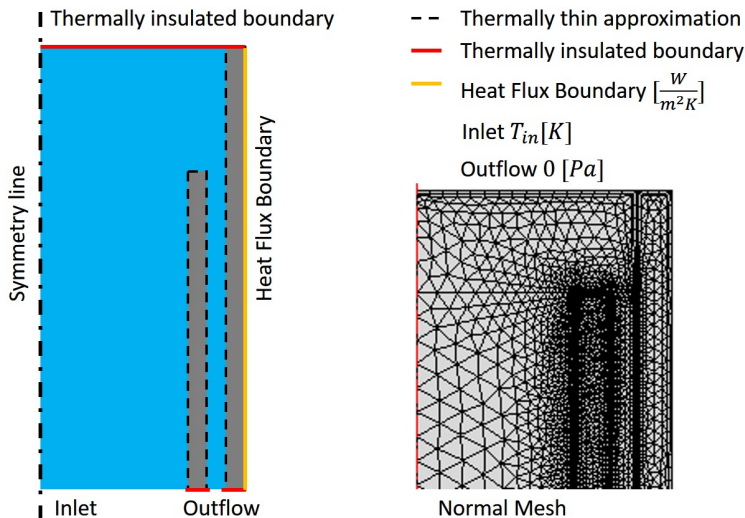


Figure 3.11: Schematic overview of the boundary conditions and the mesh (pipe-turn) for the anti-icing.

Figure 3.11 show an overview of the boundary conditions applied to the geometry, also it shows how the pipe turn is modelled to get the pipe turn effect on the flow. The image is not proportional to the modeled geometry, but it shows where the different boundary conditions are implemented. Heat flux (heat transfer in fluids) are used to simulate the boundary conditions for different wind velocities (0-20m/s). It may also be used to include the effect of water spray by increasing the heat flux.

3.3.2 Transient model (De-icing)

A de-icing simulation is time dependent due to the phase transition of melting ice. Hence, a transient model is used to simulate the de-icing process. The simulation starts with a certain ice thickness and it is assumed that the melted ice do not drain, and that the remaining ice is symmetrical around the center of the pipe. The modelling procedure is similar to the steady state model (ref. sub-section 3.3.1). The transient model is extended from the steady state model. The differences between the steady state model and the transient model are listed below:

1. Global Definitions; define the material parameters which later will be used in the phase change materials (Transition temperature, transition interval, latent heat of fusion, initial temperature of the air, temperature of the water inlet, density of ice, density of water and ratio of densities). Make a step function for the temperature in the phase change interface.
2. Component:
 - (a) Geometry; add the ice thickness (10mm).
 - (b) Materials; create two blank materials and name them phase change ice and phase change air. Implement the material parameters and the step function which were defined in Global Definitions.
 - (c) Flow; same as the steady state model.
 - (d) Heat transfer in fluids; same as the steady state model, additionally set the initial temperature (same as the air temperature $-10^{\circ}C$), and add a phase change material (set the phase change temperature, transition interval and latent heat of fusion, choose *ice phase change* as material phase 1 and *water phase change* as material phase 2).
 - (e) Mesh the model; Physics-controlled mesh; *Extra course* is sufficient for the double pipe geometry, but for the phase change material a finer mesh is needed, and a pre-defined mesh *finer* is used for the ice.
3. Study; Time Dependent. Set the time unit and time range for each time plot for example range(0,15,60) which implies a calculation for times between 0sec. to 60sec. with plotting for each 15sec. Multiple range can be set for the same study; range(0,15,60) range(120,60,1200) range(1400,200,3600) are used for this model.
4. Compute the results.
5. Results; line graphs are used to plot the temperature distribution along the length and through the layers. Numerous 2D Surface plots are made to visualize the temperature distribution, and velocity profiles. Here, more than one time plot can be plotted in the same graph.

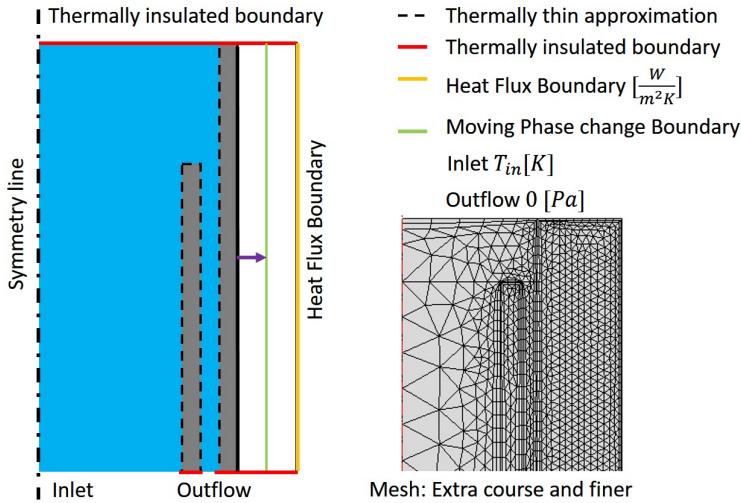


Figure 3.12: Schematic overview of the boundary conditions and the mesh (pipe-turn) for the de-icing model.

Figure 3.12 show how the boundary conditions are applied in the transient model and how the model is meshed around the pipe turn. The ice has a finer mesh due to the phase change properties. The mesh can effect the accuracy of the result and it will also effect the calculation time. Hence, a coarse mesh is selected to reduce the calculation time without significantly affecting the accuracy of the results.

3.4 Simulation results

The 1D axisymmetrical model was used to conduct a parametric study, to get an understanding of the heat transfer system and to support design decisions for the experiments. The 2D axisymmetrical model were used to verify the 1D model, and further improve the model for more complex CFD problems such as the pipe turn and phase change modelling of the melting process. The simulation results are divided into anti-icing simulations and de-icing simulations presented in the following sections.

3.4.1 Anti-icing simulations

The purpose of the anti-icing simulations are to study surface temperature profile under steady state conditions. First of all analyze the ability to keep temperature above minimum requirements (ref. DNV GL rules [6]). Further the objectives are to minimize the heat required to obtain an even surface temperature. The main parameters can be divided into design parameters such as relative area $\frac{A_1}{A_2}$ and pipe length L , and operational parameters such as fluid flow V_{flow} , inlet temperature T_{in} , wind velocity U_{wind} and air temperature T_{∞} .

Comparing 1D-axisymmetric model with the 2D-axisymmetric CFD model.

Figure 3.13 show results from the two different simulation models. In order to compare with later experiments, they are both modelled with the same pipe length $L = 2.5m$ and geometry, flow rate $V_{flow} = 0.01m^3/h$, inlet temperature $T_{in} = 20^\circ C$, wind velocity $U_{air} = 0m/s$ and air temperature $T_\infty = -10^\circ C$ as for the experiments (test 1 ref. table 4.4). The pipe dimensions are the same as in the later experiments with $\text{\O}50\text{-}\text{\O}32$ and $\text{\O}50\text{-}\text{\O}38$ double pipe (ref. experimental setup table 4.1).

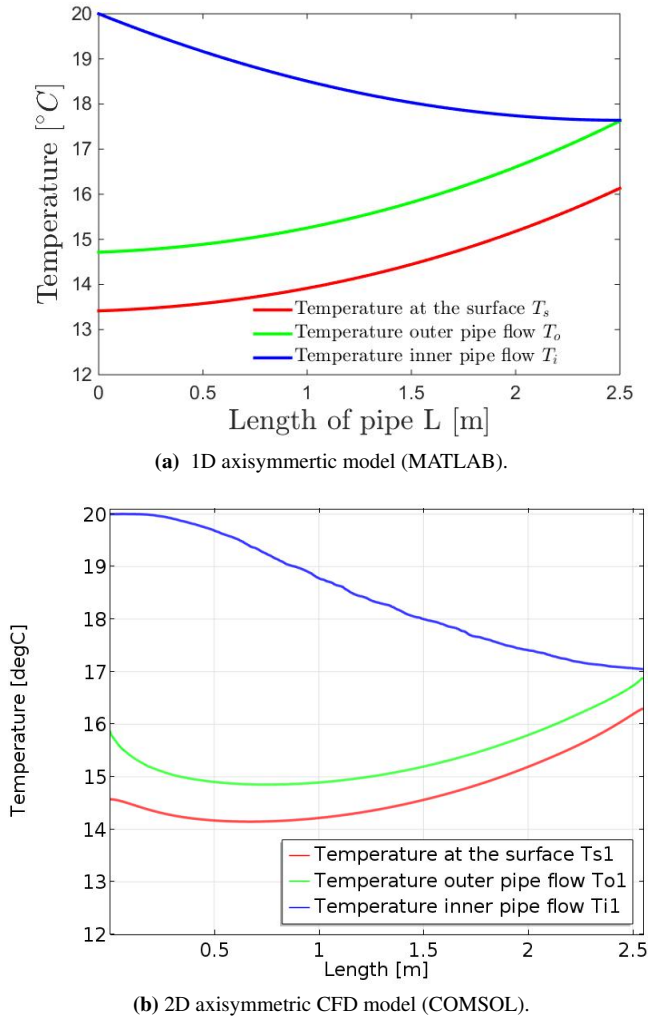


Figure 3.13: Theoretical result comparing 1D and 2D steady state models for the $\text{\O}50\text{-}\text{\O}32$ double pipe used in the experiments in chapter 4.

The result in figure 3.13 and 3.14 shows good correlations between the two different models. The results also show that the simplified 1D-axisymmetric model is a good representation for the anti-icing case.

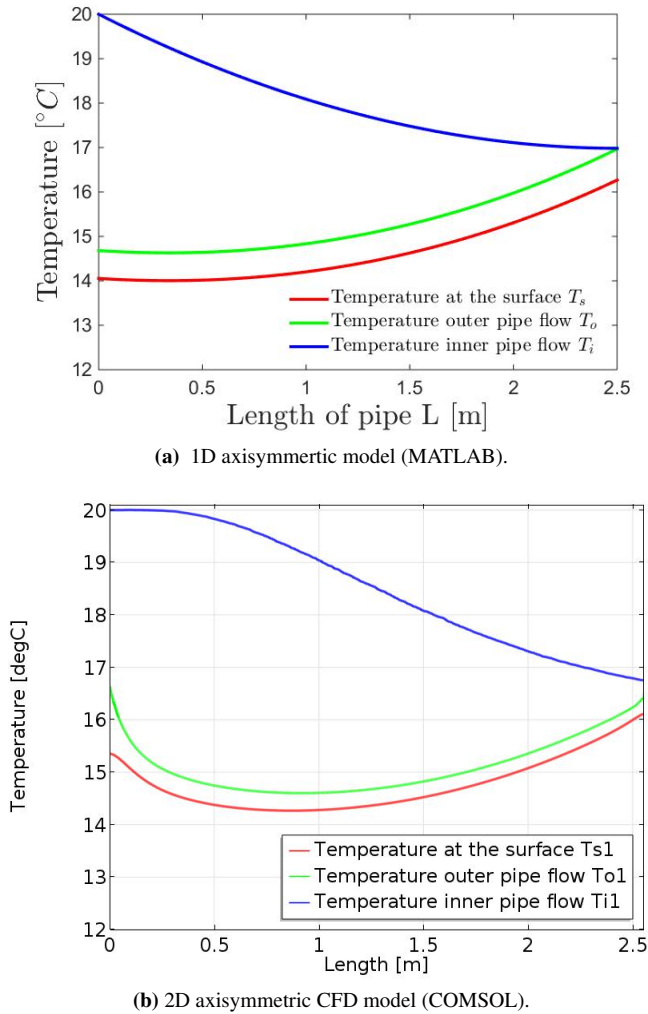


Figure 3.14: Theoretical result comparing 1D and 2D steady state models for the $\text{\O}50\text{-}\text{\O}38$ double pipe used in the experiments in chapter 4.

The 1D model programmed in MATLAB is only modelled for a double pipe simulation. However, in the experiments it was decided later to also test a single pipe as a reference to the double pipes. Therefore, a model of the single pipe was made in COMSOL. The single pipe simulations are shown in figure 3.15. As expected, the single pipe has a greater surface temperature variation compared to the double pipes (ref. figure 3.14 and 3.13).

Hence, a double pipe is clearly preferable to maintain an even surface temperature along the pipe length.

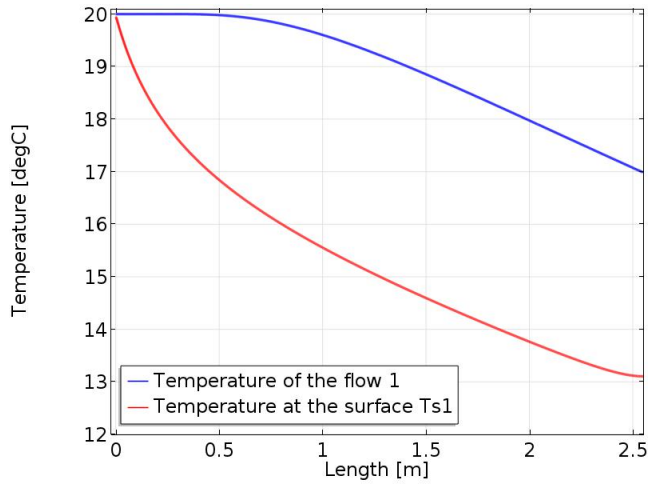
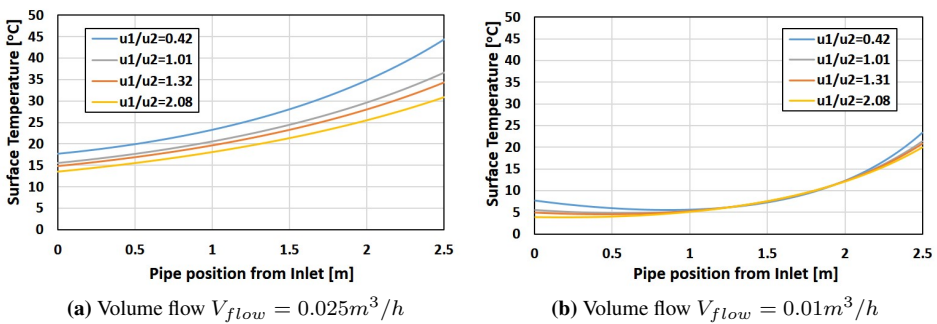


Figure 3.15: Simulation result for the $\text{\O}50$ single pipe (test 1 ref. table 4.4).

Design and operational parameter study

To prepare the experimental setup (ref. chapter 4), a parameter study was conducted, using the simplified 1D model. The objective of this study was to select geometry and test conditions for the experiments. Figure 3.16 show the surface temperature T_s distribution along the pipe for four different double-pipes designs (ref. figure 3.3). Each plot represents a different flow rate $V_{flow} = [0.025, 0.01] \text{ m}^3/h$.



(a) Volume flow $V_{flow} = 0.025 \text{ m}^3/h$

(b) Volume flow $V_{flow} = 0.01 \text{ m}^3/h$

Figure 3.16: Parameter study comparing geometry and flow rates for double pipes with an outer pipe diameter $D = 50 \text{ mm}$.

During the simulations in figure 3.16, the following parameters are kept constant; pipe-length $L = 2.5 \text{ m}$, the air temperature $T_\infty = -10^\circ \text{ C}$, wind velocity $U = 20 \text{ m/s}$ and inlet

temperature $T_{in} = 80^{\circ}C$. To test the effect of pipe length a simulation with $L = 10m$ was also conducted and presented in figure 3.17. As expected, the required flow rate is proportional to the pipe length.

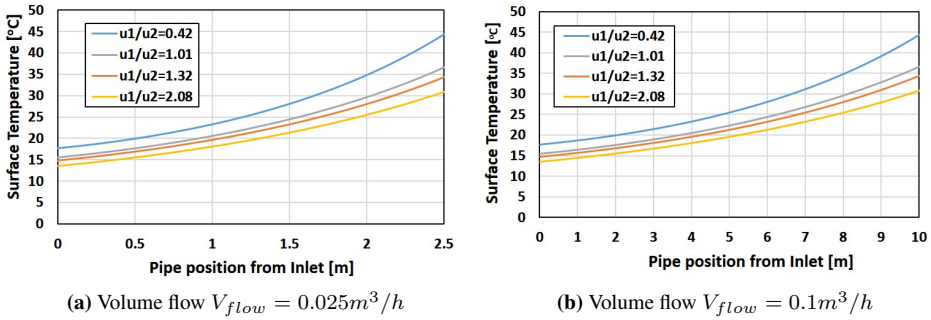


Figure 3.17: Parameter study comparing pipe length L and flow rates for double pipes with an outer pipe diameter $D = 50mm$.

The theoretical simulations show that the main factors affecting the surface temperature are the water flow rate, the pipe length, the air temperature and the wind velocity. The geometry factor $\frac{A_1}{A_2}$ has a smaller influence on the surface temperature distribution than expected. Hence, the flow needs to be controlled relative to the pipe length and the environmental conditions, to get the preferred surface temperature conditions. Simulation results indicates that a velocity factor $\frac{u_1}{u_2}$ less than 1 is preferable giving higher average pipe surface temperature under the same conditions.

3.4.2 De-icing simulations

For the de-icing simulation, the 2D-axisymmetrical model (COMSOL) was modified to a transient model with a phase change material for the ice layer. The initial temperature condition was set to $T_0 = -10^\circ\text{C}$, the water flow rate $V_{flow} = 0.02\text{m}^3/\text{h}$, the inlet temperature $T_{in} = 60^\circ\text{C}$, wind velocity $U_{air} = 0[\text{m}/\text{s}]$, air temperature $T_{air} = -10[^\circ\text{C}]$ and initial ice thickness of 10mm . This condition was selected to compare with the de-icing experiments. The simulation time was set to 1 hour (3600 seconds), plotting temperature profiles for time steps in range(0,15,60), range(120,60,1200) and range(1400,200,3600). Figure 3.18 show the temperature distribution of the water flow through the double pipe and the surface temperature after one hour. Due to the minimum pipe surface temperature at $L = 0.8\text{m}$ from the inlet, three temperature distribution plots are chosen to compare the ice melting process. One at the inlet $L = 0\text{m}$, at $L = 0.8\text{m}$ and at $L = 2.55\text{m}$ (pipe turn).

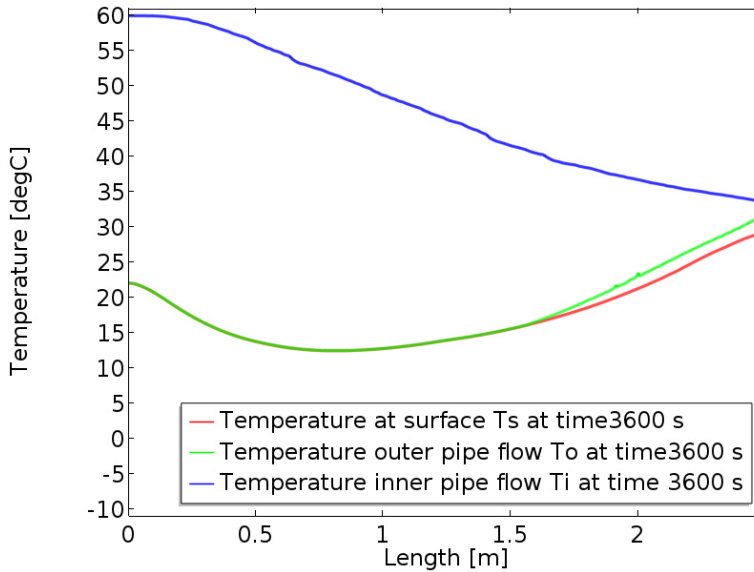
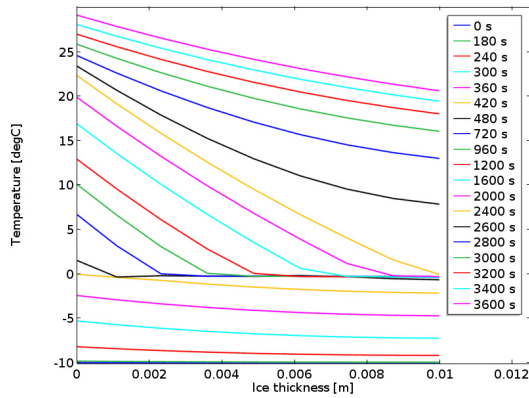
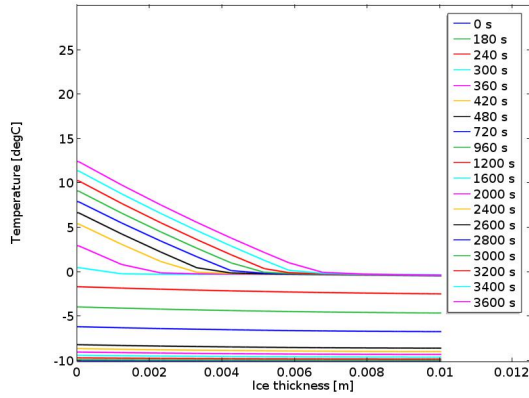


Figure 3.18: Temperature distribution of the de-icing simulation at time 3600s.

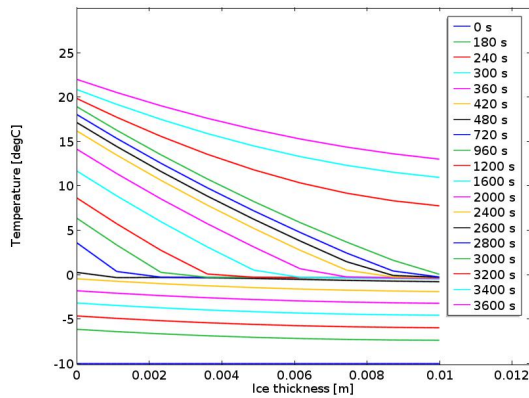
Figure 3.18 show the temperature profile through the ice layer. The ice layer starts to melt on the pipe surface after approximately 7 minutes (ref. figure 3.19a). And melting starts at the pipe end with the highest water temperature. At the lowest temperature $L = 0.8\text{m}$ melting starts after approx. 25 minutes (ref. figure 3.19b). After one hour the simulation indicates that there is still ice left at $\sim L = 0.8$, it remains approx. 3mm thick ice. The whole ice layer is melted after approx. 50 min at the pipe inlet $L = 0\text{m}$, and 40 min. at the pipe end $L = 2.55\text{m}$ (ref. figure 3.19c). After 40 min. this simulation model is not valid, due to water draining.



(a) Distance from pipe inlet $L=2.55\text{m}$



(b) Distance from pipe inlet $L=0.8\text{m}$, (min. surface temp).



(c) Distance from pipe inlet $L=0\text{m}$

Figure 3.19: Temperature profiles for the ice layer model, fresh water ice with initial thickness 10mm. Temperatures higher than 0°C is equal to melted ice (water).

The de-icing model has not reached steady state conditions after 1 hour. Hence, the de-icing time seems to be greater than one hour. On the other hand, the de-icing model is not physically realistic. Water will drain as soon as the ice layer is melted away at one point of the horizontal pipe. Thus, the de-icing time might be less than simulated. Another possibility is that the water drains creating an insulating layer of air between the pipe surface and the ice. Also, the ice is never symmetrical around the pipe in real conditions. Hence, the de-icing model can only be used to simulate the first part of the de-icing process and estimate an approximate de-icing time.

The temperature profile of the pipe at $L = 2.55m$, $L = 0.8m$ and $L = 0m$, at different time steps are plotted in figures 3.20, 3.21 and 3.22. The temperature scale show temperatures from $-10^{\circ}C$ to $60^{\circ}C$. After 300 seconds the pipe flow at the turn reaches a temperature of approximately $10^{\circ}C$. At 1200s at $L = 2.55m$, 50% of the ice thickness has melted. At pipe length $L = 0.8m$ from the inlet, the flow in the inner pipe has reached a bulk temperature of approx. $45^{\circ}C$. After 1200 seconds, the ice temperature is still below $0^{\circ}C$, which also can be seen in figure 3.19b. The phase change boundary has moved 5mm after 3000 seconds, leaving 5mm of ice and 5mm of water between the pipe and the ice.

The model assumes that the water is trapped between the ice and the pipe wall. In reality at some point the water will start to drain, leaving insulating pockets of air between the ice and the pipe surface. Therefore, an attempt to extend the simulation model to include water-draining/air-layer was made. However, material properties of ice/water/air caused numerical problems and therefore this attempt was left for further theoretical studies and experiments. Practical experiment also needs to be conducted to find the actual de-icing time due to irregular ice melting and accretion.

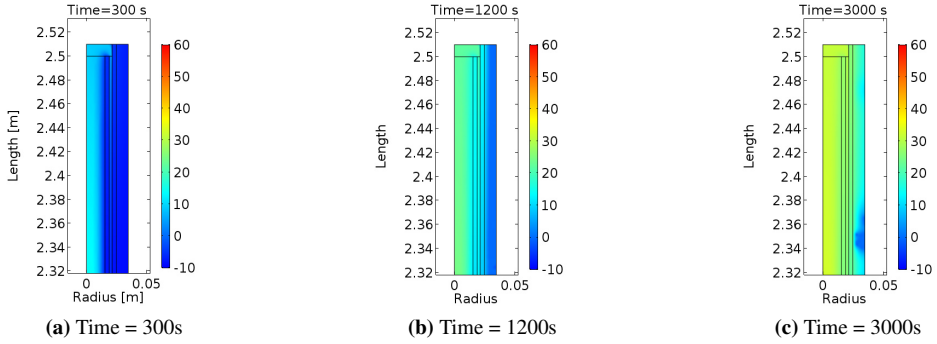


Figure 3.20: 2D temperature plot at pipe length $L=2.5\text{m}$

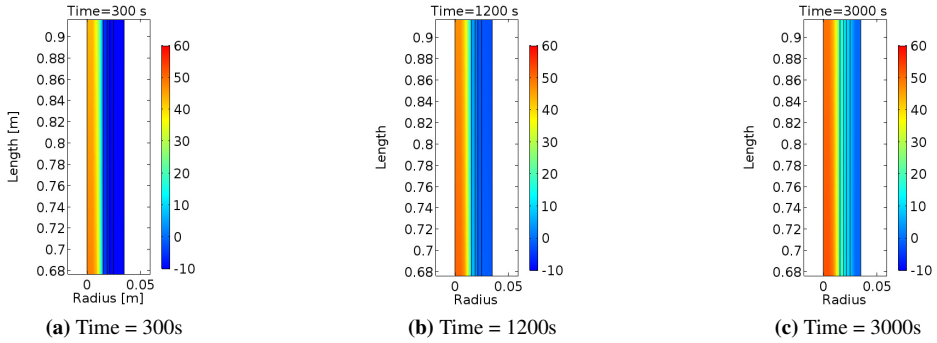


Figure 3.21: 2D temperature plot at pipe length $L=0.8\text{m}$

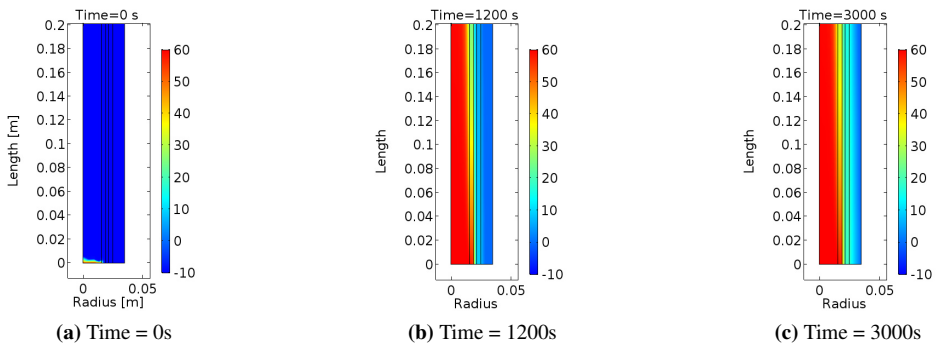


Figure 3.22: 2D temperature plot at pipe length $L=0\text{m}$

Experiments

The purpose of this laboratory experiment is to verify the numerical simulation models (presented in Chapter 3), which are calculated from basic heat and mass transfer theory. The theoretical models are based on simplifications and assumptions for simulation of anti-icing and de-icing processes. Especially, the de-icing model is based on very simple phase transfer models, where the ice melting process needs to be tested. The theoretical parameter study presented in section 3.4 is used to design and prepare the experimental setup and test conditions. In addition to anti-icing, it will be possible to test icing and de-icing. Ice growth is a complex problem which is difficult to simulate correctly together with de-icing. This is because icing is depending on many different factors caused by different weather conditions. Due to practical limitations of the test setup and time limitation for the master's thesis project, a set of test conditions were selected. The first part focused on anti-icing conditions and heat requirements under different temperature and wind conditions. Icing and de-icing is tested only with fresh water ice due to practical limitations. The different case studies are represented in sub-section 4.1.7. Planning, design, building and testing of the de-icing laboratory was a large part of the master thesis project presented in the following section (4.1).

4.1 Laboratory design and experimental setup

To get DNV GL type approval for the Ulmatec Pyro de-icing system, the product must be tested at DNV GL laboratory in Høvik. This kind of external testing is normally very expensive, and therefore some optimization needs to be conducted before final approval testing. The idea behind making a test lab internally at the company, is to be able to do many pre-tests and to be able to test different designs and parameters related to this new patented technology. In addition, it would be advantageous to know that the tests will be approved before sending it to DNV GL's test lab, in order to reduce risk and costs. The test lab used for this experiment (ref. figure 4.1), is designed and planned by the student in collaboration with Ulmatec Pyro. The test lab is designed for this master thesis, but also

designed to comply with the test lab at DNV GL in Høvik. Hence, some of the design decisions and limitations are due to later use of the lab.

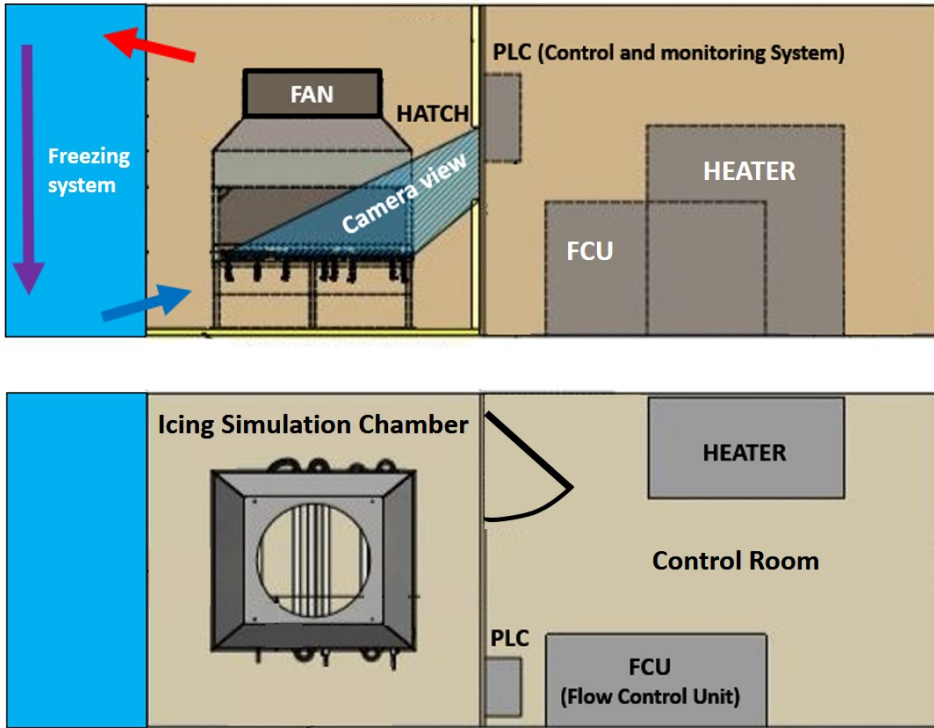


Figure 4.1: The freezer container general arrangement drawing with the essential equipment, pipes and connections between the units are not included in this drawing.

A twenty-foot freezer container was purchased for the purpose of being converted into an experimental laboratory. This container has a temperature range down to $-25^{\circ}C$. The modification process involved dividing of the container into two rooms; the icing simulation chamber and the control room as shown in figure 4.1. The icing simulation chamber is insulated from the control room, and access is given through a door and a hatch for camera access. The control room which is equipped with: an electric heater with a capacity of $0.7[m^3]$ glycol-water and heating power of $50[kW]$, a flow control unit (FCU) regulated by the outlet temperature of the test section (standard system of Ulmatec Pyro), a pump for circulation, and a control panel (PLC) to control and monitor the processes.

4.1.1 Icing simulation chamber

For this master thesis, it would be ideal to test pipes in the full straight length of the container. Practically this presents various challenges in finding a fan capable of producing high enough wind velocities ($20m/s$) uniformly for the whole pipe length. In addition, this

test lab will be used for pre-testing of different de-icing products which later that has to fit into DNV GL's test lab. Hence, the test rig was designed so that the pre-tested products can be shipped to Høvik without being changed too much. The horizontal test section is 1.2x0.85m as also shown in figure 4.5.

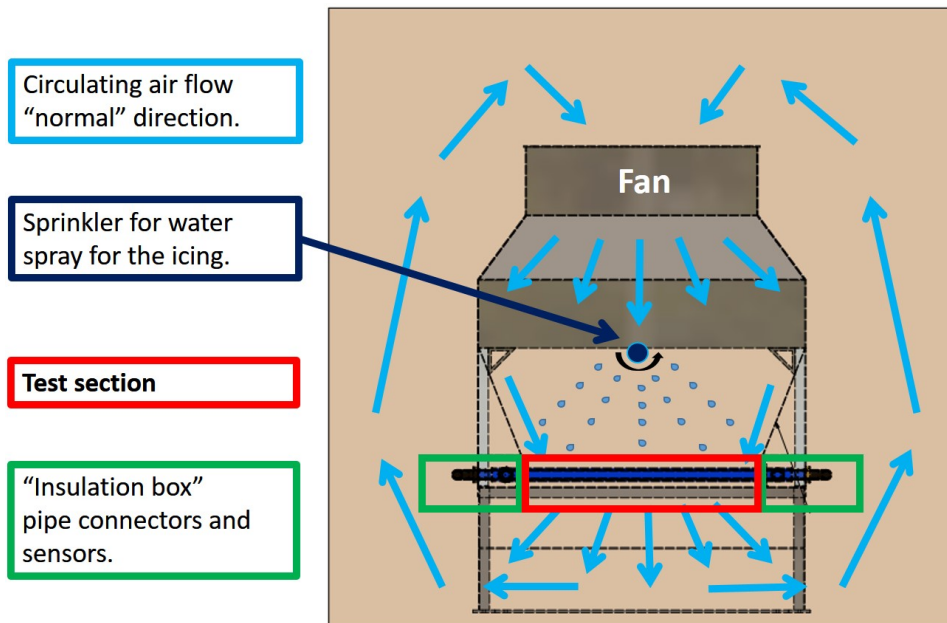


Figure 4.2: Principle drawing showing how the airflow is circulating in the test room.

Figure 4.2 show how the wind is generated by the fan, and how it is circulating inside the icing simulation chamber. Ideally it should be designed as a wind tunnel with a duct long enough to produce a uniform wind velocity for the test section. However, due to space limitation the simulation chamber is designed with an overhead fan with a short duct with plates directing the flow towards the test section with the non insulated part of the test pipes. The airflow will circulate inside the room as shown in figure 4.2. The container freezing system will provide cold air inside the simulation chamber, so that the circulating air temperature maintains constant. For simulating water spray for the icing and de-icing experiments a sprinkler system made of a pipe with many tiny holes installed between the fan and the test section (ref. figure 4.2).

4.1.2 Test section (pipe design)

A theoretical hypothesis based on heat transfer theory is compiled by the student, which implies that in order to achieve a uniform surface temperature along the length of the pipe, most of the heat loss should occur in the inner pipe. In order to achieve this, the fluid velocity in the inner pipe should be slower than the velocity in the annulus. The theoretical

parameter study conducted in the numerical study, indicated that the velocity difference in the inner and outer pipes is an important parameter for the double pipe design. Therefore, this is interesting to test experimentally. Hence, 3 different pipe-dimension were chosen for the experiment. A single pipe (3), a pipe with higher velocity in the annulus (2), and a pipe with higher velocity in the inner pipe (1), ref figure 4.3. The pipe dimensions chosen for the experiments are listed in table 4.1. The purpose of testing the single pipe as a reference to compare the surface temperature difference along the pipe length with the pipes using Ulmatec Pyro's double pipe design.

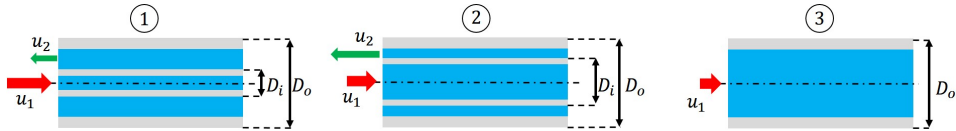


Figure 4.3: Principle drawing of the pipe dimensions used in the experiments (ref. also table 4.1).

Table 4.1: Pipe dimensions for the laboratory experiments.

Pipe dimensions			
Pos number (figure 4.5)	Inner pipe (D_i [mm])	Outer pipe (D_o [mm])	Velocity factor ($\frac{u_1}{u_2}$)
1	32 x 3.5	50 x 3.5	1.32
2	38 x 3.5	50 x 3.5	0.42
3	[-]	50 x 3.5	[-]

This final product will be extruded aluminum profiles. However, ordering special designed profiles in small quantities for testing is expensive and requires long delivery time. Hence, the pipes for these experiments are designed with standard aluminum pipes which are welded. Due to size limitation on the test section, the pipes had to be design in three pipe sections connected with insulated pipe bends as shown in figure 4.4. The purpose of the insulation "box" is to prevent heat losses and heat transfer in this part of the pipe, so all heat loss to the air will occur at the exposed sections. It is also preferable for Ulmatec Pyro to test more than one design at the same time in the lab in Høvik. Hence, to fit 3 designs into one test section the maximum length of each pipe is 3m. Since this is a prototype pipe to be welded from standard aluminum pipes for this project, it was a challenge to design a smart and "standardized" solution, that could be assembled into a "long" pipe. Figure 4.4 shows an early stage sketches of the design principle, which was used for manufacturing. Due to limited access to standard pipe dimensions, the wanted velocity factors ($\frac{u_1}{u_2} < 1$) was difficult to obtain. Double pipe number 2 (ref table 4.1) will have a very small clearance between the two pipes ($2.5[mm]$), which can lead to greater pressure drop and unpredictable flow through the pipe.

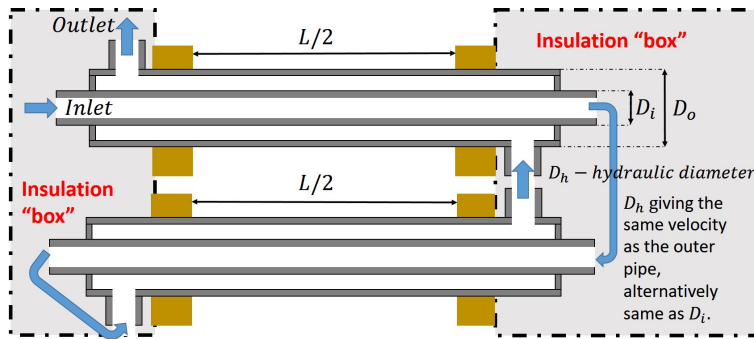


Figure 4.4: Principle drawing of the double pipe arrangement in the test section.

As mentioned in section 4.1, the flow control unit (FCU) is regulated by the return flow temperature using a flow control valve. For these master thesis experiments, 3 extra flow sensors and 3 additional temperature sensors were added to the pipe inlets. In addition, a small manual flow control valve was installed for more accurate flow control. The pipes from the FCU was insulated to prevent heat loss between the FCU and the test section. To be ensure correct inlet temperature for all three test pipes, three additional temperature sensors were installed at the pipe inlets. Manual valves on the FCU are used to control the flow and keep it constant throughout the experiment for all three test pipes which will be tested at the same time. Hence, the purpose of the flow sensor at the inlet of all the three pipes is to adjust and control the flow in each of the three pipes separately. Figure 4.5 shows the final test section design with 3 different pipe designs consisting of three pipe sections each. The effective length of each test pipe is $L = 2.55m$ ($3 \times 0.85m$). The location of the sensors is also shown in figure 4.5.

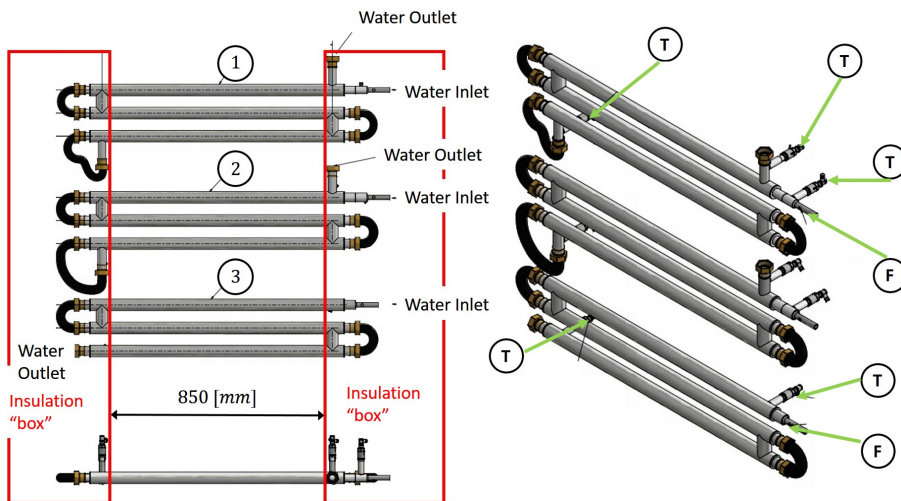


Figure 4.5: Test section consisting of three test pipes (1-3), temperature- (T) and flow sensors (F).

4.1.3 Instrumentation and data logging

Figure 4.6 shows the schematics of the de-icing test systems with sensor locations and identifications. Sensor identification are specified in table 4.2.

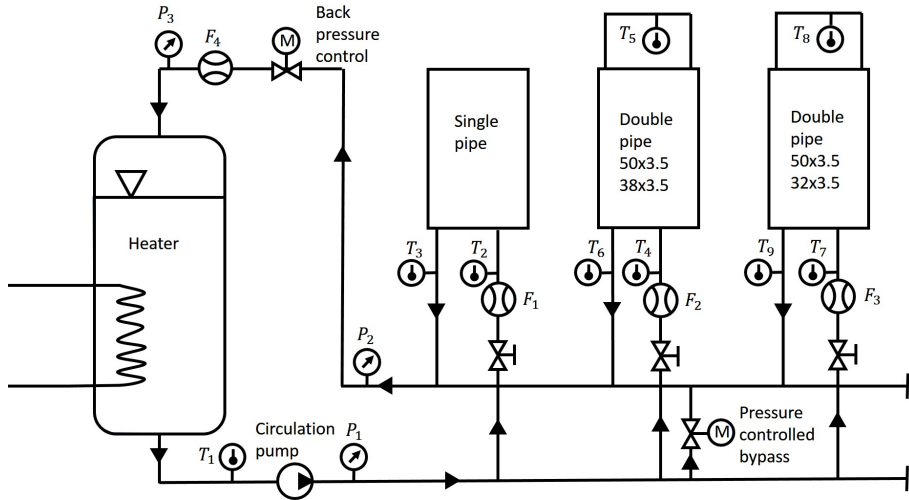


Figure 4.6: Schematic drawing of the de-icing test system.

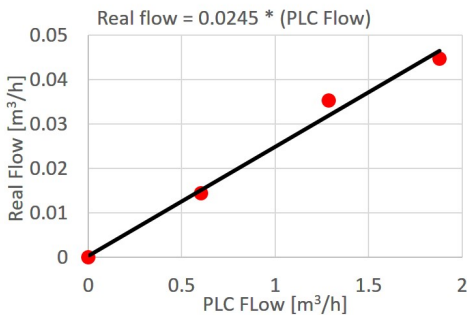
Table 4.2: Overview of sensors and control valves.

Description	Symbol	Description
Pressure [bar]		P_1 Pressure after the pump
		P_2 Pressure after the FCU
		P_3 Pressure in the heater
Flow [m^3/h]		F_1 Inlet flow for the single pipe
		F_2 Inlet flow for the double pipe 50x38
		F_3 Inlet flow for the double pipe 50x32
		F_4 Total flow including the bypass
Temperature [$^{\circ}C$]		T_1 Heater temperature
		T_2 Inlet temperature for the single pipe
		T_3 Outlet temperature for the single pipe
		T_4 Inlet temperature for the double pipe 50x38
		T_5 Turn temperature for the double pipe 50x38
		T_6 Outlet temperature for the double pipe 50x38
		T_7 Inlet temperature for the double pipe 50x32
		T_8 Turn temperature the double pipe 50x32
		T_9 Outlet temperature for the double pipe 50x32
Control valves		Manual and (M)-Automatic pressure controlled

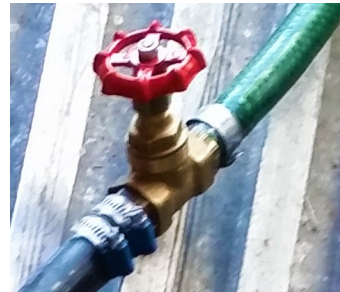
Temperature sensor location relative to simulation temperature plots are shown in figure 4.8a. The surface temperatures are measured with an infrared camera (ref. figure 4.8b), which is compared with the red line in the simulation temperature plot shown in figure 4.8a. The IR-image is taken through the hatch from the control room (ref. figure 4.1).

4.1.4 Flow sensor calibration

A new type of flow sensor IFM SA4100, which Ulmatec Pyro has installed in their systems previous to these experiments. Calibrating this sensor was a challenging task. From energy balance calculations, it was clear that the sensor gave a flow that was too high. Therefore, a separate calibration test was performed on one of the sensors. The pipes were disconnected from the flow control unit (FCU), the manual valve was connected to a water supply hose (ref. figure 4.9b) and the outlet flow were manually measured using a container to collect the water. The pipe systems were drained for glycol-water mixture, and pure water of 20°C were used to calculate a calibration factor to get the real flow. Three tests were conducted to determine the calibration factor. The manual valves were used to control the flow. When the flow was stabilized, the hose was passed over the measuring container and held there for exactly 6 minutes. Then the container was weighed and the real flow was calculated. This was repeated for three different flows. The density of water at 20°C ($998.2\text{kg}/\text{m}^3$), and the average flow from the PLC logging was used for calculation of the calibration factor. Figure 4.9a show the calibration results, and the calculated calibration factor is 0.0245 which is used for following tests. Due to time limitations and the fact that the flow sensors are identical for all three pipe circuits, the same calibration factor was further used for all flow sensors.



(a) Calibration-factor plot.



(b) Manual flow control valve.

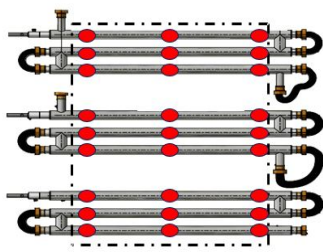
Figure 4.9: Flow sensor calibration. The calculated calibration factor is 0.0245.

4.1.5 Air flow measurements

The air fan rpm is controlled by a frequency converter (0-50Hz), which makes it possible to control the air flow velocity. Hence, a calibration test have been conducted to map the wind velocities at certain frequencies. KIMO VT115 Thermo-anemometer with hotwire is used to measure the wind velocities [16]. It is also desirable to test how even the wind velocity

variation over the test section. The results of the test is presented in table 4.3, where the red dots (ref. figure in table 4.3) present the measuring points during the velocity measurements. Relative linearity between frequency and wind velocity were observed. Hence, only two frequencies are represented in table 4.3. Since wind velocity varies over the test section, an average wind velocity is calculated and presented in the right column. This average velocity is used when comparing with numerical simulations.

Table 4.3: Wind velocity calibration measurements.

Fan frequency [Hz]	Pipe dimensions [mm]	Air velocity [m/s]			
		Left	Center	Right	Average
[-]	50x32				
	50x38				
	Single Pipe				
25	50x32	2.5	2.5	1.5	2.6
		3	2.5	1	
		3	5	2	
	50x38	3	2	3	2.6
		2	1	4	
		2	1	5	
	Single Pipe	3	4	8	5.1
		3	4	8	
		3	4.5	8.5	
50	50x32	5	3.5	3	5.2
		6	6	2	
		7.5	10	4	
	50x38	6	4.5	7	5.8
		4	2	9	
		4.5	3	12	
	Single Pipe	6	8.5	15	10.4
		6	10	15	
		6	11	16	

Wind velocities for frequencies in between these measured values can be estimates using linear interpolation. While completing the calibration test, it was worth noting how difficult it was to measure the wind velocity because of turbulence, and an approximated mean value was logged. Due to access problems in the test section, it was difficult to get the

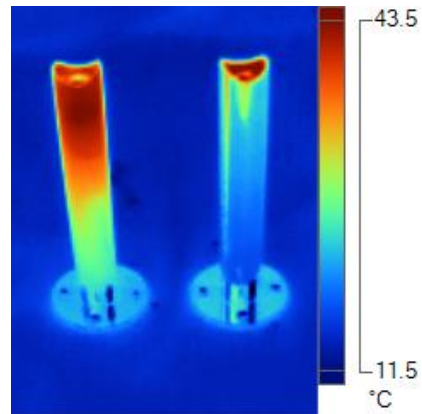
wind velocity from all the angles. Hence, the velocities could be greater than the ones measured. With the given geometry and fan arrangement it is very hard to achieve a uniform steady air flow over all nine pipes. One possible future arrangement could be to test one pipe design (3 pipes) separately. However, due to limited time all three pipe designs are tested simultaneously in this thesis project. A more steady flow in the test section could also be achieved with longer distance from the fan, and with multiple smaller fans. To compare with numerical simulations, the average wind velocity is used as shown in the right column in table 4.3. As seen from the average values, the single pipe is exposed to higher average wind velocity (approximately double). This is taken into account when comparing with numerical simulations.

4.1.6 Infrared camera for pipe surface temperature measurements

To measure the surface temperature of the pipes during the experiment, an infrared (IR) camera FLUKE Thermal Imager Ti110 is used [8]. During the calibration testing of the camera, it was detected that the camera had problems measuring the temperature on the aluminum pipes, due to low emissivity of shiny surfaces. Emissivity is the efficiency of emitting energy as thermal radiation. Shiny aluminum has an approximate emissivity of 0.10 and the camera specifications strongly recommend measuring on surfaces with emissivity higher than 0.6. This issue was solved by applying a thin layer of black matte lacquer on the pipe surfaces to obtain a higher emissivity value. According to table of emissivity (ref. [20]) matte black lacquer has a value of 0.96-0.98. A emissivity value for a thin layer of matte black lacquer on aluminum pipes can be found by a simple temperature test. Measuring the temperature of the material and compare it to the value given by the IR-camera for various emissivity values. Hence, value of 0.96 is used for these experiments.



(a) The two test objects in visible light.



(b) Infrared picture of the test objects.

Figure 4.10: Surface emissivity test for IR-camera. The object to the left is sprayed with matte black lacquer, and the one to the right has a shiny metal surface.

Figure 4.10 show how the accuracy of the IR-camera is strongly dependent on the emissivity of the surface. The two test objects (ref. figure 4.10a) are identical made of a shiny metal and tested under the same conditions. The only difference is that one of the objects have a thin layer of matte black lacquer. Both test objects are placed in a bowl of hot water to heat up the tip of the pipe. The hot tip of the test object which have a matte black lacquer can be seen in figure 4.10b. Hence, low accuracy for low emissivity values.

4.1.7 Test procedure/plan

During the pre-tests, it was discovered that the freezing system failed to maintain stable low air temperatures when the fan was running. Several tests were conducted modifying the test chamber and controlling the air flow. However, it became quite clear that the freezing system did not have sufficient capacity to run the extreme conditions. According to the freezing system specification, the freezing capacity was 3.5kW. Some simple energy balance estimates revealed that heat from the pipes exceeded the capacity of the freezing system. Thus, the total heat transfer of the pipes were greater than the capacity of the freezer container, which could explain the difficulty of maintaining stable air temperature. Hence, some changes to the original test plan was made to adapt to the limitations of the freezing container. For wind tests, the air temperature setting was selected to $-10^{\circ}C$. The control system (PLC) and cameras were synchronized so that all the log data can be compared at the correct time.

Three different test cases were planned; anti-icing, icing and de-icing. And the test procedures are described in the following subsections.

Case 1; Anti-icing - Heat transfer simulations

1. Start the freezing container and set the air temperature. Start the circulation pump and the logging function on the PLC.
2. Adjust the water temperature and flow to maintain a stable flow for all three pipe designs.
3. Wait for the air temperature to stabilize at the set value and the water flow temperatures stabilize. Log surface temperatures using the IR-camera through the hatch (0Hz).
4. Set a new air temperature as low as possible (approximate $-20^{\circ}C$). Wait for the air temperature stabilizes to the new air temperature T_{air} .
5. Start the fan at the chosen air velocity/frequency for the current test (25Hz or 50Hz).
6. Wait until the air temperature reaches $-10^{\circ}C$, log the surface temperatures with the IR-camera through the hatch. Log the time and date for each IR-camera picture to later compare with log data from the PLC.
7. Turn off the fan, and wait until the container reaches the set air temperature. Proceed with point 5 for the next air velocity setting (25Hz or 50Hz).

This should be repeated for all the tests listed in table 4.4 below.

Table 4.4: Overview of the planned test for Case 1; Anti-icing.

Test number	Water temp [°C]	Fan frequency [Hz]	Water flow [m ³ /h]	Air temp [°C]
1	20	0	0.01	-10
2	20	25	0.01	-10
3	20	50	0.01	-10
4	40	0	0.01	-10
5	40	25	0.01	-10
6	40	50	0.01	-10
7	20	0	0.02	-10
8	20	25	0.02	-10
9	20	50	0.02	-10
10	40	0	0.02	-10
11	40	25	0.02	-10
12	40	50	0.02	-10

Case 2; Icing simulations

The icing and the de-icing experiment are connected. Hence, the temperature of the heater and the pipe flow for the de-icing experiment should be set before turning off the pump stopping the circulation in the pipes.

1. Set the container temperature to -10 °C.
2. Set the heater temperature to 40 °C.
3. Adjust the pipe flow to approximate 0.02 m³/h.
4. Stop the pump (no flow in the pipes during icing).
5. Wait until the steady state temperature inside the test chamber has reached -10 °C.
6. Start applying the water spray with a period of approx. 15 sec. and a duration of approx. 4 sec. [13].

Originally the plan was to build a water spraying nozzle to simulate periodic icing (ref. figure 4.2). Due to time limitations the spray was manually applied with a spray gun (ref. figure 4.11). The water spray was applied every 15 seconds, and pictures of the pipes were taken with a GoPro camera in between each spray application with a 15 second time lap.

Case 3; De-icing

The water temperature and the flow were already set during the icing experiment.

1. Make sure the time and date settings of the GoPro camera is the same as the PLC.
2. Start the GoPro camera with time-laps, picture every 10s. (ref. figure 4.12 at t=0).
3. Start the pump, note the starting time.
4. Take picture with the IR-camera every 15min.
5. Take closeup pictures with a camera.
6. Log the ending time.



Figure 4.11: Icing - Manually application of the water spray.



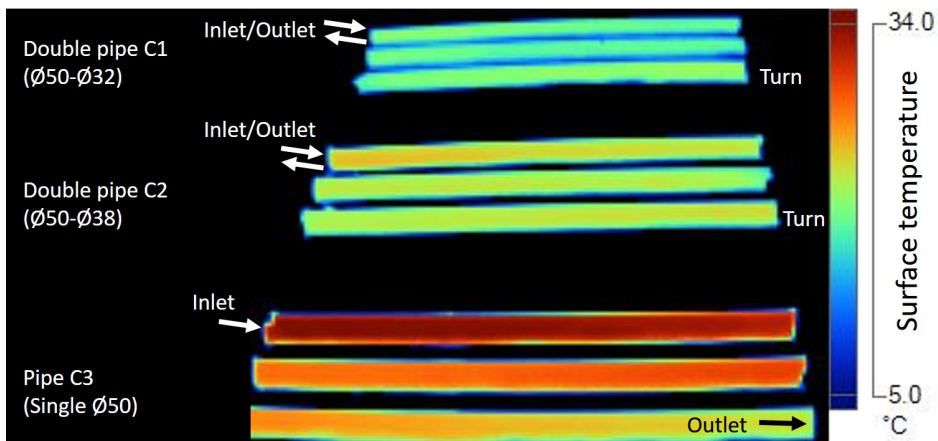
Figure 4.12: Starting de-icing process.

4.2 Experimental results

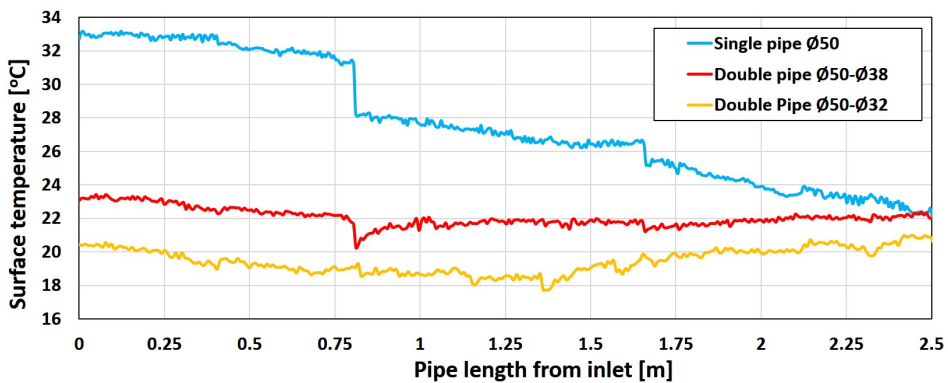
The experimental results are divided into; Anti-Icing, Icing and De-Icing. They are presented briefly in this section and discussed further in chapter 5 where numerical simulations and experimental results are compared.

4.2.1 Case 1; Anti-icing

During anti-icing tests, surface temperature was measured using the infrared camera (IR-camera). Figure 4.13a show the pipe surface temperatures recorded by the IR-camera. Based on the IR-images, surface temperatures were extracted from the images using FLUKE's software "SmartView" [8]. The results clearly show that the double pipes have a more uniform surface temperature than the single pipe (ref. figure 4.13).



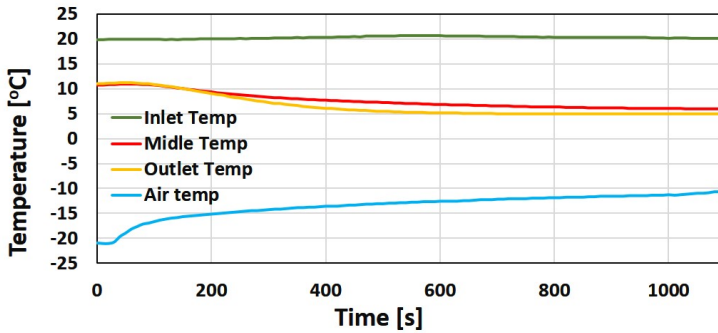
(a) IR-camera image



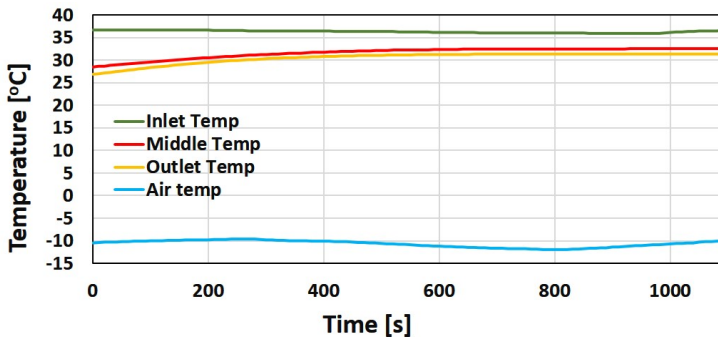
(b) Temperature plots from the IR-camera.

Figure 4.13: Surface temperature measured with the IR-camera (inlet temperature $T_{in} \approx 35^\circ C$).

Water temperatures and air temperatures were measured and logged by the Ulmatec Pyro's control system (PLC). Figure 4.14 show temperature-time plots during a test sequence. From the plots we can see when the test conditions reaches steady state ($\frac{dT}{dt} \approx 0$). The test procedures are reflected in the graphs. For the cases with wind velocities, an air temperature $T_{air} = -20^\circ C$ is set for the freezing container. The air temperature starts increasing as the fan is started (ref. figure 4.14a). Due to freezing container limitations, the temperatures do not reach steady state conditions. But the temperatures is relatively stable after approx. 15 min. ($\sim 900s$). Hence, the IR-picture is taken at approx. 15 min. ($\sim 900s$). For the tests with wind velocity $0m/s$, the container is set to $T_{air} = -10^\circ C$. Figure 4.14b show some irregular air temperatures over time, this is due to the freezer control system. It also shows steady state conditions after approx. 10min. (600s). Hence, the IR-picture is taken after 10 min. Due to freezing container limitations, only the experiments with no wind ($U = 0m/s$) reaches steady state conditions. Hence, this is taken into considerations when comparing with numerical simulations. All anti-icing tests are presented in table 4.5. The temperature difference in the water flow is calculated as the difference between the inlet and outlet of the "outer- pipe". Hence, $\Delta T_L = T_{in} - T_{out}$ for the single pipe and $\Delta T_L = T_{turn} - T_{out}$ for the double pipes.



(a) Test 2; $T_{in} = 20^\circ C$, $U = 2.6m/s$, $V_{flow} = 0.01$ and $T_{air} = -10^\circ C$.



(b) Test 10; $T_{in} = 40^\circ C$, $U = 0m/s$, $V_{flow} = 0.02$ and $T_{air} = -10^\circ C$.

Figure 4.14: Time dependent temperature plot for the double-pipe $\text{Ø}50\text{-}\text{Ø}38$.

Table 4.5: Test result from the PLC. Case1; test 1-12. $\Delta T_L = T_{in} - T_{out}$ for the single pipe and $\Delta T_L = T_{turn} - T_{out}$ for the double pipes.

Test	Pipe dimensions [mm]	Water flow temperature [°C]			ΔT_L [°C]	Flow [m ³ /h]
		T_{in} [°C]	T_{turn} [°C]	T_{out} [°C]		
1	Ø50 - Ø32	16.9	14.3	11.5	2.8	0.008
	Ø50 - Ø38	17.4	13.7	12.7	1.0	0.0064
	Single Pipe	17.4	[-]	13.5	3.9	0.007
2	Ø50 - Ø32	19.1	9.1	3.8	5.3	0.008
	Ø50 - Ø38	20.1	5.9	4.9	1.0	0.0064
	Single Pipe	20.2	[-]	5.0	15.2	0.007
3	Ø50 - Ø32	17.1	8.6	2.8	5.5	0.008
	Ø50 - Ø38	17.8	6.5	2.6	3.9	0.0064
	Single Pipe	18.3	[-]	2.7	15.6	0.007
4	Ø50 - Ø32	38.3	30.6	27.9	2.7	0.009
	Ø50 - Ø38	40.1	32.5	32.1	0.4	0.008
	Single Pipe	38.6	[-]	33.2	5.4	0.008
5	Ø50 - Ø32	36.1	22.5	17.1	5.4	0.009
	Ø50 - Ø38	39.1	25.5	21.8	3.7	0.008
	Single Pipe	36.9	[-]	16.1	20.8	0.008
6	Ø50 - Ø32	36.4	23.3	20.3	3.0	0.009
	Ø50 - Ø38	39.5	27.2	25.1	2.1	0.008
	Single Pipe	36.6	[-]	19.9	16.7	0.008
7	Ø50 - Ø32	21.1	19.3	17.5	1.8	0.016
	Ø50 - Ø38	21.4	19.1	18.3	0.8	0.020
	Single Pipe	21.2	[-]	17.0	4.2	0.016
8	Ø50 - Ø32	16.7	12.3	8.5	3.6	0.016
	Ø50 - Ø38	17.2	10.9	8.2	2.7	0.020
	Single Pipe	17.3	[-]	5.9	11.4	0.016
9	Ø50 - Ø32	19.7	13.6	8.9	4.7	0.016
	Ø50 - Ø38	20.4	12.2	8.4	3.8	0.020
	Single Pipe	20.3	[-]	6.0	14.3	0.016
10	Ø50 - Ø32	35.6	33.1	29.9	3.2	0.018
	Ø50 - Ø38	36.0	32.4	31.3	1.1	0.016
	Single Pipe	34.9	[-]	28.9	6.0	0.014
11	Ø50 - Ø32	36.1	30.1	25.1	5.0	0.018
	Ø50 - Ø38	36.8	28.8	26.0	2.8	0.016
	Single Pipe	35.6	[-]	22.1	13.5	0.014
12	Ø50 - Ø32	36.5	30.4	26.3	4.1	0.018
	Ø50 - Ø38	37.3	29.3	26.9	2.4	0.016
	Single Pipe	35.8	[-]	23.1	12.7	0.014

4.2.2 Case 2; Icing

During the icing experiment, the circulation pump were turned off. Hence, the PLC logging data are not interesting in this case. Selected images from the GoPro-camera time laps photos are presented below (ref. figure 4.15).



(a) Time 45 sec.



(b) Time 10 min.



(c) Time 1 hour.

Figure 4.15: Icing experiment from start to end. Total icing time is approx. 1 hour.

4.2.3 Case 3; De-icing

The de-icing experiment started with inlet water temperature $T_{in} = 40^{\circ}C$. Due to slow melting rate, the inlet temperature setting was increased to $80^{\circ}C$ after one hour. This is shown by the inlet temperature graph in figure 4.16, and the pictures in figure 4.17 taken at different times during the de-icing experiment. After almost two hours, the freezing container started defrosting. Hence, the circulation pump was stopped to avoid increasing air temperature. Due to relative stable air temperature, the circulation pump was restarted after 20 min. while the container still was in defrost mode. After 40 min. ($t=150$ min.) the freezing container was restarted. After three hours more than 50 % of the pipe surface is free of ice (ref. figure 4.17d), and it can be seen from the temperature plots that the heat transfer increases. Because of the problems with the freezing container, the de-icing experiment should have been repeated. However, these results was considered as the best possible within the limitations of the freezing container. Therefore, further icing and de-icing experiment must be planned with a modified freezing system.

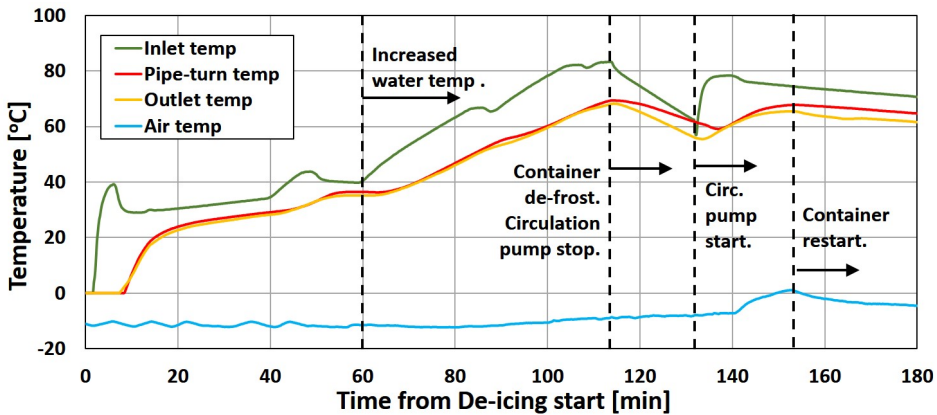


Figure 4.16: Time dependent temperature plot of the De-Icing Experiment.

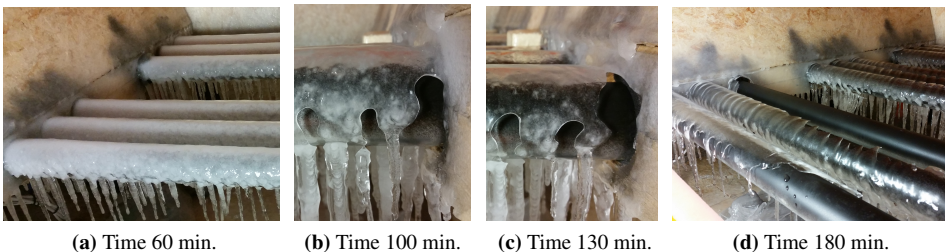


Figure 4.17: Photographs of different parts of the pipes at different times during the De-Icing experiment.

Results and discussion

Theoretical analysis and experiments have shown that icing is a complex mechanism involving heat/mass transfer, phase transitions and variable material properties. The main purpose of the experiments was to verify the theoretical and numerical models, and to develop a facility for Ulmatec Pyro to test their double pipe de-icing systems. The tests have revealed that the laboratory facility need improvements to be able to test for more extreme Polar conditions. The current conditions of the laboratory only allows testing down to $-10^{\circ}C$ and wind velocities up to maximum $10m/s$, while extreme conditions are $T_{air} = -45^{\circ}C$ and $U_{wind} = 20m/s$. In the following sections the numerical and experimental results will be compared and discussed further.

5.1 Anti-icing experiments vs. 1D simulations

Anti-icing experiments were conducted without water spray, similar to the simulation models. During the experiments, the following variables were tested; water flow rate V_{flow} , water inlet temperature T_{in} , air temperature T_{∞} , wind velocity U_{wind} for three different pipe geometries with the same outer diameter ($\varnothing 50mm$) and length (approx. $2.5m$). The experiments show that the double pipe design results in a more uniform surface temperature than the single pipe design (ref. figure 4.13 in section 4.2.1). The IR-images in figures 5.1, 5.2 and 5.3 show surface temperature distribution for the three different pipe designs. The shown tests 4, 7 and 10 are all at $0m/s$ wind velocity. These all show a more uniform temperature distribution for the double pipes, and that the double pipe with the highest flow velocity in the annulus ($\varnothing 50-\varnothing 38$) has the most uniform surface temperature. The IR-images in figures 5.4, 5.5 and 5.6 show surface temperature distributions at wind velocity $\sim 2.6m/s$ (test 2, 5 and 11). The IR-images of the tests exposed to wind velocity show non continuous temperature profiles (temperature "jumps"). This can be explained by non steady state conditions. Hence, a time delay between the flow temperatures and the surface temperatures (ref. figure 5.8). Another factor affecting the time delay in the system is the "dead-volumes" between the pipe sections (insulation "box" ref. figure 4.5).

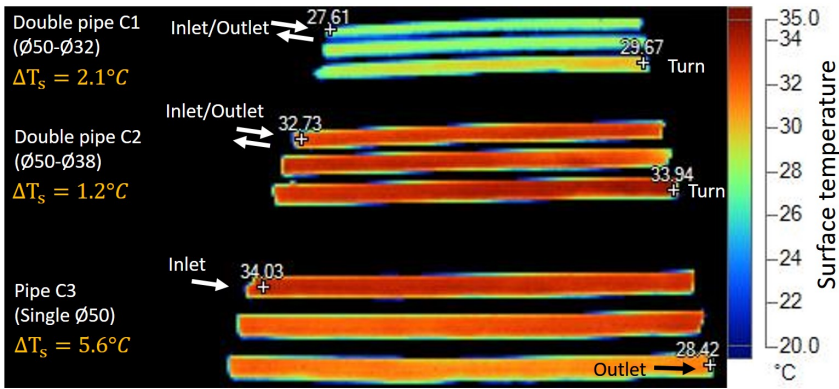


Figure 5.1: Test 4: $V_{flow} \approx 0.01[m^3/h]$, $T_{in} \approx 40[^\circ C]$, $T_\infty \approx -10[^\circ C]$ and $U_{wind} = 0[m/s]$.

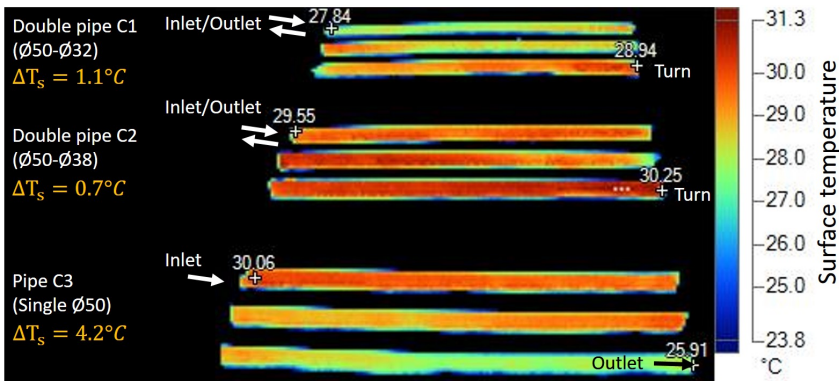


Figure 5.2: Test 7: $V_{flow} \approx 0.02[m^3/h]$, $T_{in} \approx 20[^\circ C]$, $T_\infty \approx -10[^\circ C]$ and $U_{wind} = 0[m/s]$.

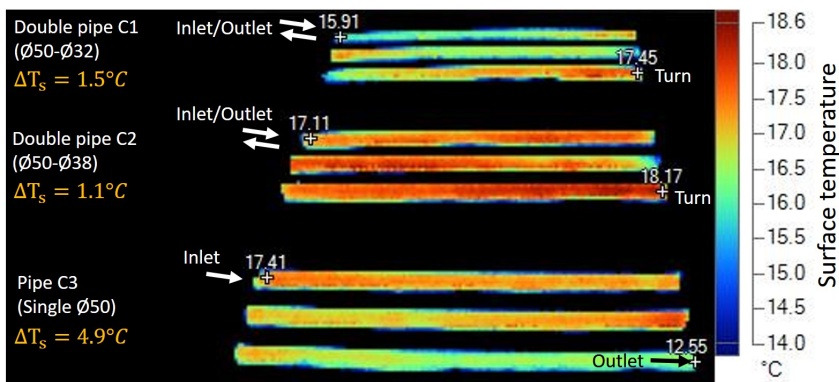


Figure 5.3: Test 10: $V_{flow} \approx 0.02[m^3/h]$, $T_{in} \approx 40[^\circ C]$, $T_\infty \approx -10[^\circ C]$ and $U_{wind} = 0[m/s]$.

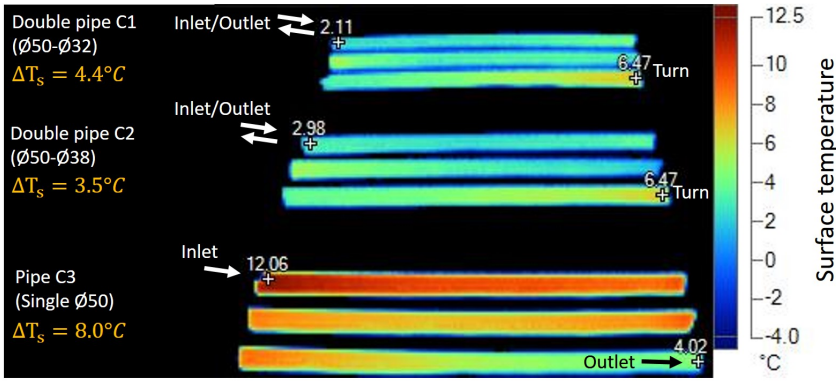


Figure 5.4: Test 2: $V_{flow} \approx 0.01[m^3/h]$, $T_{in} \approx 20[^\circ C]$, $T_\infty \approx -10[^\circ C]$ and $U_{wind} = 2.6[m/s]$.

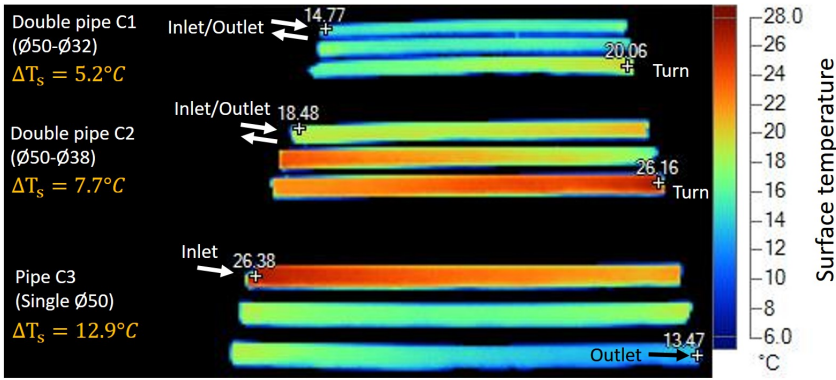


Figure 5.5: Test 5: $V_{flow} \approx 0.01[m^3/h]$, $T_{in} \approx 40[^\circ C]$, $T_\infty \approx -10[^\circ C]$ and $U_{wind} = 2.6[m/s]$.

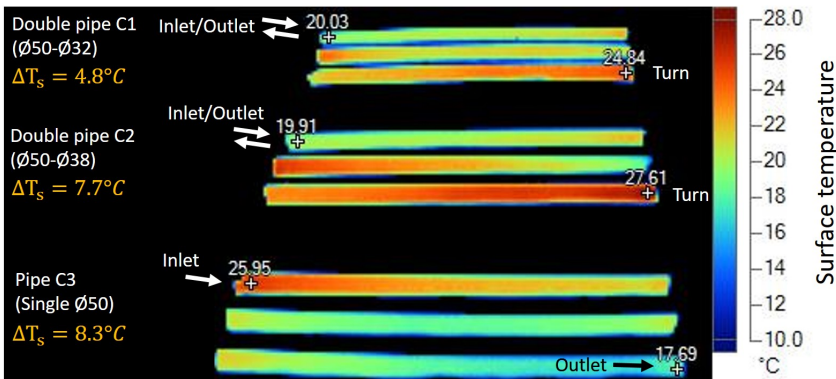


Figure 5.6: Test 11: $V_{flow} \approx 0.02[m^3/h]$, $T_{in} \approx 40[^\circ C]$, $T_\infty \approx -10[^\circ C]$ and $U_{wind} = 2.6[m/s]$.

Theoretical simulations confirmed that the 1D axisymmetrical model (MATLAB) shows sufficient accuracy compared with the 2D axisymmetrical simulation model (COMSOL) (ref. figure 3.13 and 3.14). Due to simulation time, the 1D model was used for experimental comparison. New simulations for the double pipes were performed with the same boundary conditions as the experiments to compare simulations and experimental results summarized in table 5.1 and 5.2. Table 5.1 represent the water flow temperatures from test 1, 4, 7 and 10, where the wind velocity is 0m/s. Table 5.2 represent the water flow temperatures from test 2, 5, 8 and 11, where the wind velocity is 2.6m/s. For higher wind velocities see table 4.5 in chapter 4. ΔT_L represent the temperature difference of the water flow in the pipe annulus ($T_{turn} - T_{out}$). The input parameters used in the 1D axisymmetrical simulation model are; water flow rate V_{flow} , water inlet temperature T_{in} , air temperature T_{∞} , wind velocity U_{wind} and pipe geometry ($\frac{A_1}{A_2}$ and L). Only the results for wind velocity 2.6m/s and 0m/s are further analyzed due to freezing container instability for higher wind velocities.

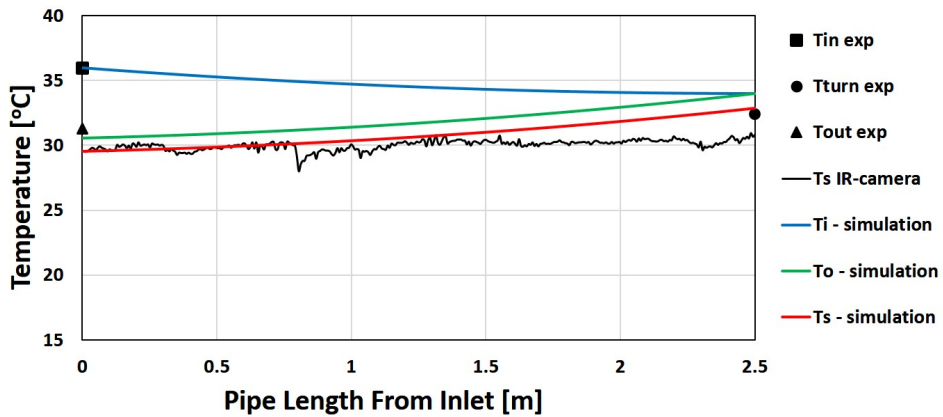
For wind velocity 0m/s, the simulations and experimental results show good correlations. However, for wind velocity 2.6m/s the surface temperature plots obtained from the IR-images show temperature "jumps", indicating unsteady state conditions (ref. figure 5.10). Similar water temperature differences between simulations and experiments are also shown in table 5.2. These temperature differences can be related to the temperature "jumps" seen in the IR-images. As mentioned earlier, this is related to unsteady state conditions and "dead-volumes" in the insulation "box". This unsteady state problems increase with increasing wind velocities.

Table 5.1: Results from the PLC and numerical simulations for the tests with **wind velocity 0m/s**.

Test	Data source and pipe dimensions [mm]	Water flow temperature			ΔT_L [$^{\circ}C$]	Flow [m^3/h]
		T_{in} [$^{\circ}C$]	T_{turn} [$^{\circ}C$]	T_{out} [$^{\circ}C$]		
1	Simulation $\text{\O}50 - \text{\O}32$	16.9	14.3	12.1	2.2	0.008
	Experiment $\text{\O}50 - \text{\O}32$	16.9	14.3	11.5	2.8	0.008
	Simulation $\text{\O}50 - \text{\O}38$	17.4	12.5	11.8	0.7	0.0064
	Experiment $\text{\O}50 - \text{\O}38$	17.4	13.7	12.7	1.0	0.0064
4	Simulation $\text{\O}50 - \text{\O}32$	38.3	33.6	29.2	4.4	0.009
	Experiment $\text{\O}50 - \text{\O}32$	38.3	30.6	27.9	2.7	0.009
	Simulation $\text{\O}50 - \text{\O}38$	40.1	32.5	29.8	2.7	0.008
	Experiment $\text{\O}50 - \text{\O}38$	40.1	32.5	32.1	0.4	0.008
7	Simulation $\text{\O}50 - \text{\O}32$	21.1	20.2	17.9	2.3	0.016
	Experiment $\text{\O}50 - \text{\O}32$	21.1	19.3	17.5	1.8	0.016
	Simulation $\text{\O}50 - \text{\O}38$	21.4	20.6	18.7	1.9	0.02
	Experiment $\text{\O}50 - \text{\O}38$	21.4	19.1	18.3	0.8	0.02
10	Simulation $\text{\O}50 - \text{\O}32$	35.6	34.3	30.8	3.5	0.018
	Experiment $\text{\O}50 - \text{\O}32$	35.6	33.1	29.9	3.2	0.018
	Simulation $\text{\O}50 - \text{\O}38$	36.0	34.0	30.5	3.5	0.016
	Experiment $\text{\O}50 - \text{\O}38$	36.0	32.4	31.3	1.1	0.016

Table 5.2: Results from the PLC and numerical simulations for the tests with **wind velocity 2.6m/s**.

Test	Data source and pipe dimensions [mm]	Water flow temperature			ΔT_L [$^{\circ}C$]	Flow [m^3/h]
		T_{in} [$^{\circ}C$]	T_{turn} [$^{\circ}C$]	T_{out} [$^{\circ}C$]		
2	Simulation $\varnothing 50 - \varnothing 32$	19.1	10.8	4.5	6.3	0.008
	Experiment $\varnothing 50 - \varnothing 32$	19.1	9.1	3.8	5.3	0.008
	Simulation $\varnothing 50 - \varnothing 38$	20.2	6.1	4.1	2.1	0.0064
	Experiment $\varnothing 50 - \varnothing 38$	20.2	5.9	4.9	1.0	0.0064
5	Simulation $\varnothing 50 - \varnothing 32$	36.1	24.4	13.9	10.5	0.009
	Experiment $\varnothing 50 - \varnothing 32$	36.1	22.5	17.1	5.4	0.009
	Simulation $\varnothing 50 - \varnothing 38$	39.1	20.6	14.0	6.6	0.008
	Experiment $\varnothing 50 - \varnothing 38$	39.1	25.5	21.8	3.7	0.008
8	Simulation $\varnothing 50 - \varnothing 32$	16.7	14.1	7.5	6.6	0.016
	Experiment $\varnothing 50 - \varnothing 32$	16.7	12.3	8.5	3.6	0.016
	Simulation $\varnothing 50 - \varnothing 38$	17.2	14.7	8.6	6.1	0.020
	Experiment $\varnothing 50 - \varnothing 38$	17.2	10.9	8.2	3.7	0.020
11	Simulation $\varnothing 50 - \varnothing 32$	36.1	32.1	21.2	10.9	0.018
	Experiment $\varnothing 50 - \varnothing 32$	36.1	30.1	25.1	5.0	0.018
	Simulation $\varnothing 50 - \varnothing 38$	36.8	30.2	19.4	10.8	0.016
	Experiment $\varnothing 50 - \varnothing 38$	36.8	28.8	26.0	2.8	0.016

**Figure 5.7:** Test 10: $T_{in} = 36.0^{\circ}C$, $V_{flow} = 0.016m^3/h$ and $U_{wind} = 0m/s$.

Figures 5.7 and 5.8, show the two tests 10 and 11. They are exposed to the same conditions, except the wind velocity $0m/s$ and $2.6m/s$, respectively. The results for wind velocity $0m/s$, show good correlation with the numerical models (ref. figure 5.7). For test 11 with wind velocity $2.6m/s$ (ref. figure 5.8), the correlation between numerical models and experimental results show the before mentioned temperature "jumps", which are related

to unsteady state conditions. For wind velocity 2.6m/s , the temperature "jumps" are approximately $\sim 2^{\circ}C$ in the first pipe bend and $\sim 3^{\circ}C$ in the second bend. This give a total temperature "jump" of $\sim 5^{\circ}C$. However, compensating for the temperature "jumps", the correlation between the numerical simulations and the experimental results are quiet good (T_{out} and T_s). These temperature jumps are caused by the delay in the "dead-volumes" in the insulation "box". This problem can only be solved by increasing the capacity of the freezing system, allowing time to reach steady state conditions.

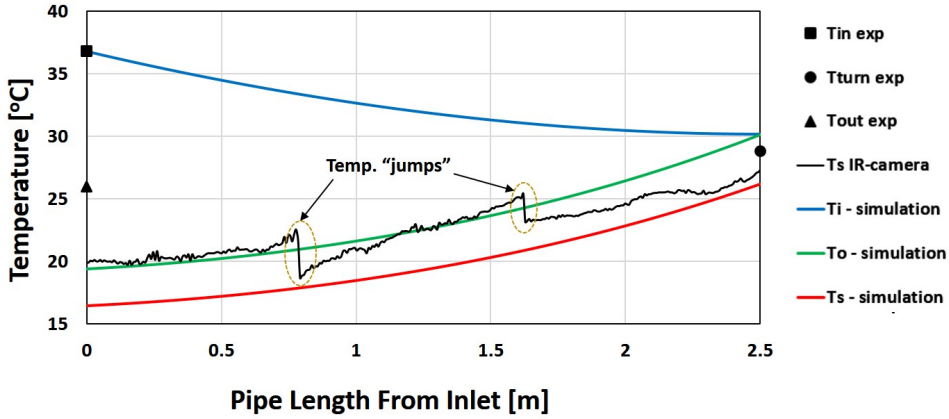


Figure 5.8: Test 11: $T_{in} = 36.8^{\circ}C$, $V_{flow} = 0.016m^3/h$ and $U_{wind} = 2.6m/s$.

Based on the IR-camera images, surface temperature distribution for tests with wind velocities 0m/s, 2.6m/s and 5.8m/s are measured and plotted in figures 5.9, 5.10 and 5.11 respectively. In the same plots, numerical simulations are also plotted to compare with the experimental results. The numerical simulations plotted in figures 5.9, 5.10 and 5.11 are based on the experimental water inlet temperatures and water flow rates. As mentioned earlier, the test with wind velocity 0m/s correlates well with the numerical simulations and the tests with wind velocity 2.6m/s and 5.8m/s show temperature "jumps" indicating unsteady state conditions. Hence, the tests with wind velocity 2.6m/s and 5.8m/s can not be compared with the numerical simulation directly.

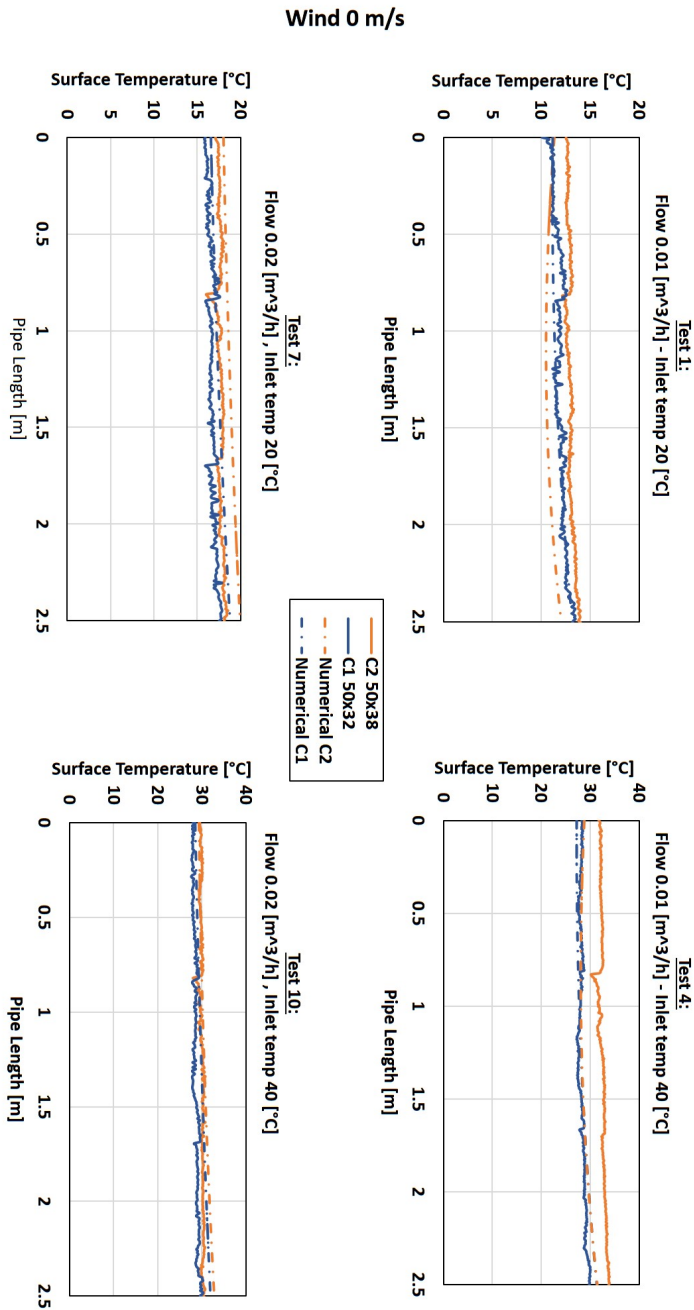


Figure 5.9: Surface temperatures for wind velocity of 0 [m/s], test number 1, 4, 7 and 10. C1 refers to the double pipe 50x32, and C2 refers to 50x38. The plot combines the experimental result (IR-camera) and numerical results from the 1D axisymmetrical model with the same conditions as the experimental data (ref. table 5.1).

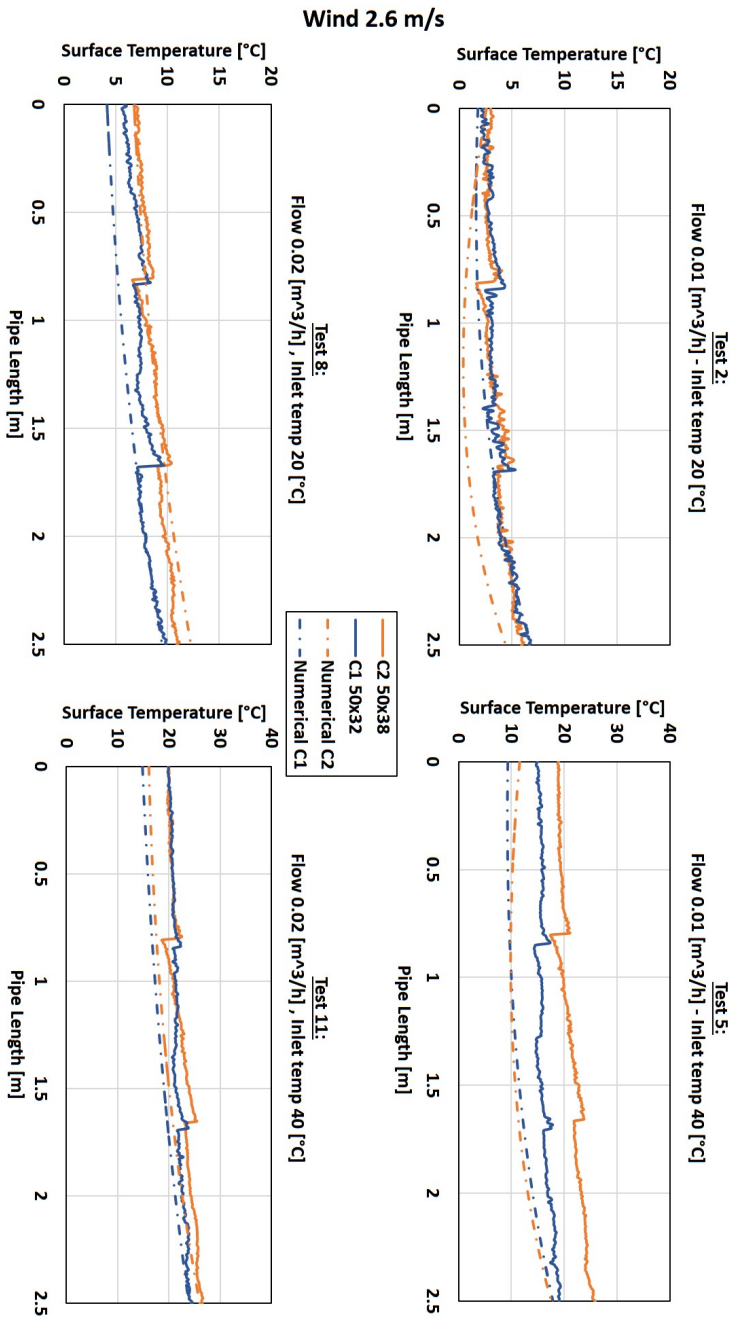


Figure 5.10: Surface temperatures for wind velocity of 2.6 [m/s], test number 2, 5, 8 and 11. C1 refers to the double pipe 50x32, and C2 refers to 50x38. The plot combines the experimental result (IR-camera) and numerical results from the 1D axisymmetrical model with the same conditions as the experimental data (ref. table 5.2).

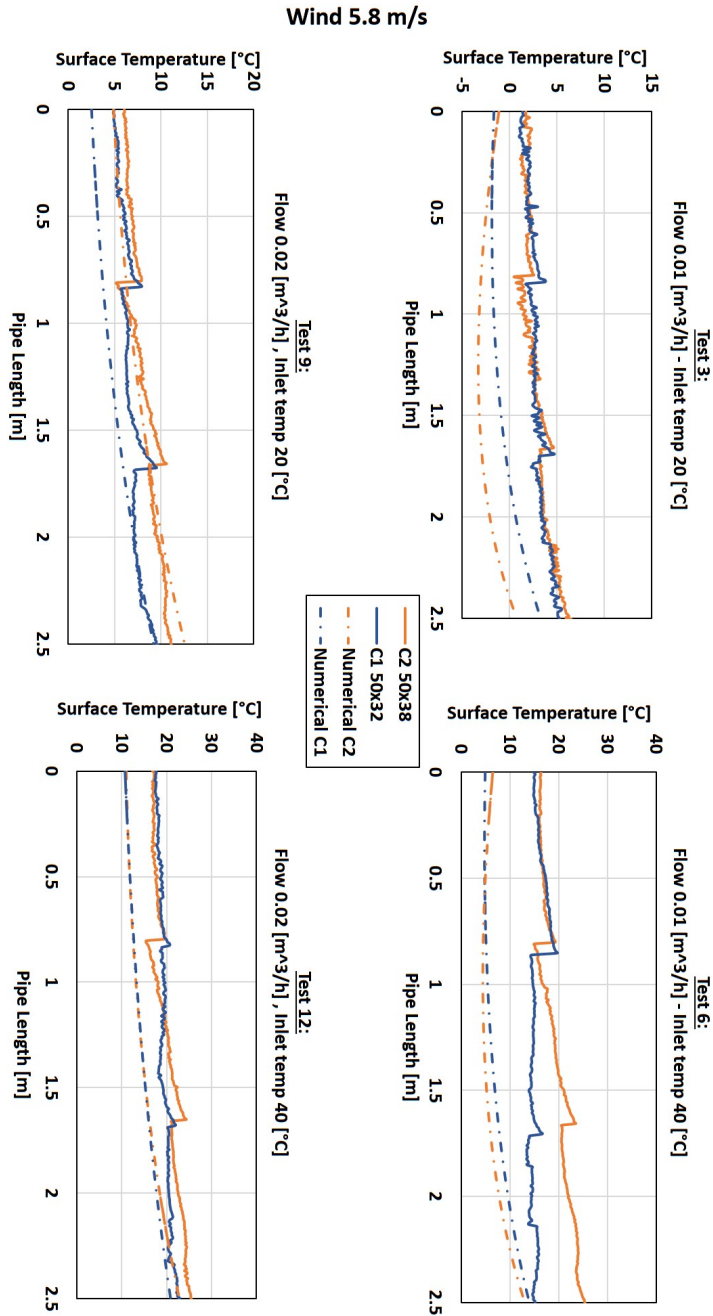


Figure 5.11: Surface temperatures for wind velocity of 5.8 [m/s], test number 3, 6, 9 and 12. C1 refers to the double pipe 50x32, and C2 refers to 50x38. The plot combines the experimental result (IR-camera) and numerical results from the 1D axisymmetrical model with the same conditions as the experimental data (ref. table 4.5).

5.1.1 Experimental heat transfer coefficients

Based on the experimental results, the heat transfer coefficient h_{air} is calculated using the following energy balance equation:

$$h_{air} = \frac{V_{flow} \cdot \rho_w \cdot c_p (T_{w_{in}}) - T_{w_{out}}}{A_s \cdot (T_{s_{avg}} - T_{air})} \quad (5.1)$$

Figure 5.12 show the theoretical heat transfer coefficient h_{air} used in the 1D numerical simulation model. Based on experimental water flow rates (V_{flow}), water flow temperatures ($T_{w_{in}}$ and $T_{w_{out}}$), air temperature (T_{air}) and wind velocity (U_{air}) found in table 5.3 for the three pipe designs Ø50-Ø32, Ø50-Ø38 and Ø50-single respectively. Here, the thermal properties of water $\rho_w = 1000[kg/m^3]$ and $c_p = 4200[J/kgK]$ are used in the calculations.

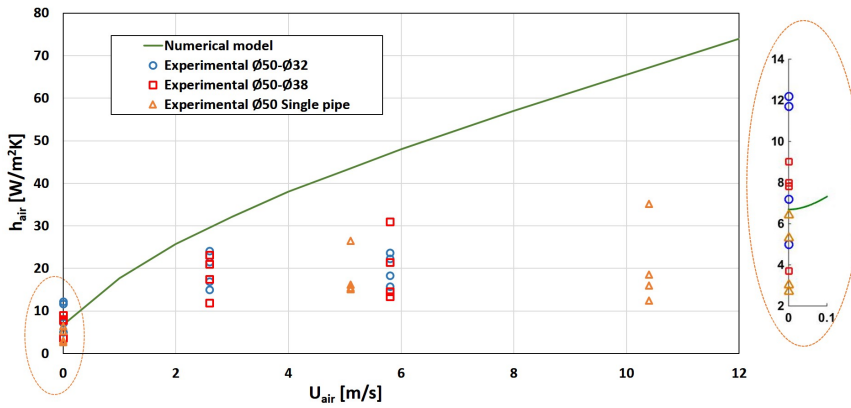


Figure 5.12: Heat transfer coefficient h_{air} for theoretical simulations and experimental results.

The results show a significantly lower heat transfer rate than theoretically expected. For natural convection (0m/s wind), the results are close to the theory. However, as wind velocity increase, the deviation between experiments and theory increase. This may be explained mainly by the unsteady conditions and also that the variable air velocities measured. Hence, these values can not be compared directly, and new experiments with more steady state conditions are required. At steady state the water outlet temperature $T_{w_{out}}$ will decrease resulting in a higher heat transfer coefficient (ref. equation 5.1). Hence, the experimental value will be closer to the theoretical heat transfer coefficient used in the theoretical simulation model. From the tests with wind velocity 0m/s the heat transfer coefficients found from the experiments are relatively close to the expected theoretical value (ref. figure 5.12). Variations are expected due to variations in natural convection over the test section. Another factor affecting the calculation of the experimental heat transfer coefficient, is the water flow rate. The flow rate measurements may be inaccurate due to the sensor calibration factor (flow rate) and measurement accuracy for the flow sensors. For more accurate measurements, a more accurate flow sensors are required for both water and air flow measurements.

Table 5.3: Heat transfer coefficient h_{air} calculation table.

Test	$T_{w_{in}}$ °C	$T_{w_{out}}$ °C	$T_{s_{avg}}$ °C	V_{flow} m^3/h	Q_{tot} W/m^2	T_{air} °C	U_{air} m/s	h_{air} W/m^2K
Double pipe Ø50-Ø32								
1	16.6	11.5	12	0.008	119	-10.8	0.0	5.0
2	19.1	3.8	3.7	0.008	357	-10.8	2.6	15.0
3	17.1	2.8	3.0	0.008	333	-8.2	5.8	15.7
4	38.3	27.9	28.4	0.009	273	-10.3	0.0	11.7
5	36.1	17.1	16.3	0.009	498	-10.1	2.6	21.6
6	36.4	20.3	15.4	0.009	422	-10	5.8	18.3
7	21.1	17.5	16.8	0.016	168	-10.2	0.0	7.2
8	16.7	8.5	7.6	0.016	382	-9.6	2.6	16.9
9	19.7	8.9	6.8	0.016	503	-9.6	5.8	22.3
10	35.6	29.9	28.7	0.018	299	-11.4	0.0	12.2
11	36.1	25.1	21.8	0.018	577	-10.9	2.6	24.1
12	36.5	26.3	19.6	0.018	535	-9.6	5.8	23.7
Double pipe Ø50-Ø38								
1	17.4	12.7	13	0.0064	88	-10.8	0.0	3.7
2	20.1	4.9	3.6	0.0064	283	-10.8	2.6	11.9
3	17.8	2.6	2.98	0.0064	283	-8.2	5.8	13.4
4	40.1	32.1	32.6	0.008	186	-10.3	0.0	8.0
5	39.1	21.8	21.4	0.008	403	-10.1	2.6	17.5
6	39.5	25.1	19.6	0.008	336	-10	5.8	14.6
7	21.4	18.3	17.7	0.020	181	-10.2	0.0	7.8
8	17.2	8.2	8.8	0.020	524	-9.6	2.6	23.2
9	20.4	8.4	8.3	0.020	699	-9.6	5.8	30.9
10	36	31.3	30	0.016	219	-11.4	0.0	9.0
11	36.8	26	22.6	0.016	503	-10.9	2.6	21.1
12	37.3	26.9	20.3	0.016	485	-9.6	5.8	21.4
Ø50 single pipe								
1	17.4	13.5	14	0.007	70	-10.8	0.0	3.0
2	20.2	5	7.7	0.007	273	-10.8	5.1	15.4
3	18.3	2.7	5.1	0.007	280	-8.2	10.4	18.6
4	38.6	33.2	31	0.008	111	-10.3	0.0	2.7
5	36.9	16.1	18.3	0.008	427	-10.1	5.1	15.1
6	36.6	19.9	17.5	0.008	343	-10	10.4	12.5
7	21.2	17	17	0.016	172	-10.2	0.0	6.4
8	17.3	5.9	7.7	0.016	468	-9.6	5.1	26.4
9	20.3	6	6.7	0.016	587	-9.6	10.4	35.2
10	34.6	28.9	29	0.014	205	-11.4	0.0	5.3
11	35.6	22.1	20	0.014	485	-10.9	5.1	16.2
12	35.8	23.1	18.5	0.014	456	-9.6	10.4	16.0

5.1.2 Design simulations for Polar Code Conditions

The following simulations are conducted for typical design environmental conditions (ref DNV GL table 2.2). "Basic" environment; air temperature $T_\infty = -10^\circ C$, wind velocity $U = 20m/s$. "Cold" environment; air temperature $T_\infty = -30^\circ C$, wind velocity $U = 20m/s$. "Polar" environment; air temperature $T_\infty = -45^\circ C$, wind velocity $U = 20m/s$. The water flow is adjusted to give minimum surface temperature of approximate $T_s \approx 10^\circ C$. For all the simulations a double-pipe $\text{Ø}50\text{-Ø}38$ with a pipe-length of $L = 30m$ is used.

- For "Basic" condition, the results in figure 5.13 show that the minimum flow required for this pipe geometry is $\sim 0.15m^3/h$, giving a total heat transfer rate of approx. $11kW$ or $2.3kW/m^2$.
- For "Cold" condition, the results in figure 5.14 show that the minimum flow required for this pipe geometry is $\sim 0.4m^3/h$, giving a total heat transfer rate of approx. $26kW$ or $5.4kW/m^2$.
- For "Polar" condition, the results in figure 5.15 show that the minimum flow required for this pipe geometry is $\sim 0.6m^3/h$, giving a total heat transfer rate of approx. $35kW$ or $7.4kW/m^2$.

These simulations are based on theoretical heat transfer coefficients. Hence, experiments to validate these models under extreme Polar conditions are needed. The simulations are conducted without the effect of water spray since water spray is not defined in DNV GL's rules and regulations (ref. table 2.2).

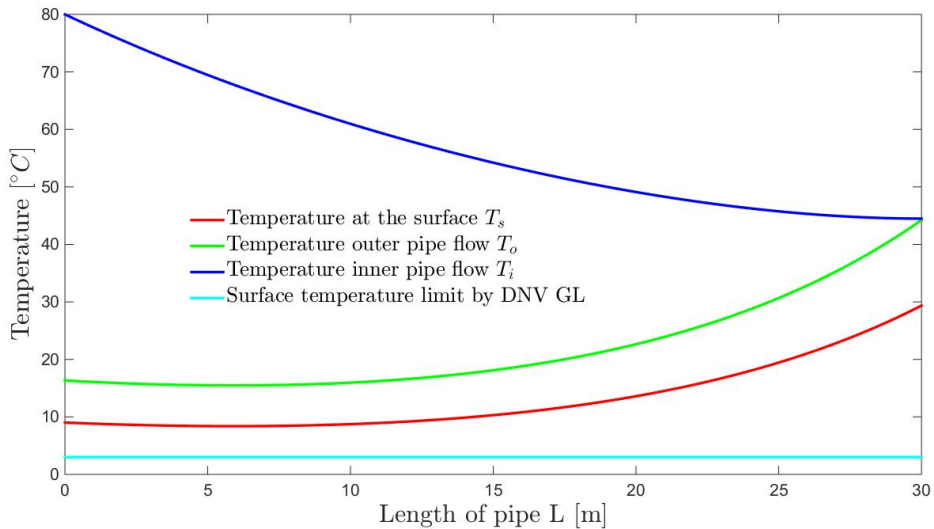


Figure 5.13: Double pipe simulations for "Basic" condition; $T_\infty = -10^\circ C$, $U = 20m/s$ and $V_{flow} = 0.15m^3/h$

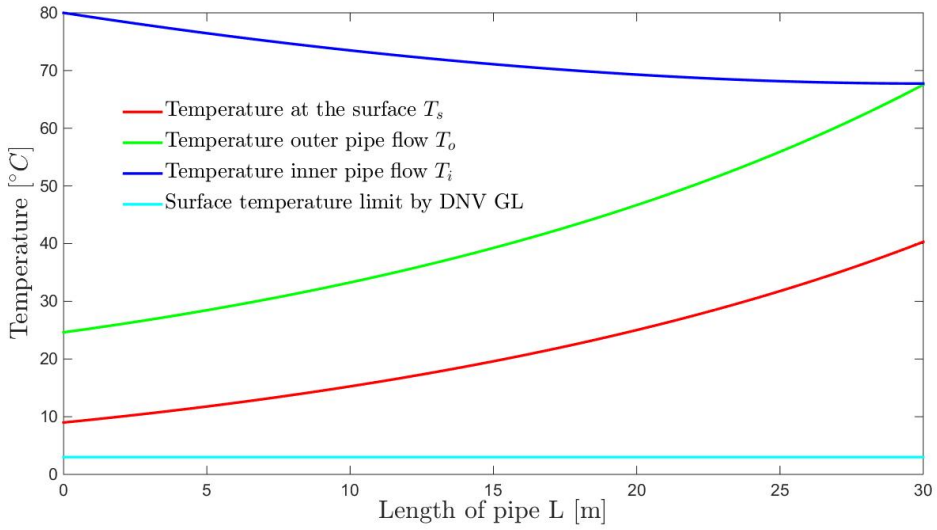


Figure 5.14: Double pipe simulations for "Cold" condition; $T_\infty = -30^\circ\text{C}$, $U = 20\text{m/s}$ and $V_{flow} = 0.4\text{m}^3/\text{h}$

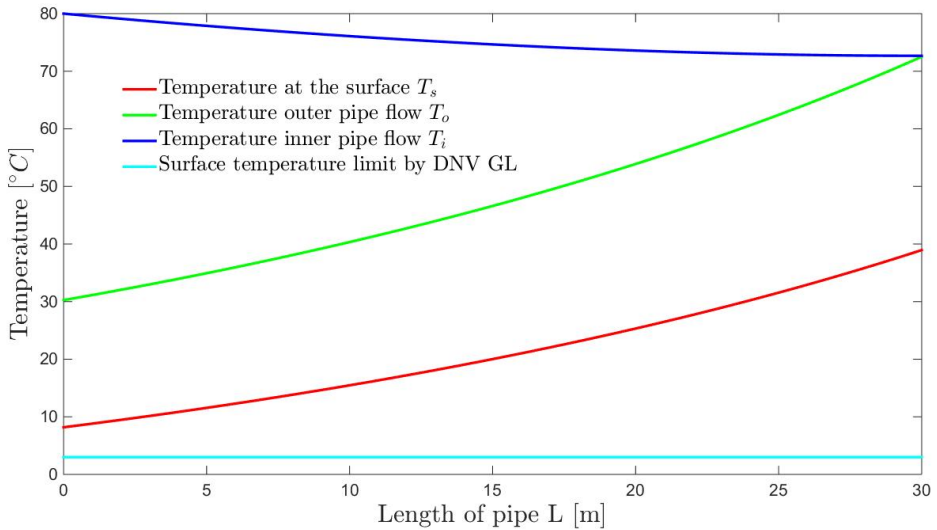


Figure 5.15: Double pipe simulations for "Polar" condition; $T_\infty = -45^\circ\text{C}$, $U = 20\text{m/s}$ and $V_{flow} = 0.6\text{m}^3/\text{h}$

5.2 Icing experiment

Figure 5.16 show 3 pictures of the icing process. Fresh water was used to avoid corrosion inside the icing simulation chamber. Hence, pure ice were applied. Due to freezing container limitations, icing under extreme conditions were not possible to test. Hence, a simple icing test were conducted mainly for later de-icing purposes. A caliper was used to measure the ice thickness. The formation and the average ice thickness that were measured is shown in figure 5.17. Sea water icing is left for future work, when the freezing system capacity is increased.

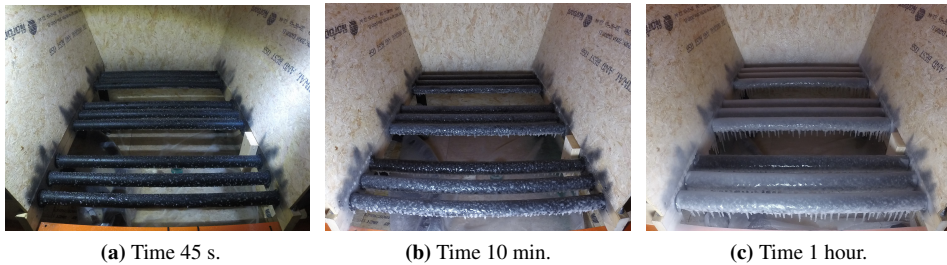


Figure 5.16: Icing process; The pictures taken with a GoPro camera in between every water spray.

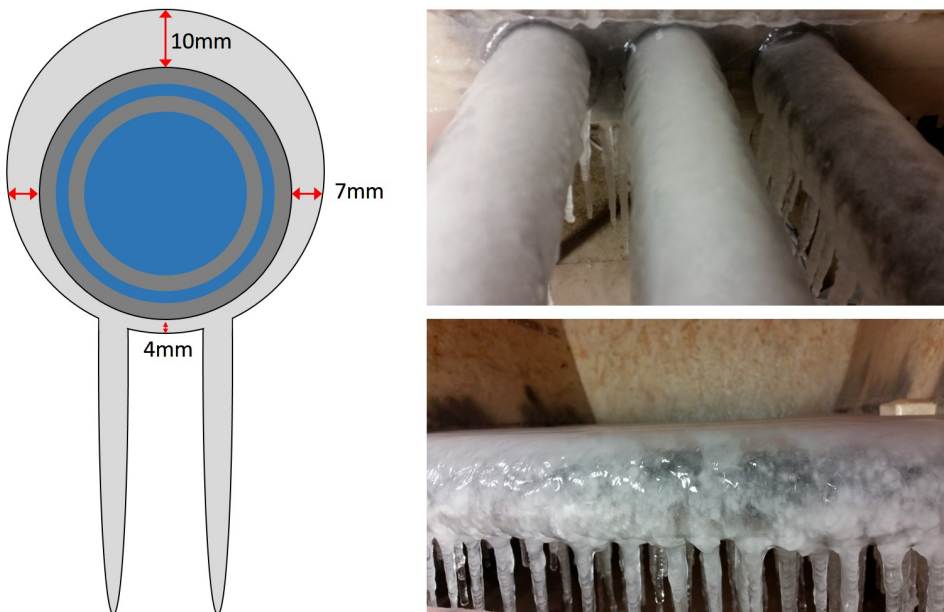


Figure 5.17: Ice dimensions after the icing experiment. The ice thickness is approximately 10mm at the top, 7mm on the sides and 4mm at the bottom.

5.3 De-icing simulations vs. experiments

The theoretical de-icing simulation model indicated a de-icing time of approximate one hour for an ice thickness of 10mm. However, this 2D axisymmetrical model is relatively simple assuming that the water is trapped between the ice and the pipe wall, and no water will drain during the melting process. As predicted in section 3.4.2, water will drain, leaving insulating pockets of air between the ice and the pipe surface. Hence, practical experiments are needed to find the actual de-icing time due to irregular ice melting and accretion. The de-icing model need improvements for further use.

Figure 5.18 show a schematic drawing of the de-icing process. The pipe to the left show the ice dimensions before the de-icing process started. As the hot water entered the pipe, the ice started to melt, creating a thin layer of water in between the pipe and the ice. Due to small holes in the ice, the water drained through the holes leaving a layer of air in between the pipe and the ice. Due to low conductivity of air ($\sim 0.02[W/m^2K]$ ref equation A.5), the layer of air work as an insulator rather than a conductor. Hence, the melting rate decrease drastically and the small amount of water which is still melting freeze onto the growing icicles (ref. figure 5.18).

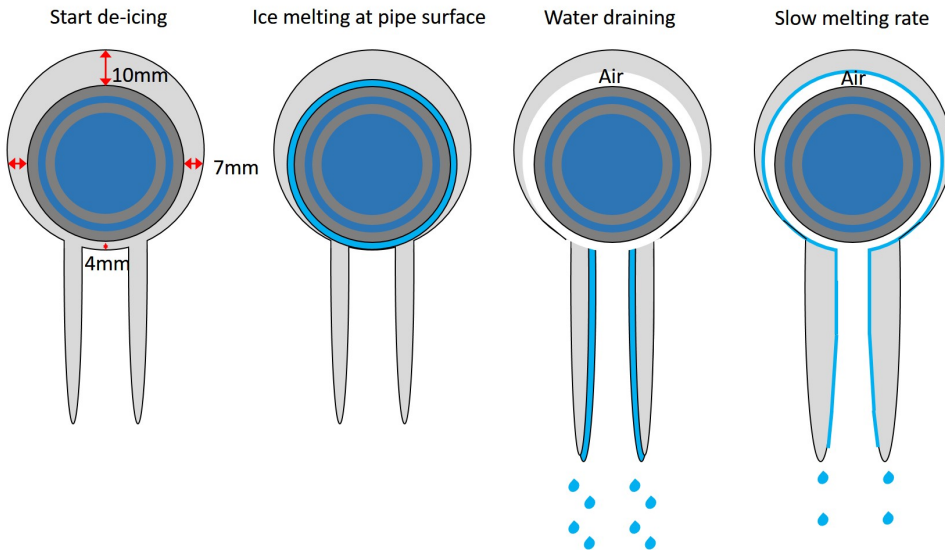


Figure 5.18: Schematic drawing of the de-icing process.

The GoPro pictures taken during the experiment showed that the water started to melt immediately after the hot water entered the single pipe. For the double pipes, the ice started to melt at the pipe-turn where the hot water-flow entered the annulus, as expected. From the GoPro pictures, it was observed that after 320 seconds, the ice on all three pipes had started to melt. This correlates well with the de-icing temperature plot shown in figure 4.16 in section 4.2.3, showing the water temperature in the annulus increasing above $0^{\circ}C$ after approx 7 minutes. Then all the melted ice drained. After one hour, the inlet temperature

were increased due to the slow melting process (ref. figure 4.16). The total de-icing time of this experiment was approx. three hours.

When the de-icing process was declared complete after 3 hours, images was taken with the infrared camera, ref. figure 5.19. It can easily be seen where the pipes are exposed to the air. Figure 5.19 show the same picture with two different temperature scales, and one with visible light, to show where the ice is in relation to the pipes.

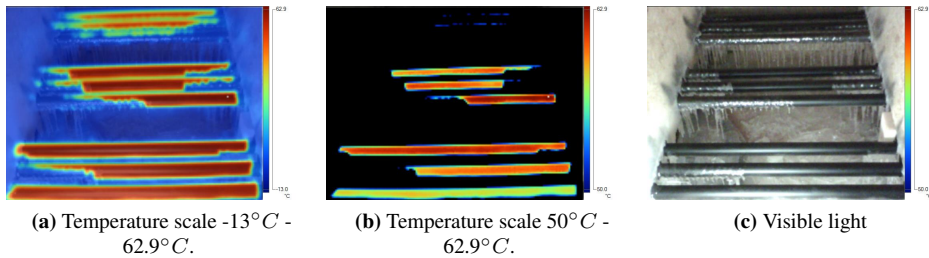


Figure 5.19: Infrared picture taken at the end of the De-Icing experiment.



Figure 5.20: Picture showing the insulating layer of air between the pipe surface and the ice.

De-icing using heat creates some extra challenges. Due to the insulating layer of air caused by water draining, the melting process is slowed down and may stop due to equilibrium state (air layer and slow melting rate ref. figure 5.20). With a slow melting rate, the ice growth of the outer surface of the ice may even be greater than the melting rate. The melting water may freeze on another surface, just moving the ice to a different location on the vessel. This is also a well known problem from de-icing systems on air-planes [11]. Hence, de-icing using heat should be combined with some kind of mechanical removal of the ice.

An attempt to extend the de-icing simulation model to include water-draining/air-layer was made. However, material properties of ice/water/air caused numerical problems and therefore, this attempt was left for further theoretical studies and experiments. Further work should also include saline ice both in simulation models and experiments.

5.4 Experimental uncertainty and test rig modification

Practical experiments have sources of error due to measuring instrument accuracy, geometry tolerances, unsteady conditions and synchronizing data logging. The numerical simulations are based on ideal pipe geometry and steady state conditions, and do not take the pipe bends into consideration. Hence, the minor heat loss through the insulation "box" and the flow effect inside the pipe connections are not included in the simulation model. The pipe bends are constructed with "dead-volumes" also affecting the time to reach steady state conditions. These "dead-volumes" in combination with the freezing container limitations made it impossible to reach steady state conditions with wind velocities.

The IR-camera used to measure the surface temperature also has limitations due to image resolution. The camera measuring distance also vary for each of the pipe sections (1m between the pipes at each end). The IR-camera images was useful in order to discover the temperature "jumps", which indicate unsteady state.

It was observed that the fan/frequency-converter affected the water flow sensors (electromagnetic noise). Hence, flow measurements for the 0m/s measurements were used for the tests with 2.6m/s and 5.8m/s. The flow sensors are based on quite simple commercial applications, and not suitable for accurate laboratory use.

Due to turbulence in the air flow, the wind velocity varies over the test section. Hence, the average velocity measured was used when comparing with numerical simulations. For more accurate testing the location of the fan(s) and air ducting should be improved. Also a more accurate air flow velocity measurements is required.

The freezing system does not have enough capacity to keep the air temperature at steady state conditions while using the fan for wind velocities. Due to these freezing container capacity limitations, modifications are needed before further testing. The fan also has a wind velocity limitation for the double-pipes of approx. 5m/s, which could be increased by modifying the duct to a smaller test section. The icing simulation chamber size limits the test rig design and the location of the fan in relation to the test section. For further testing, the test rig need improvements to be able to test more extreme conditions (ref. Polar Codes). Suggestions for test rig modifications are listed below:

1. Increasing the test section size, using the whole twenty-foot container as the icing simulation chamber. This will make it possible to place the pipes at a longer distance from the fan, and test longer pipe sections without pipe bend connections.
2. Test one pipe design at a time. Hence, the test section can be reduced making it possible to increase the air flow velocities and reduce the freezing system requirements.
3. New fan with higher capacity, or multiple fans placed beside each other for a more uniform air velocity. Also, the fan should be placed so that the air circulating inside the simulation chamber do not counteract the circulation through the freezing system.
4. Freezing system need improvement to increase the capacity.
5. Better insulation of the pipes between the FCU and the test section.
6. Install a permanent water spray system for icing tests.
7. Select a more accurate water flow sensor.

5.5 Suggestions for further work

5.5.1 Theoretical model modifications

The theoretical simulation models are based on simplifications and assumptions creating sources of simulation errors. The 1D numerical anti-icing simulations model showed good correlations with the experimental results at steady state conditions. Hence, the assumptions made for the numerical anti-icing models are sufficient. For the de-icing simulation model, the assumptions are too simplified and does not give realistic results. Hence, the model should be modified for further use:

1. Model the water draining leaving an air layer between the pipe surface and the ice.
2. A full 3D model with unsymmetrical ice (realistic ice). Using data from icing experiments with saline ice for a realistic modelling of the ice (for example, [9]).
3. Material properties of saline ice should be included for the phase change materials. These materials (fresh-water/ice and saline-water/ice) have different melting temperatures and rates due to salinity.

5.5.2 Experiments

The experimental testing were limited due to the icing simulation chamber capacity. Therefore, only limited tests were performed in this study. Testing for more extreme Arctic conditions (Polar Code) will be useful for further model verification's. The 1D anti-icing simulation model were used for design environmental condition simulations (Polar Code) of the following environmental conditions Basic, Cold and Polar (ref. figures 5.13, 5.14 and 5.15). These simulations should be verified by experimental testing. Hence, the test rig should be modified before further testing. Assuming a modified test rig capable of testing the extreme conditions, these tests should be conducted:

1. Verification experiments for the Polar Codes; Basic ($T_{\infty} = -10$ and $U_{wind} = 20m/s$), Cold ($T_{\infty} = -30$ and $U_{wind} = 20m/s$) and Polar ($T_{\infty} = -45$ and $U_{wind} = 20m/s$).
2. Test for longer pipe lengths $L > 3m$ (without bends if possible).
3. Try anti-icing with periodic and/or continuous water spray.
4. More de-icing experiments, with multiple ice thicknesses, and with and without water spray.
5. Test different de-icing double pipe profiles (for example helicopter-deck sections and escape-route profiles using the double pipe technology).

Conclusions

Marine activities in Arctic waters are endangered by ice accretion on critical structures causing various safety risks. The research objectives of this master thesis was to support Ulmatec Pyro in the design process, using theoretical models for design optimization, and to develop an experimental facility to verify their designs to meet the IMO safety requirements. Different Polar Codes are required depending on the vessel classification; Basic ($T_{air} = -10^{\circ}C$ and $U_{wind} = 20m/s$), Cold ($T_{air} = -30^{\circ}C$ and $U_{wind} = 20m/s$) and Polar ($T_{air} = -45^{\circ}C$ and $U_{wind} = 20m/s$). The anti-icing requirements for all Polar Codes is a minimum surface temperature requirement of $T_s > 3^{\circ}C$.

Two different numerical models are developed, based on previous icing studies in combination with thermo- and fluid- dynamics. A 1D axisymmetrical steady state simulation model based on heat and mass transfer theory using finite difference method (FDM) and lumped capacitance method (LCM), was programmed in MATLAB. Further, a 2D axisymmetrical CFD model was modelled in COMSOL Multiphysics to compare with the simple 1D axisymmetrical model.

The 1D simulation model show good correlation with the more advanced 2D CFD model. Hence, due to simulation time the 1D model was preferred for further simulations, to compare with the experimental results. The 2D CFD model was extended to a transient de-icing model, which simulated the phase transition of melting ice. The transient de-icing simulations results show good results within the assumptions that the water is entrapped in the ice. However, the de-icing experiments show that this model must be modified to give more realistic ice-melting behavior. These modifications include water draining, giving an insulating air layer between the ice and the pipe surface, and further include saline ice models.

The experimental setup was designed and built for validating theoretical models, and further as a design verification lab for Ulmatec Pyro. The test lab was built inside a commercial freezing container, which turned out to have insufficient freezing capacity for the extreme Polar test conditions. Despite of these limitations, a series of experiments were conducted, providing valuable insight in the icing- and anti-icing processes. The experi-

mental results show good correlation with the numerical simulation models of anti-icing. Due to freezing capacity limitations, the tests with higher wind velocity were not able to reach steady state conditions. Hence, these test could not be directly correlated to numerical simulations.

The experiments confirm that the double pipe technology is giving a more uniform surface temperature along the pipe, compared to a single pipe. Hence, a more efficient use of waterborne heat is obtained. The results show that the Ø50 – Ø38 double pipe give the best results of the tested pipe designs, due to higher velocity in the outer pipe flow (annulus). The experiments also provided good validation of the theoretical simulation models within the available test conditions. The main parameters effecting the surface temperature are water flow rate, pipe length, water inlet temperatures, air temperatures and wind velocities.

The de-icing test also showed the complexity of the ice melting process. Using heat as a de-icing method presents challenges as the melted ice will drain, leaving an insulating air layer between the heat source and the ice. The insulating layer will slow down or even stop the melting process. Hence, a supplementary de-icing method such as mechanical removal is needed. Heat as a anti-icing method on the other hand works very well, as long as the surface temperature can hold the requirements of minimum $+3\text{ }^{\circ}\text{C}$.

The experiments also provided valuable experience and information needed to upgrade the test facility for more extreme conditions. The suggested modifications are; increase the freezing system capacity, test one pipe design at a time to reduce the freezing system requirements, increase fan capacity, install a permanent water spray system for icing experiments, and modify the test section geometry to test longer pipe lengths.

Experimental tests with more extreme conditions (Basic, Cold and Polar) are also suggested for future work and research.

Bibliography

- [1] 29. Fremgangsmåte og system for av-ising av skipskonstruksjoner. <https://search.patentstyret.no/Patentskrifter/Publisering/336839.pdf>, 2015. Online; accessed 10-May-2017.
- [2] C. Alexander. Rogue wave theory to save ships. <http://www.constantinealexander.net/2015/07/rogue-wave-theory-to-save-ships.html>, 7 2015. Online; accessed 13-Januar-2017.
- [3] T. L. Bergman, F. P. Incropera, D. P. DeWitt, and A. S. Lavine. *Fundamentals of heat and mass transfer*. John Wiley & Sons, 2011.
- [4] D. Bohne, S. Fischer, and E. Obermeier. Thermal, conductivity, density, viscosity, and prandtl-numbers of ethylene glycol-water mixtures. *Berichte der Bunsengesellschaft für physikalische Chemie*, 88(8):739–742, 1984.
- [5] A. Dehghani-sani, Y. S. Muzychka, and G. F. Naterer. Analysis of ice accretion on vertical surfaces of marine vessels and structures in arctic conditions. In *ASME 2015 34th International Conference on Ocean, Offshore and Arctic Engineering*, pages V007T06A056–V007T06A056. American Society of Mechanical Engineers, 2015.
- [6] DNV-GL. Rules for classification, ships. <https://rules.dnvgl.com/docs/pdf/dnvgl/ru-ship/2017-01/DNVGL-RU-SHIP-Pt6Ch6.pdf>, 1 2017. Online; accessed 13-Januar-2017.
- [7] H. Eicken. Salinity profiles of antarctic sea ice- field data and model results. *Journal of Geophysical Research*, 97(C10):15545–15557, 1992.
- [8] FLUKE. Smartview, mobil-app og programvare for analyse og rapportering av infrarøde bilder. <http://www.fluke.com/fluke/nono/tilbehorsok/programvare/fluke-smartview-ir-mobile.htm?pid=56169>. Online; accessed 22-July-2017.

-
- [9] S. Fukusako, A. Horibe, and M. Tago. Ice accretion characteristics along a circular cylinder immersed in a cold air stream with seawater spray. *Experimental Thermal and Fluid Science*, 2(1):81–90, 1989.
- [10] R. Gallant. Physical properties of hydrocarbons, v. 1: Gulf publ. Co., Houston, TX, 1968.
- [11] R. Gent, N. Dart, and J. Cansdale. Aircraft icing. *Philosophical Transactions of the Royal Society of London A: Mathematical, Physical and Engineering Sciences*, 358(1776):2873–2911, 2000.
- [12] E. S. Hansen. Numerical modelling of marine icing on offshore structures and vessels. Master’s thesis, NTNU Institutt for fysikk, 2012.
- [13] I. Horjen. *Numerical modelling of time-dependent marine icing, anti-icing and deicing*. PhD thesis, NTNU, 6 1990. Not available online, borrowed at the school library at NTNU.
- [14] H. Hu and S. A. Argyropoulos. Mathematical modelling of solidification and melting: a review. *Modelling and Simulation in Materials Science and Engineering*, 4(4):371, 1996.
- [15] IMO. International code for ships operating in polar waters (polar code). [http://www.imo.org/en/KnowledgeCentre/IndexofIMOResolutions/Maritime-Safety-Committee-\(MSC\)/Documents/MSC.385\(94\).pdf](http://www.imo.org/en/KnowledgeCentre/IndexofIMOResolutions/Maritime-Safety-Committee-(MSC)/Documents/MSC.385(94).pdf), 11 2014. Online; accessed 15-July-2017.
- [16] K. Instruments. Hotwire thermo-anemometer vt 110 – vt 115. http://www.instrumentcompaniet.no/files/NyeKimo/Kimo_VT110_VT115.pdf. Online; accessed 22-July-2017.
- [17] D. Jamieson and J. Tudhope. Physical properties of sea water solutions: thermal conductivity. *Desalination*, 8(3):393–401, 1970.
- [18] A. Kulyakhtin. *Numerical modelling and experiments on sea spray icing*. PhD thesis, NTNU and UNIS, 12 2014.
- [19] E. P. Lozowski, K. Szilder, and L. Makkonen. Computer simulation of marine ice accretion. *Philosophical Transactions of the Royal Society of London A: Mathematical, Physical and Engineering Sciences*, 358(1776):2811–2845, 2000.
- [20] MICRON. Table of emissivity of various surfaces. http://www-eng.lbl.gov/~dw/projects/DW4229_LHC_detector_analysis/calculations/emissivity2.pdf. Online; accessed 24-June-2017.
- [21] M. Paulin et al. Arctic offshore technology assessment of exploration and production options for cold regions of the us outer continental shelf. *prepared by IMV for American Bureau of Ocean Energy Management, Regulation and Enforcement, IMVPA Project No C-0506-15*, 2008.

-
- [22] P. Roebber and P. Mitten. Modelling and measurement of icing in canadian waters. canadian climate centre, report 87-15, 150 pp, 1987.
- [23] C. C. Ryerson. Ice protection of offshore platforms. *Cold Regions Science and Technology*, 65(1):97–110, 2011.
- [24] E. M. Samuelsen, S. Løset, and K. Edvardsen. Marine icing observed on kv nordkapp during a cold air outbreak with a developing polar low in the barents sea. *Port and Ocean Engineering under Arctic Conditions*, 2015.
- [25] T. Sawada. Ice accretion on ships in northern seas of japan. *Journal of the Meteorological Society of Japan. Ser. II*, 46(3):250–254, 1968.
- [26] F. Schwerdtfeger. The thermal properties of sea ice. *Journal of glaciology*, 36:789–807, 1963.
- [27] Ulmatec. Ulmatec. <http://www.ulmatec.no/>. Online; accessed 16-Januar-2017.
- [28] H. M. Valderhaug. Photo:. http://sysla.no/2015/07/08/maritim/jobber-pa-spreng-for-a-finne-arbeid-til-dette-nye-skipet_54442/, 7 2015. Online; accessed 13-Januar-2017.
- [29] A. J. yunus A. Cengel. *Heat and Mass Transfer*. Mc Graw Hill, 2 Penn Plaza, New York, 5 edition, 2015.

Material Properties

A.1 Saline Ice and Water

A comparison of thermal properties of pure water and saline water was conducted in the pre-project to consider the possibility of using already existing material properties within COMSOL in the simulation of the de-icing process.

Table A.1: Thermal Properties of Sea Ice $0^{\circ}C - 8^{\circ}C$ [26]

Thermal Properties of Sea Ice $0^{\circ}C - 8^{\circ}C$			
Salinity (S) [‰]	Temperature (T) [°C]	Conductivity (k) [W/(mK)]	Density (ρ) [g/cm ³]
8	-1	1.385	0.925
	-2	1.724	0.925
	-4	1.904	0.925
	-8	1.996	0.925

A part of the study of thermal properties of sea ice done by Schwerdtfeger, F. is represented in Table A.1. The article concluded that: *Already at $-8^{\circ}C$ all the curves show asymptotic behavior. At lower temperatures, the conductivity of low salinity ice will tend to the value for freshwater ice [26].* Natural sea water has a salinity of approximately [30 – 35‰] [17]. Hence, the salinity of the melted water during the de-icing process will have a lower salinity than natural sea water, values between (0-8‰) [26]. The variation conductivity of saline water compared to fresh water is negligible [17]. Hence, the values of freshwater is plotted. The measured values represented in table A.1 is plotted together with measured conductivity values of fresh water in figure A.1, (plotted as dots). The curve fitting tool in MATLAB were used to make functions of temperature which could be implemented in COMSOL as material data for saline ice and water. **The input temperatures for these functions must be in Celsius [°C].**

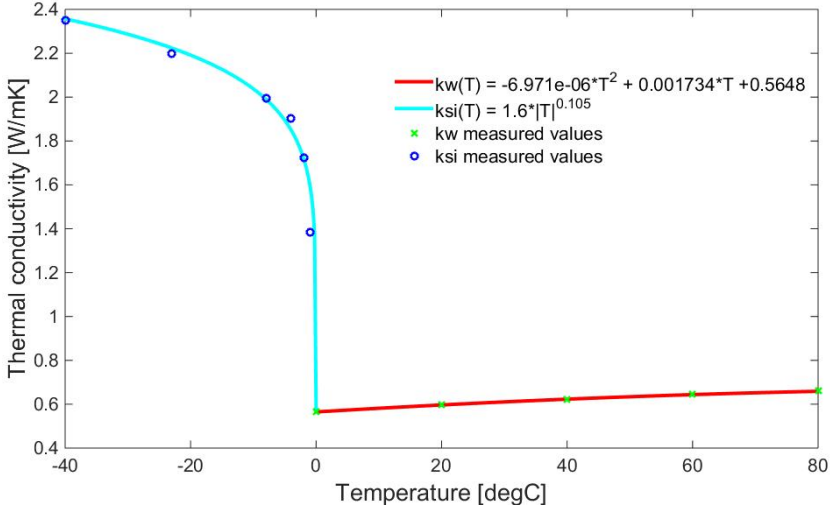


Figure A.1: Thermal Conductivity (k) of saline water and ice. The lines show functions of temperature from regression, while the dots represents measured values.

A.2 Glycol-Water mixture

The thermal properties listed in table A.2 are taken from the article '*Thermal, Conductivity, Density, Viscosity, and Prandtl-Numbers of Ethylene Glycol-Water Mixtures*' [4], where the authors used the specific heat capacity values from the book '*Physical properties of hydrocarbons*' [10].

To simplify the calculations, polynomials were deducted from table A.2 using a regression analysis. The De-Icing analysis use temperature between -45°C and 80°C , hence property polynomials were made for the temperature range $[-50^{\circ}\text{C}, 100^{\circ}\text{C}]$. A summary of the functions are listed below;

$$k(T) = (-6.504 * 10^{-9})T^3 + (4.52 * 10^{-6})T^2 - (3.454 * 10^{-4})T + 0.2424 \quad (\text{A.1})$$

$$c_p(T) = (-0.01946)T^2 + (16.66)T + 109.5 \quad (\text{A.2})$$

$$\rho(T) = (-1.627 * 10^{-3})T^2 + (0.374)T + 1097 \quad (\text{A.3})$$

$$\mu(T) = (6.914 * 10^4)e^{(-0.05999T)} + 0.09799e^{(-0.01318T)} \quad (\text{A.4})$$

The input temperatures (T) for these polynomials must be in Kelvin [K].

These functions are used in the simulation models in MATLAB.

Table A.2: The thermal properties conductivity, density and dynamic viscosity are taken from[4], while the specific heat capacity are taken form [10].

Solution by volume [%]	Temperature [$^{\circ}C$]	Thermal conductivity [W/mK]
55	-19.27	0.3396
	26.26	0.3698
	65.78	0.3913
	109.88	0.4077
Solution by volume [%]	Temperature [$^{\circ}C$]	Density [kg/m^3]
51	-8.40	1081.97
	0.70	1077.16
	10.10	1072.06
	19.50	1066.66
	25.00	1063.80
	29.30	1061.13
	39.60	1053.85
	60.80	1041.44
	80.20	1025.27
Solution by volume [%]	Temperature [$^{\circ}C$]	Dynamic Viscosity [$mPa * s$]
49.9	-9.20	12.22
	-0.40	8.057
	9.40	5.366
	19.30	3.780
	29.60	2.732
	39.60	2.069
	60.50	1.309
	80.30	0.920
	100.60	0.799
Solution by volume [%]	Temperature [$^{\circ}C$]	Specific heat [J/kgK]
50	-10	3140
	0	3224
	20	3308
	40	3412
	60	3517
	80	3559

A.3 Air

Material properties are found from table A-15 in Heat and Mass Transfer, Fundamentals and applications [29]. To simplify the calculations, polynomials were deduced from the material properties tables using a regression analysis. The De-Icing analysis use temperature between -40°C and 80°C , hence property polynomials were made for the temperature range $[-50^{\circ}\text{C}, 100^{\circ}\text{C}]$. A summary of the functions are listed below;

$$k(T) = -(3 * 10^{-8})T^2 + (8 * 10^{-5})T + 0.0236 \quad (\text{A.5})$$

$$c_p(T) = -(7 * 10^{-8})T^4 + (2 * 10^{-5})T^3 - (1.2 * 10^{-3})T^2 - 0.034T + 1.0064 \quad (\text{A.6})$$

$$\rho(T) = (5 * 10^{-10})T^4 - (8 * 10^{-8})T^3 + (2 * 10^{-5})T^2 - 0.0047T + 1.2933 \quad (\text{A.7})$$

$$\mu(T) = (10^{-10})T^2 + (9 * 10^{-8})T + 10^{-5} \quad (\text{A.8})$$

$$Pr(T) = (10^{-8})T^3 - (10^{-6})T^2 - 0.0002T + 0.7362 \quad (\text{A.9})$$

The input temperatures (T) for these polynomials must be in Celsius [$^{\circ}\text{C}$].

These functions are used in the simulation models in MATLAB.

Appendix **B**

MATLAB Codes

1D model for steady state analysis (Main Code).

Functions called by the Main Code:

1. Heat transfer coefficient for the inner flow (hw1).
2. Heat transfer coefficient for the annulus flow (hw2).
3. Heat transfer coefficient for the outer air flow (hair).
4. Thermal capacitance due to mass flow (QL).
5. Heat transfer coefficient for the inner pipe wall, due to thermal resistance (QR1).
6. Heat transfer coefficient for the outer pipe wall, due to thermal resistance (QR22).

```

1 % This Code simulates the temperatures for Ulmatec Pyro Double-Pipe design
2 % Coded by Lene Esøy 30.03.2017
3
4 % The pipe is modeled using finite difference method (FDM)
5 % For heat transfer Lumped Capacitance Method (LCM) is used
6
7 clear all
8 clc
9 clf
10
11 %% INPUT Parameters=====
12
13 m=400;           %[-] number of elements along L
14 Tin=20+273.15;  %[K] Tin water inlet temperature
15 Tlim=3+273.15;  %[K] Tlim is the surface temperature limmit
16                %from DNV GL (+3degC or 276.15K)
17 Tinf=-10+273.15; %[K] air temperature
18 Vflow=0.01/3600; %[m^3/s] volumetric flow
19 U=0;           %[m/s] wind velocity
20 dr=0.6565;     %[-] radius factor %0.8388 50x38, %0.6565 50x32
21 r2=0.025;      %[m] radius outer pipe %0.025 for {\O}50mm
22 L=2.5;         %[m] length of the pipe
23
24 %% CALCULATION STARTS =====
25
26 % Initializing Parameters-----
27
28 %Parameters dependent on INPUT
29 dL=L/m;         %[m] Length of each element
30 r1=dr*r2;      %[m] radius inner pipe
31
32 %Making zero vectors (Ax-B=0) => (Q*T = Qtot)
33 n=2;           %This is a fixed parameter
34 Q=zeros(m*n,m*n); %A-matrix
35 Qtot=zeros(m*n,1); %B-matrix
36
37 %Since Q matrix is dependent on the T vector, an iteration process has to
38 %be done, here T0 is the startig condition.
39 for e=1:(n*m)
40 T0(e,1)=Tin;   %Starting iteration with Tin for all elements.
41 end
42
43 % Iteration starts-----
44
45 for cal=1:40   %iteration loop, updating the matrixes for each new T0
46
47 % Making the matrixes A and B calling the functions QL, QR1 and QR22:
48 %QL=QL(Vflow,T1) Thermal Capacitance coeff. [W/K], mass transport
49 %QR1=QR1(r1,r2,T1,T2,dL) Heat transfer coeff. [W/K],inner pipe wall
50 %QR22(r1,r2,T2,Tinf,dL,U) Heat transfer coeff. [W/K], outer pipe wall
51
52 % Making the boundary heat flow matrix B
53 for in=1:m
54 Qtot(1,1)=-QL(Vflow,Tin)*Tin; %[W] Heat transfer from the inlet flow
55 Qtot(in*n,1)=-QR22(r1,r2,T0(in*n,1),Tinf,dL,U,Vflow)*(Tinf);
56 %[W] Heat transfer to the air due to convection
57 end
58
59 % Making the thermal coefficient matrix A
60

```

```

61 % For m=1 Inlet side nodes
62 for i=1
63     for j=1 %inner pipe flow
64         Q(j,j)=-QL(Vflow,T0(j,1))-QR1(r1,r2,T0(j,1),T0(j+1,1),dL,Vflow);
65         Q(j+1,j)=QR1(r1,r2,T0(j,1),T0(j+1,1),dL,Vflow);
66     end
67     for j=2 %outer pipe flow
68         Q(j-1,j)=QR1(r1,r2,T0(j-1,1),T0(j,1),dL,Vflow);
69         Q(j,j)=-QL(Vflow,T0(j,1))-QR1(r1,r2,T0(j-1,1),T0(j,1),dL,Vflow)...
70             -QR22(r1,r2,T0(j,1),Tinf,dL,U,Vflow);
71         Q(j,j+n)=QL(Vflow,T0(j+n,1));
72     end
73 end
74
75 % For m= 2:m-1 Mid nodes
76 for i=2:1:m-1
77     for j=1+(n*(i-1)) %inner pipe flow
78         Q(j,j-n)=QL(Vflow,T0(j-n,1));
79         Q(j,j)=-QL(Vflow,T0(j,1))-QR1(r1,r2,T0(j,1),T0(j+1,1),dL,Vflow);
80         Q(j+1,j)=QR1(r1,r2,T0(j,1),T0(j+1,1),dL,Vflow);
81     end
82     for j=2+(n*(i-1)) %outer pipe flow
83         Q(j-1,j)=QR1(r1,r2,T0(j-1,1),T0(j,1),dL,Vflow);
84         Q(j,j)=-QL(Vflow,T0(j,1))-QR22(r1,r2,T0(j,1),Tinf,dL,U,Vflow)...
85             -QR1(r1,r2,T0(j-1,1),T0(j,1),dL,Vflow);
86         Q(j,j+n)=QL(Vflow,T0(j+n,1));
87     end
88 end
89
90 % For m=m The nodes where the water turns
91 for i=m
92     for j=1+(n*(i-1)) %inner pipe flow
93         Q(j,j-n)=QL(Vflow,T0(j-n,1)) ;
94         Q(j,j)=-QL(Vflow,T0(j,1))-QR1(r1,r2,T0(j,1),T0(j+1,1),dL,Vflow) ;
95         Q(j+1,j)=QL(Vflow,T0(j,1))+QR1(r1,r2,T0(j,1),T0(j+1,1),dL,Vflow) ;
96     end
97     for j=2+(n*(i-1)) %outer pipe flow
98         Q(j-1,j)=QR1(r1,r2,T0(j-1,1),T0(j,1),dL,Vflow) ;
99         Q(j,j)=-QL(Vflow,T0(j,1))-QR1(r1,r2,T0(j-1,1),T0(j,1),dL,Vflow)...
100             -QR22(r1,r2,T0(j,1),Tinf,dL,U,Vflow) ;
101     end
102 end
103
104 T = Q\Qtot;           % calculating the resulting temperature vector T
105 T0=T;                %updating the new T0 vector for the next iteration
106
107 end
108
109
110 %% Preparing results for plotting=====
111
112 % Separating the result vector T into Ti(inner pipe) and To(outer pipe)
113 Ti(1)=Tin;
114 s=1;
115 for p=1:n:m*n
116     Ti(s+1)=T(p,1);
117     To(s+1)=T(p+1,1);
118     s=s+1;
119 end
120

```

```

121 %Estimating the outlet temperature from the last two temperature points
122 To(1)=To(2)+(To(2)-To(3));
123
124 % Calculaing Ts(surface temperature) from To(temperature outer pipe)
125 for i=1:m+1
126     Ts(i)=(hw2(To(i),r1,r2,Vflow)*To(i))+(hair(Tinf,To(i),U,r2)*Tinf)...
127         /((hair(Tinf,To(i),U,r2)+hw2(To(i),r1,r2,Vflow)));
128 end
129
130 % Making L vector for plotting
131 for l=1:m
132     L(l)=0;
133     L(l+1)=dL*1;
134 end
135
136 %change the unit from Kelvin to degree Celsius for plotting
137 Ts=Ts-273.15;
138 To=To-273.15;
139 Ti=Ti-273.15;
140 Tlim=Tlim-273.15;
141
142 % DNV GL Rules for minimum surface temperature
143 Limmit=ones(1,length(L))*Tlim;
144
145 %% Plotting=====
146
147 plot1=plot(L,Ts,'r',L,To,'g',L,Ti,'b')%,L,Limmit,'c')
148 set(plot1,'LineWidth',2.5)
149 set(gca,'FontSize',16)
150 leg=legend({'Temperature at the surface $$T_s$$'...
151     , 'Temperature outer pipe flow $$T_o$$'...
152     , 'Temperature inner pipe flow $$T_i$$'}...
153     , 'box','off');%, 'Surface temperature limmit by DNV GL')
154 set(leg,'Interpreter','latex','FontSize',16);
155 xlabel('Length of pipe L [m]','Interpreter','latex','FontSize',24)
156 ylabel('Temperature $$[^\circ C]$$','Interpreter','latex','FontSize',24)
157 xlswrite('TiToTsC2.xlsx',[L' Ti' To' Ts]) %Temperature into Excel format

```

```

1 function heat1 = hwl(T,r1,V)
2 % This function calculates the total heat transfere coeffisient for
3   %inner pipe flow due to forced convection
4
5 % Coded by Lene Esøy 30.03.2017
6
7 %% Thermal properties of Glycol/Water (50/50)
8 dynvisk_gw=dvw(T);% [kg/ms]
9 rho_gw=rhow(T); %[kg/m^3]
10 Pr_gw=prw(T); % [-]
11 k=0.5; %[W/Km]
12
13 %% Flow velocities and Reynolds number
14 Vflow=V/3600;           % [m^3/s] volumetric flow rate
15 u1=(Vflow)/(pi*r1^2)   % [m/s] Average flow velocity
16 Re1=rho_gw*u1*r1/dynvisk_gw; % Reynoldsnumber for the inner flow
17
18 %turbulent flow 3000<Re<5000000
19 if Re1>=3000
20 f1=((0.79*log(Re1))-(1.64))^(2); %darcys friction factor for smooth pipe
21 Nul=((f1/8)*(Re1-1000)*Pr_gw)/(1+((12.7)*((f1/8)^0.5)*((Pr_gw^(2/3))-1)));
22                                     % Nusselts number
23 heat1=(Nul*k)/(2*r1);           % [W/Km^2] heat transfer coefficient
24
25 %transition flow 2300<Re<3000
26 elseif Re1>2300
27 f1=((3.03*10^-12)*Re1^3)-((3.67*10^-8)*Re1^2)+((1.46*10^-4)*Re1)-0.151 ;
28                                     %darcys friction factor for smooth round pipe
29 Nul=((f1/8)*(Re1-1000)*Pr_gw)/(1+((12.7)*((f1/8)^0.5)*((Pr_gw^(2/3))-1)));
30                                     % Nusselts number
31 heat1=(Nul*k)/(2*r1);           % [W/Km^2] heat transfer coefficient
32
33 %laminar flow Re<2300
34 else Re1<=2300
35 Nul=4.36;                         % constant heat flux
36 heat1=(Nul*k)/(2*r1);           % [W/Km^2] heat transfer coefficient
37 end
38 end
39

```

```

1 function heat2 = hw2(T,r1,r2,V)
2 % This function calculates the total heat transfere coefficient for
3   %Annulus (outer pipe) flow due to forced convection
4
5 % Coded by Lene Esøy 30.03.2017
6
7 %% Thermal properties of Glycol/Water (50/50)
8 dynvisk_gw=dvw(T);           % [kg/ms]
9 rho_gw=rhow(T);             %[kg/m^3]
10 Pr_gw=prw(T);               % [-]
11 k=0.5;                       % [W/Km]
12
13 %% Flow velocities and Reynolds number
14 Dh=(r2-r1)*2;                % [m] Hydraulic diameter for pipe annulus
15 Vflow=V/3600;                % [m^3/s] volumetric flow rate
16 u2=(Vflow)/(pi*((r2^2)-(r1^2))); % [m/s] average flow velocity
17 Re2=rho_gw*u2*Dh/dynvisk_gw; % Reynolds number
18
19 %turbulent flow 3000<Re<5000000
20 if Re2>=3000
21 f2=((0.79*log(Re2))-(1.64))^( -2); % Darcys friction factor
22 Nu2=((f2/8)*(Re2-1000)*Pr_gw)/(1+((12.7)...
23   *((f2/8)^0.5)*((Pr_gw^(2/3))-1))); % Nusselts number
24 heat2=(Nu2*k)/(Dh);          % [W/Km^2] heat transfer coeff.
25
26 %transition flow 2300<Re<3000
27 elseif Re2>2300
28 f2=((3.03*10^-12)*Re2^3)-((3.67*10^-8)*Re2^2)+...
29   ((1.46*10^-4)*Re2)-0.151; % Darcys friction factor for smooth pipe
30 Nu2=((f2/8)*(Re2-1000)*Pr_gw)/(1+((12.7)...
31   *((f2/8)^0.5)*((Pr_gw^(2/3))-1)));
32 % Nusselts number
33 heat2=(Nu2*k)/(2*r1);        % [W/Km^2] heat transfer coefficient
34
35 %laminar flow Re<2300
36 elseif Re2<=2300
37 Nu2=4.36 ;                   % Nusselts number
38 heat2=(Nu2*k)/(Dh);          % [W/Km^2] heat transfer coefficient
39 end
40 end

```



```

1 function heat3 = hair(Tinf,Ts,U,r2)
2 % This function calculates the total heat transfere coefficient for
3   %air flow due to natural and forced convection
4
5 % Coded by Lene Esøy 30.03.2017
6
7 Tinf=Tinf-273.15;           %Temperature far away from pipe [deg]
8 Tsurf=Ts-273.15;         %Surfacetemperature [deg]
9 Uwind=U;                 %Wind velocity [m/s]
10 m=length(Tsurf);
11 Dpipe=2*r2;              %Outside diameter of pipe [m]
12 N=length(Uwind);
13
14 for i=1:m
15 for j=1:N
16
17 % Thermal properties of air using boundary layer temperature
18   Tavg(i)=0.5.*(Tsurf(i)+Tinf(1));   %Average boundary layer temp
19   Kair(i)=(-3*(10^-8).*(Tavg(i)^2)+(Tavg(i).*(8*(10^-5)))...
20     +0.0236;
21   Prair(i)=((10^-8).*(Tavg(i)^3))-((10^-6).*(Tavg(i)^2))...
22     -(0.0002.*Tavg(i))+0.7362;
23   myair(i)=((10^-10).*(Tavg(i)^2)+(9*(10^-8).*Tavg(i))...
24     +(10^-5);
25   beta=1/(273.15+Tavg(i));
26   g=9.81;
27
28   Re(j)=Uwind(j)*Dpipe/myair(i);     %Reynolds number
29
30 % Heat flux coefficient forced convection
31   if Re(j)*Prair(i)>=0.2
32     Nuf(j,i)=0.3+(((0.62*(Re(j)^0.5)*(Prair(i)^(1/3)))/((1+((0.4/...
33       Prair(i)^(2/3)))^(1/4))))*(1+((Re(j)/282000)^(5/8)))^(4/5));
34     hconvf(j,i)=(Kair(i)/Dpipe)*Nuf(j,i);
35   else
36     Nuf(j,i)=0;
37     hconvf(j,i)=(Kair(i)/Dpipe)*Nuf(j,i);
38   end
39
40 % Heat flux coefficient natural convection
41   RaD(i)=(g*beta*(Tsurf(i)-Tinf(1))*(Dpipe^3))/(myair(i)^2);
42   Nun(i)=(0.6+(((0.387.*(RaD(i).^(1/6)))/((1+((0.559/Prair(i))...
43     .^(9/16))).^(8/27))))).^2;
44   hconvn(i)=(Kair(i)/Dpipe)*Nun(i);
45
46   Nutot(j,i)=((Nuf(j,i)^4)+(Nun(i)^4))^(1/4);
47
48   heat3(i,j)=(Kair(i)/Dpipe)*Nutot(j,i);
49   heat3=heat3(i,j) ;
50   j=j+1;
51 end
52   i=i+1 ;
53 end
54 end

```

```

function ThermalCapacitance = QL(Vflow,T)
% This function calculates the Thermal Capacitance [W/K]
%due to mass transport

% Coded by Lene Esøy 30.03.2017

ThermalCapacitance=Vflow*rhow(T)*cpw(T);
end

function HeatTransferCoefficient = QR1(r1,r2,T1,T2,dL,V)
% This function calculates the overall heat transfer coefficient [W/K]
%through the inner pipe wall

% Coded by Lene Esøy 30.03.2017

A=2*pi*dL*r1;
Uwall=1/((1/(hw1(T1,r1,V)))+(1/(hw2(T2,r1,r2,V))));
HeatTransferCoefficient=Uwall*A;
% Due to thin wall and high conductivity of the pipe wall, this is
%neglected in the overall heat transfer coefficient Uwall.
end

function HeatTransferCoefficient2 = QR22(r1,r2,T2,Tinf,dL,U,V)
% This function calculates the overall heat transfer coefficient [W/K]
%through the outer pipe wall

% Coded by Lene Esøy 30.03.2017

Ts=T2; % For calculation of the air properties of the boundary layer,
% assuming surface temperature equal to the annulus flow temp
A=2*pi*dL*r2;
Uwall=1/((1/(1*(hair(Tinf,Ts,U,r2)))+(1/(hw2(T2,r1,r2,V))));
HeatTransferCoefficient2=Uwall*A;
% Due to thin wall and high conductivity of the pipe wall, this is
%neglected in the overall heat transfer coefficient Uwall.
end

```